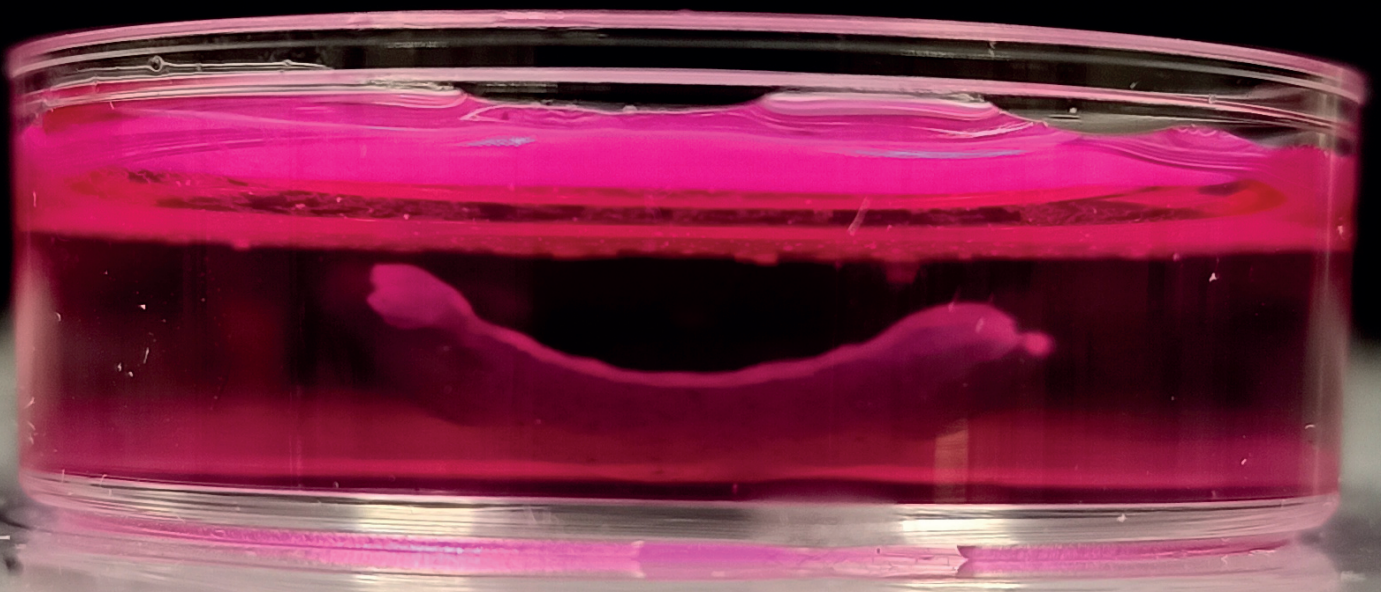


4D bioprinting for cartilage tissue engineering: a controlled shape transformation approach

Maria Kalogeropoulou



4D bioprinting for cartilage tissue engineering: a controlled shape transformation approach

by

Maria Kalogeropoulou

to obtain the degree of Master of Science in

Biomedical Engineering

at the Delft University of Technology,
to be defended publicly on the 30th of July 2021.

Student number: 5140234
Project duration: February 1, 2021 – July 1, 2021
Supervisory Team: Prof. dr. A. A. Zadpoor, TU Delft
Assistant. Prof. dr. L. Fratilla-Apachitei, TU Delft
dr. P. J. Díaz-Payno, TU Delft

An electronic version of this thesis is available at <http://repository.tudelft.nl/>.

Contents

Preface	1
Acknowledgements	2
Abstract	3
Abbreviations and Nomenclature	4
1 Introduction	6
2 Experimental Section	9
2.1 Reagents and Materials	9
2.2 Preparation of HA-Tyr and Alg/HA-Tyr Inks	9
2.3 Rheological Characterization	10
2.4 Shear Thinning Modeling	12
2.5 Multi-material 4D printing	12
2.6 Compression Tests	14
2.7 Swelling Studies of Single Material Scaffolds	15
2.8 Curvature Analysis	15
2.9 Self-bending Model	16
2.10 Cell Studies	17
2.10.1 Cell Thawing And Plating	17
2.10.2 Trypsinization	18
2.10.3 Pellet Preparation and Culture	18
2.10.4 Media Preparation	18
2.10.5 CaCl ₂ Effect on hMSCs	19
2.11 4D Bioprinting	19
2.12 Cell Assays	21
2.12.1 Presto Blue™ Assay	21

2.12.2	Live/Dead Assay	21
2.13	Histological Analysis	22
2.13.1	Fixation	22
2.13.2	Agarose Embedding	22
2.13.3	Dehydration	23
2.13.4	Paraffin Embedding	23
2.13.5	Slicing	23
2.13.6	Staining	23
2.13.7	Imaging	24
2.14	Statistical Analysis	24
3	Results	25
3.1	Rheological Characterization of the HA-Tyr and Alg/HA-Tyr inks	25
3.2	Single-Material 3D Printing: Printing Optimization, Scaffold Design and Characterization	28
3.3	Multimaterial 3D Printing: From 3D to 4D	28
3.4	Parameters affecting self-bending	30
3.4.1	Effect of Infill Density and Printing Pattern on Curvature	30
3.4.2	Effect of Thickness Ratio on Curvature	32
3.4.3	Effect of CaCl ₂ Crosslinking Time on Curvature	34
3.4.4	Effect of Solution Composition on Curvature	36
3.5	4D Bioprinting	38
3.5.1	Determination of the Chondrogenic Capacity of hMSCs and Medium Optimization	38
3.5.2	4D Bioprinting using Cell Expansion Medium	41
3.5.3	4D Bioprinting using Chondrogenic Medium	43
4	Discussion	46
5	Concluding Remarks and Future Perspectives	50

References	52
Appendices	58
APPENDIX A: Effect of CaCl₂ concentration and exposure time on hMSCs	58
APPENDIX B: Cell Viability Assays: Protocol Optimization	59
APPENDIX C: Images of 4D Bioprinted Scaffolds.	61
APPENDIX D: Scaffold Stability	62
APPENDIX E: Use of DMEM in ink preparation	63
Appendix F: Molding and Staining Protocols	64

Preface

This project was carried out at the Biomechanical Engineering Department, 3mE, TU Delft. All experiments involving (bio)printing, scaffold evaluation and imaging were performed at the Cytocompatibility and Biointerfaces (CCB) Lab while histological analyses were conducted at the Chemistry Lab (3mE, TU Delft). Rheological measurements were performed at the Bionanoscience Department (TNW, TU Delft).

Delft, July 2021

Acknowledgements

The completion of this thesis would not have been possible without the help and support of Assistant Professor Dr. Lidy Fratila-Apachitei. She trusted me with a very ambitious project and gave me invaluable guidance and encouragement, throughout the course of my thesis.

I would like to express my deepest appreciation to Professor Dr. Amir Zadpoor for his valuable suggestions and comments on my project. He encouraged me to thoroughly investigate the behavior of the printed scaffolds in various conditions, thus, inspiring me to try and understand the self-bending mechanism of my project in depth.

Moreover, I would like to thank my daily supervisor, Dr. Pedro J. Diaz-Payno for training and helping me in every stage of this project, from grasping the initial concept to preparing for the final defense. With his precious guidance I was able to successfully plan and carry out all my experiments.

In addition, I would like to thank Prof. Dr. Gijsje Koenderink for giving me access in the rheology labs of the Bionanoscience Department (TNW faculty, TU Delft) where I could perform measurements for characterizing the printability of the materials I used.

I owe a special thanks to Esther Kingma, who started as being my lab partner and became a very dear friend. She made long lab days pass in a pleasant way and supported me in situations beyond the thesis per se.

A very big “thank you”, from the bottom of my heart, goes to my parents, Nick and Vicky, my little sister, Gina and my “extra” pair of parents, Kostas and Victoria. They were always by my side, calling or texting me, and experienced all the ups and downs of this project with me.

I also want to thank my best friend, Helen, for her lovely surprises and our daily chats that always made me smile. Her academic guidance and advice helped me see things from a different perspective and I am deeply grateful for that.

Last, but definitely not least, I would like to express my heartfelt gratitude to my boyfriend, Jacob. His love and support gave me the strength to finish this project and his kind smile cheered me up whenever I had a bad day.

Abstract

Cartilage degeneration is a major cause of chronic disability and its treatment usually involves highly invasive procedures. To address this issue, three-dimensional (3D) bioprinting was introduced as a promising tissue engineering approach. However, the structures fabricated with this method are static and lack the dynamic response of native tissues. Moreover, the fabrication of curved or tubular structures remained challenging, especially in the case of soft tissues. Four-dimensional (4D) bioprinting is a newly emerged, next-generation biofabrication technology capable of resolving the aforementioned challenges. In this thesis, an advanced 4D bioprinting method based on multi-material extrusion of two hydrogel-based (bio)inks is reported. This approach allows the fabrication of bilayered scaffolds made from a bottom part of a HA-Tyr precursor and a composite hydrogel top part from alginate and HA-Tyr (Alg/HA-Tyr). The scaffolds demonstrated self-bending upon immersion in aqueous solutions that was driven by the different swelling capacity of the two inks. Compatibility of the inks with extrusion printing was verified by rheological characterization. Control of the obtained curvature was achieved by tuning the infill density, printing angle and layer thickness. Moreover, the effect of crosslinking time as well as the influence of the swelling solvent type in the degree of bending was also investigated. Finally, human mesenchymal stem cells (hMSCs) were mixed with the Alg/HA-Tyr ink and self-bending living scaffolds were bioprinted. The shape-shifted scaffolds were capable of supporting a high cell viability for up to 14 days and remained viable for up to 4 weeks.

Abbreviations and Nomenclature

3D	Three-Dimensional
CAD	Computer-Aided Design
CT	Computerized Tomography
MRI	Magnetic Resonance Imaging
HA	Hyaluronic Acid
ECM	Extracellular Matrix
GAG	Glycosaminoglycan
HA-Tyr	Tyramine-modified Hyaluronic Acid
HRP	Horseradish Peroxidase
H ₂ O ₂	Hydrogen Peroxide
EO	Eosin Y
4D	Four-Dimensional
Alg/HA-Tyr	Sodium Alginate/Tyramine-modified Hyaluronic Acid
CaCl ₂	Calcium Chloride
hMSCs	Human Mesenchymal Stem Cells
NaCl	Sodium Chloride
FBS	Fetal Bovine Serum
AA	Ascorbic Acid
ITS+	Insulin Transferring Selenic Acid
TGF- β 1	Transforming Growth Factor- β 1
HCl	Hydrochloric Acid
DMEM	Dulbecco's Modied Eagle Medium
α MEM	α Minimum Essential Medium
EthD-1	Ethidium Homodimer
TNS	Trypsin Neutralizing Solution
FGF2	Human Fibroblast Growth Factor
STL	Stereolithography
CO ₂	Carbon Dioxide
CM-L	Chondrogenic Differentiation Medium (Lonza)
CM-E	Chondrogenic Differentiation Medium (Erasmus MC)
PBS	Phosphate-Buffered Saline
UV	Ultraviolet
RFU	Relative Fluorescent Unit
PFA	Paraformaldehyde
NA	Numerical Apperture
ANOVA	Analysis Of Variance
RT	Room Temperature

Ca^{2+}	Calcium Cation
g	Gravitational Acceleration
G'	Storage Modulus
G''	Loss Modulus
s	Second(s)
min	Minute(s)
h	Hour(s)
Hz	Hertz
rad	Radians
η	Viscosity
K	Ostwald-de Waele model constant
$\dot{\gamma}$	Shear Rate
n	Ostwald-de Waele model constant
E	Elastic Modulus
E_0	Elastic Modulus at Dry State
R^2	Coefficient of determination
SR_m	Mass Swelling Ratio
SR_v	Volumetric Swelling Ratio
κ	Curvature
ρ	Radius of Curvature
$\tan\delta$	Damping Factor
γ	Shear Strain
k	Thermal Expansion Coefficient
t	Final Temperature
t_0	Initial Temperature
m	Ratio of Layer Thicknesses
h	Total Scaffold Thickness
n	Ratio of Elastic Moduli
λ	Linear Expansion Rate

1 Introduction

Articular cartilage is avascular, non-innervated and relies on diffusion for nutrient and waste exchange, resulting in its low healing potential. Consequently, cartilage is prone to degenerative conditions, such as osteoarthritis, which poses a substantial clinical problem and is a major cause of chronic disability [1]. Numerous approaches have been proposed and/or implemented for advanced cartilage degeneration treatment, with the most common being joint replacement surgery, a highly invasive and expensive procedure [2]. Hence, less invasive cartilage repair strategies that could decrease hospitalization time and enhance the postoperative life quality of patients seem particularly attractive. Cartilage engineering aims at the fabrication of tissue that closely recapitulates the structure and function of native cartilage and has emerged as a promising alternative treatment method, attracting increasing interest [3,4]. More precisely, 3D bioprinting of living scaffolds, capable of producing mature cartilage tissue has emerged as a novel fabrication method and has already yielded promising results [3,5,6].

Three dimensional (3D) bioprinting is a powerful and versatile technology for the fabrication of biomimetic tissue constructs, enabling an unprecedented control over the composition and geometry of the printed structures. This technology supports the fabrication of highly sophisticated scaffolds, capable of closely recapitulating the heterogeneity and complexity of native tissues [7–9]. In 3D bioprinting, cell-laden hydrogels, collectively known as “bioinks”, are used for the fabrication of living scaffolds in a layer-by-layer manner [10]. Briefly, the scaffold is modeled using advanced computer aided design (CAD) or obtained from an existent structure (*e.g.*, from a CT or MRI of a patient) and sliced in layers by specialized software. The resulting document is, subsequently, used as input for a bioprinting device, which will fabricate the scaffold based on the provided “blueprint”. Currently, there are three biofabrication approaches, namely extrusion-, inkjet- and laser-based bioprinting. Among them, particular focus has been placed on extrusion(-based) bioprinting [11,12]. In extrusion bioprinting, the bioink is pushed through a nozzle or a needle, driven by a mechanical or pneumatic system, and is deposited on the printing platform as a continuous, cylindrical filament. The filament is extruded, using a predetermined printing pattern, pressure and speed, in successive two-dimensional layers, until the 3D scaffold is fabricated.

Bioinks compatible with extrusion bioprinting are usually natural polymer hydrogel precursors, such as hyaluronan [13], gelatin [14], alginate [15] and collagen [16], because they exhibit structural similarities to the native extracellular matrix (ECM) and allow homogeneous cell mixing in a highly hydrated environment. Precursors are usually subjected to a pre-crosslinking step in order to improve printability and filament formation. Pre-crosslinking strategies include enzymatic [17] or ionic mediated crosslinking [18]. After printing, a secondary crosslinking is usually applied (*e.g.*, photocrosslinking [19,20]) to enhance the mechanical strength of the extruded filaments.

Hyaluronan (also known as hyaluronic acid and hereinafter abbreviated as HA) is a non-sulfated glycosaminoglycan (GAG) and an ubiquitous component of native ECM, and can be found in abundance in mammalian connective tissues [21]. More specifically, in articular cartilage, HA is a strategic player in maintaining cartilage homeostasis by regulating cellular functions, including the promotion of the chondrogenic phenotype and the production of ECM components [22]. Chondrocytes possess processes extending in the matrix, however, they are cytoplasmically isolated from their neighbouring cells [23]. Therefore, cell-matrix

interactions are vital for the maintenance of cartilage ECM. Hence, HA-based hydrogels have been investigated as suitable bioinks for cartilage tissue engineering [24–26]. Different crosslinking methods, such as enzymatic- or photo-crosslinking, have been implemented to fabricate printable HA-based bioinks [13]. Recently, the use of tyramine-modified HA (HA-Tyr) as a bioink was proposed as a promising biomaterial due to its straightforward preparation and its dual crosslinking potential using two independent mechanisms to tune its printability [20]. The first crosslinking mechanism of HA-Tyr is enzymatically mediated and is catalyzed by horseradish peroxidase (HRP) in the presence of hydrogen peroxide (H_2O_2) [27]. By tuning the concentrations of HRP and H_2O_2 , hydrogel precursors of different viscosities can be prepared, allowing for a great control over the customization of extrusion parameters. Additionally, incorporation of a photoinitiator in the hydrogel, such as Eosin Y (EO) or rose Bengal [27], permits a secondary photocrosslinking triggered by visible light irradiation.

On the other hand, alginate is a natural, non-toxic, non-immunogenic and biodegradable linear polysaccharide, capable of chelating in the presence of divalent cations, such as Ca^{2+} , by generating inter-chain bridges [28]. Alginates are binary co-polymers of linked β -D-mannuronic and α -L-guluronic acid in varying order and molecular weight. The hydrogel is formed as blocks of guluronic acid bind to divalent cations, generating a three-dimensional network of alginate strands held together by ionic interactions [29]. Alginate has been extensively used in bioprinting [30], as it forms cell-friendly hydrogels that are easily extruded and exhibits fast gelation. Although not a component of articular cartilage, or the human body in general, alginate has been used as a bioink for cartilage bioprinting, usually in combination with another polymer [31–33].

Despite the tremendous potential that 3D bioprinting introduced to the tissue engineering field, it still suffers from certain drawbacks. For instance, the fabrication of tubular or curved living structures has been proved to be particularly challenging and usually requires the use of sacrificial materials and supports, introducing additional post-printing processing steps and, thus, increasing the total fabrication time [34, 35]. Furthermore, 3D bioprinted scaffolds are static and exhibit no dynamic response to external stimulation. Native ECM, on the contrary, is a highly dynamic structure that undergoes continuous, regulated remodelling [36]. Hence, in order to effectively mimic native tissues, biofabricated scaffolds should exhibit an equally dynamic behavior. The fabrication of tissues with such dynamic responses has recently become possible by 4D bioprinting, a novel technology that may solve the aforementioned challenges.

Four dimensional (4D) bioprinting is a newly emerged technology in tissue engineering that enhances the biomimicry of 3D bioprinted scaffolds by using smart materials capable of recapitulating the dynamic responses of physiological tissues against natural stimuli. 4D bioprinting uses the same fabrication principles as 3D bioprinting, whilst introducing an additional, post-printing phase, during which the application of one or more stimuli triggers the transformation of the printed structure. The applied stimuli can be a temperature change [37], immersion in aqueous solutions [38], electric [39] or magnetic stimulation [?] as well as light irradiation [40]). Transformation of the living scaffolds is exhibited as a change in either their shape or function. A schematic illustration of the shape-shifting 4D bioprinting is presented in Fig. 1. Irrespective of the transformation type in question, the two approaches share a common principle: the transition from one stable state (post-printing state) to a new, equally stable condition (post-transformation state).

Though still in its infancy, 4D bioprinting has already been used in a few studies, yielding promising results [38–41]. More specifically, Yang *et al.* presented a novel approach for the alignment of murine myoblasts in gelatine-based bioinks using an external electric field during printing [39]. Strands of bioink were aligned on a cell-free gelatine sheet which was capable of self-rolling, resulting in the formation of fibrous bundles. Gelatine and alginate-based bioinks laden with human embryonic kidney cells were used by Luo *et al.* for the fabrication of scaffolds that could change their shape upon near-infrared irradiation [40]. The shape morphing was enabled by the use of a cell-free “strut” made from alginate and polydopamine. In another study, alginate and HA sheets laden with mouse bone marrow stromal cells capable of self-folding into tubes were fabricated [41]. Finally, digital light processing was used along with a UV-curable silk fibroin hydrogel to fabricate patterned sheets capable of folding into tracheal-like implants laden with rabbit chondrocytes and turbinate-derived mesenchymal stem cells [38]. The same types of cells derived from humans were also used for *in vitro* studies.

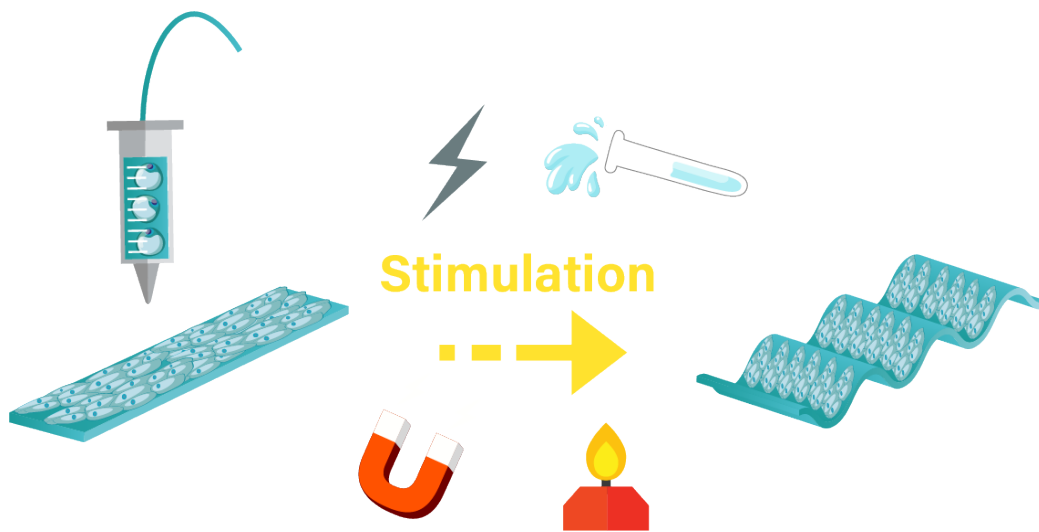


Figure 1: Schematic illustration of shape-shifting 4D bioprinting.

In this thesis, an advanced 4D bioprinting method based on multi-material extrusion of two hydrogel-based (bio)inks, is reported. This approach allows the fabrication of bilayered scaffolds made from a bottom part of a HA-Tyr precursor and a composite hydrogel top part from alginate and HA-Tyr (Alg/HA-Tyr), capable of self-bending upon immersion in a swelling solvent. The shape shifting of the scaffolds was driven by the different swelling capacities of the two inks. Control of the obtained curvature was achieved by tuning a range of parameters including the infill density and printing angle, the thickness of each layer, the CaCl_2 crosslinking time of the alginate component as well as the type of the swelling solvent. A qualitative model was established, providing a preliminary framework for predicting the final curvature of the structure, that could be used as a starting point for different 4D bioprinting applications. Incorporation of human mesenchymal stem cells (hMSCs) in the Alg/HA-Tyr composite hydrogel allowed the fabrication of living, self-bending scaffolds that could support cell survival for at least 14 days without a decrease in cell viability. Hence, this is one of the very few studies considering 4D bioprinting and, probably, the first to report incorporation of human-derived cells in bilayered scaffold made from two different, natural polymers.

2 Experimental Section

2.1 Reagents and Materials

Tyramine-substituted hyaluronic acid ($M_w=280-290$ kDa) was kindly provided by AO Research Institute (Davos, Switzerland) [20]. The degree of substitution was 6.6%, as determined by absorbance reading at 275 nm, described by Schwab *et al.* [42]. Sodium alginate ($M_w=75-200$ kDa) was purchased from NovaMatrix (Sandvika, Norway). Horseradish peroxidase (HRP), anhydrous calcium chloride (CaCl_2), sodium chloride (NaCl), hydrogen peroxide (H_2O_2), Alcian blue, Fetal Bovine Serum (FBS), Ascorbic Acid (AA), Insulin Transferring Selenic acid (ITS+), L-proline, Dexamethasone, Transforming Growth Factor- $\beta 1$ (TGF- $\beta 1$), Direct Red 80, Saturated Aqueous Solution of Picric Acid, Solid Picric Acid, DPX mountant, HARRIS Hematoxylin solution, Eosin Y solution, Acetic Acid (CH_3COOH), Hydrochloric Acid (HCl) were purchased from Sigma-Aldrich (St. Louis, Missouri, USA). Dulbecco’s Modified Eagle Medium (DMEM) used for preparing the custom chondrogenic medium (DMEM-HG, GlutaMAXTM, HEPES), α Minimum Essential Medium (α MEM), Fungizone (Amphoterycin B, AmpB), Sodium Pyruvate, Gentamicin, Calcein AM, Ethidium homodimer (EthD-1), PrestoBlueTM were purchased from ThermoFisher Scientific (Waltham, Massachusetts, USA). DMEM, trypsin EDTA, HEPES Buffered Saline Solution, Trypsin Neutralizing Solution (TNS), Human Mesenchymal Stem Cells (hMSCs) at passage 2 were purchased from Lonza (Basel, Switzerland). Recombinant Human Fibroblast Growth Factor (FGF2) and Trypan blue were purchased from BioRad (Hercules, California, USA). Xylene was purchased from Avantor (Radnor, Pennsylvania, USA).

2.2 Preparation of HA-Tyr and Alg/HA-Tyr Inks

For the preparation of 1 ml of HA-Tyr ink, 25 mg of HA-Tyr were mixed with 650 μl of 0.9% NaCl and 10 μl of 10 U/ml HRP using a two-syringe mixing method. The concentrations of HA-Tyr and H_2O_2 used for the preparation of the inks were selected based on a study from Petta *et al.* where a similar ink was reported to exhibit good printability [17]. Briefly, a “female-to-female” luer lock was attached to the tips of two syringes and the contents were thoroughly mixed. The formulation was left to be further mixed overnight at 4°C in a covered syringe placed on a thermal shaker (Thermal Shake *lite*, VWR, Leicestershire, UK). The following day, 170 μl of 0.9 % NaCl and 170 μl of 1 mM H_2O_2 were added to the formulation using the two-syringes method for mixing. Immediately after homogenizing, the ink was centrifuged for 5 min at $200\times g$ to remove air bubbles (Sigma 4-16KS, Sigma Laboratory Centrifuges, Osterode am Harz, Germany) and kept protected from light at room temperature for at least 30 min before printing, to ensure the enzymatic-mediated crosslinking was complete. The same preparation procedure was followed for the Alg/HA-Tyr composite ink, with the sole difference being the addition of 10 mg of sodium alginate in the initial formulation. In order to distinguish the two inks after combining them in the same scaffold and facilitate the quantification of the obtained curvature, 30 μl and 10 μl of Alcian blue (1% w/v) were mixed in the Alg/HA-Tyr and the HA-Tyr inks, respectively, before printing. The concentrations of the individual components of the two inks are summarized in [Table 1](#).

Table 1: Composition of HA-Tyr and Alg/HA-Tyr inks. (+) and (-) symbols indicate the presence or absence of the material, respectively.

Material	Concentration	HA-Tyr	Alg/HA-Tyr
HA-Tyr	25 mg/ml	+	+
Alginate	10 mg/ml	-	+
HRP	0.1 U/ml	+	+
NaCl	0.9%	+	+
H ₂ O ₂	0.17 mM	+	+

2.3 Rheological Characterization

Rheological properties are the physicochemical parameters which largely affect the printability and shape-fidelity of a hydrogel-based ink. Rheological measurements provide an overview of the flow and deformation behavior of the tested material under shear loading [43]. In extrusion bioprinting, the ink undergoes a three-state transition: from a resting, bulk state in the printing cartridge, to a condition of high-shear exposure, while passing through the nozzle, to a new, resting state, in which its shape has been changed to that of a filament [12]. The rheological parameters which are critical for the prediction of the ink's behavior during the aforementioned transitions are: the viscoelastic shear moduli, the viscosity, the elastic recovery and the yield stress [44]. The important rheological parameters for each state are illustrated in Fig. 2.

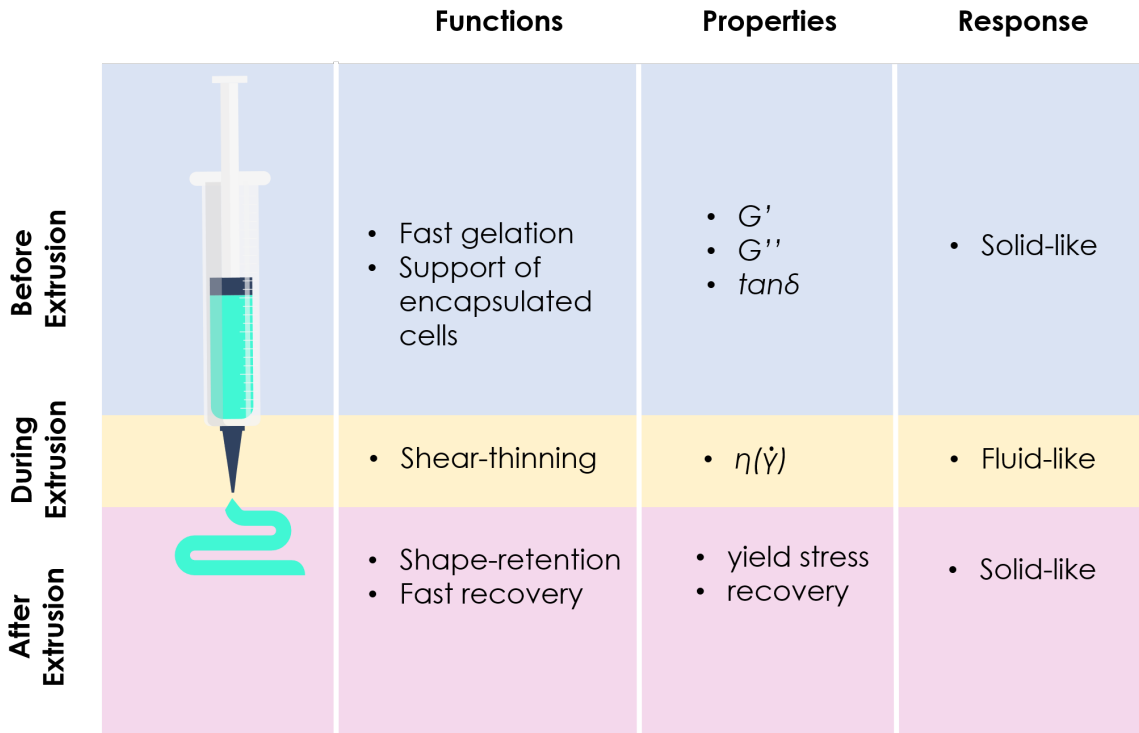


Figure 2: Schematic illustration of the three-state transition of an ink during extrusion. Figure abbreviations: G' : storage modulus, G'' : loss modulus, $\tan\delta$: damping factor, η : viscosity, $\dot{\gamma}$: shear rate.

In extrusion bioprinting, inks should, ideally, flow under the application of pressure,

without displaying a significant flow resistance that could negatively affect cell viability. Upon removal of extrusion shear, immediate recovery of the hydrogel is desired, in order to achieve the formation of a filament capable of retaining its shape, enabling encapsulated cells to remain localized upon filament deposition. The combination of viscous flow and elastic shape retention can be described by the two shear moduli: the storage (or elastic) modulus, G' , and the loss (or viscous) modulus, G'' . The storage modulus, G' , is a measure of the deformation energy stored by the material during shear loading. Upon load removal, this energy is the driving force for shape retention which compensates, partially or fully, the deformation underwent by the material during loading. Thus, G' , represents the elastic behavior of the material and is associated with the post-printing shape-fidelity of the ink. The loss modulus, G'' , is a measure of the deformation energy dissipated by the material during shear loading, caused by frictional forces between molecules or even greater domains of the hydrogels [43]. Therefore, G'' is associated with the viscous flow of the inks. The ratio of the viscous and the elastic portion of the ink is determined by the damping factor, $\tan \delta = \frac{G''}{G'}$. Apart from the storage modulus, the shape fidelity of a material can also be determined by its yield point which was measured using a strain sweep test. The yield point, *i.e.*, the threshold stress value that has to be exceeded for flow to occur, was determined as the stress value corresponding to the intersection of the $G'(\gamma)$ and $G''(\gamma)$ curves.

Viscosity is the flow resistance occurring for a fluid in motion and is caused by the internal frictional forces which develop due to the relative motion of the fluid's molecules [43]. For extrusion bioprinting, a higher ink viscosity usually results in an increased shape fidelity. However, a material with high viscosity will experience higher shear stress during extrusion bioprinting, compared to a less viscous ink, which could affect the viability of the encapsulated cells. Therefore, inks exhibiting shear thinning, *i.e.*, their viscosity decreases with increasing shear rate have become an attractive option for cell-compatible extrusion of a bioink through a small orifice (needle or nozzle).

Rheological measurements were performed using two Anton Paar Physica MCR 501 rheometers (Anton Paar, Graz, Austria), equipped with a thermostatic hood and a Peltier element for temperature control. A cone-plate geometry (diameter: 30 mm, angle: 1°) was used and the temperature was set to 21°C , to mimic the conditions of crosslinking and printing at room temperature. To prevent dehydration, a low viscosity mineral oil was deposited on the perimeter of the samples and milli-Q water was added in the circular groove surrounding the measuring platform, to create a vapor-saturated environment. Five different tests were performed for each sample. Each hydrogel was mixed with H_2O_2 and immediately loaded on the rheometers. Polymerization progress of the samples was recorded using a small-amplitude oscillatory test, by measuring the time dependence of the storage and loss moduli (G' and G'' respectively). The duration of the test was set to 1 h (3600 s) with a 5 s interval between consecutive measurements (720 measuring points). The frequency and strain were kept constant at 0.5 Hz (π rad/s) and 0.5% respectively. The frequency dependence of the samples was investigated through a frequency sweep test, by measuring G' and G'' for 20 frequency values, logarithmically spaced in a range from 0.01 Hz (0.02π rad/s) to 10 Hz (20π rad/s). Similarly to the first test, the strain amplitude was kept constant at 0.5%. Subsequently, a shear stress ramp from 0.01 Pa to 20 kPa with a slope of 20 points per decade was applied to the sample in order to measure its viscosity, η , under increasing shear. Finally, a second stress ramp from 1 Pa to 5 kPa (51 logarithmically spaced measuring points) was applied to the materials to identify their yield stress as the point where the G' and G'' curves intersect, under increasing shear strain. Immediately after the strain sweep stress, an oscillatory thixotropy test was performed for a constant

strain value of 0.5% to study the recovery of the material after the exposure to high shear strain. The frequency was set to 0.5 Hz for both the strain sweep and the oscillatory thixotropy tests. The first three measurements described above were performed on the same sample as consecutive tests of the same process, using the RheoPus software (Anton Paar, Graz, Austria). After the shear stress sweep, the samples had reached their breaking point and could not be used for further analyses. Therefore, for the last two measurements, a new, fully crosslinked sample of the same material was loaded on the rheometers. In total, three measurements were performed for each material, using newly prepared inks and employing both rheometers, yielding a total of six ($n = 6$) data sets per test. The data were processed with MATLAB R2020b and plotted using GraphPad Prism version 9.1.1. for Windows (GraphPad Software, SanDiego, California USA).

2.4 Shear Thinning Modeling

The linear region of the $\eta(\dot{\gamma})$, plot was characterized using the Ostwald-de Waele power law equation for apparent viscosity [45]:

$$\eta = K\dot{\gamma}^{n-1} \quad (1)$$

where K and n are constants of the model. Based on the value of n , materials are characterized as: shear-thinning for $n < 1$, Newtonian for $n = 1$ and shear thickening for $n > 1$ [43]. Model fitting was performed using the Curve Fitting ToolboxTM for MATLAB R2020b.

2.5 Multi-material 4D printing

HA-Tyr and Alg/HA-Tyr precursors were used for printing bilayered scaffolds with various designs, including a basic rectangular scaffold and flower-, star-, and cross-shaped structures. CAD models of the scaffolds were designed using TinkerCAD (Autodesk, San Rafael, California, USA) and exported as STereoLithography files (STL). Subsequently, the STL documents were sliced using the open-source slicing software Cura Ultimaker 4.7 and exported as 3D objects (.3mf). The following slicing parameters were used: layer height: 0.25 mm; wall thickness: 0 mm for rectangular scaffolds, 0.25 mm for flower-, star- and cross-shaped scaffolds; infill density: 40%, 50%, 60%; infill pattern: zig-zag; infill line directions: $[0^\circ, 90^\circ]$ and $[90^\circ, 0^\circ]$ for rectangular scaffolds and $[45^\circ, 135^\circ]$ for flower-, star- and cross-shaped scaffolds; speed: 10 mm/s; cooling: off; plate adhesion: off. The 3D objects were then imported to CAMotics v.1.2.0. open-source software and the G-code of each design was generated. Finally, the G-codes were imported to a BIO X 3D bioprinter (Cellink, Göteborg, Sweden) (Fig. 3a).

Two cartridges equipped with 25G nozzles (32 mm length, 500 μm inner diameter at the top, 250 μm inner diameter at the tip) were used for the fabrication of the bilayered scaffolds (Fig. 3b). The pressure was set to 40 Pa for the HA-Tyr ink and to 50 Pa for the Alg/HA-Tyr ink. The optimal printing speed was defined at 10 mm/s for both materials with the aforementioned pressure values (Fig. 3c). Both the printing platform and the chamber were kept at room temperature. All scaffolds were printed in 35 mm \times 10 mm petri dishes (Greiner Bio-One GmbH, Frickenhausen, Germany) to minimize scaffold handling during post-printing steps. Directly after printing, 3 ml of 200 mM CaCl_2 were added in the dish

to crosslink the alginate component of the Alg/HA-Tyr layer of the scaffold. After 10 min the solution was removed and the scaffolds were washed twice in 3 ml 0.9% NaCl for 5 min. For the self-bending experiments, bilayered scaffolds were left in 3 ml of different solutions, including DMEM, deionized H₂O, 0.9% NaCl with 2 mM CaCl₂, 0.9% NaCl, 5% NaCl and 10% NaCl, in ParafilmTM sealed dishes, at room temperature, for up to 24 h.

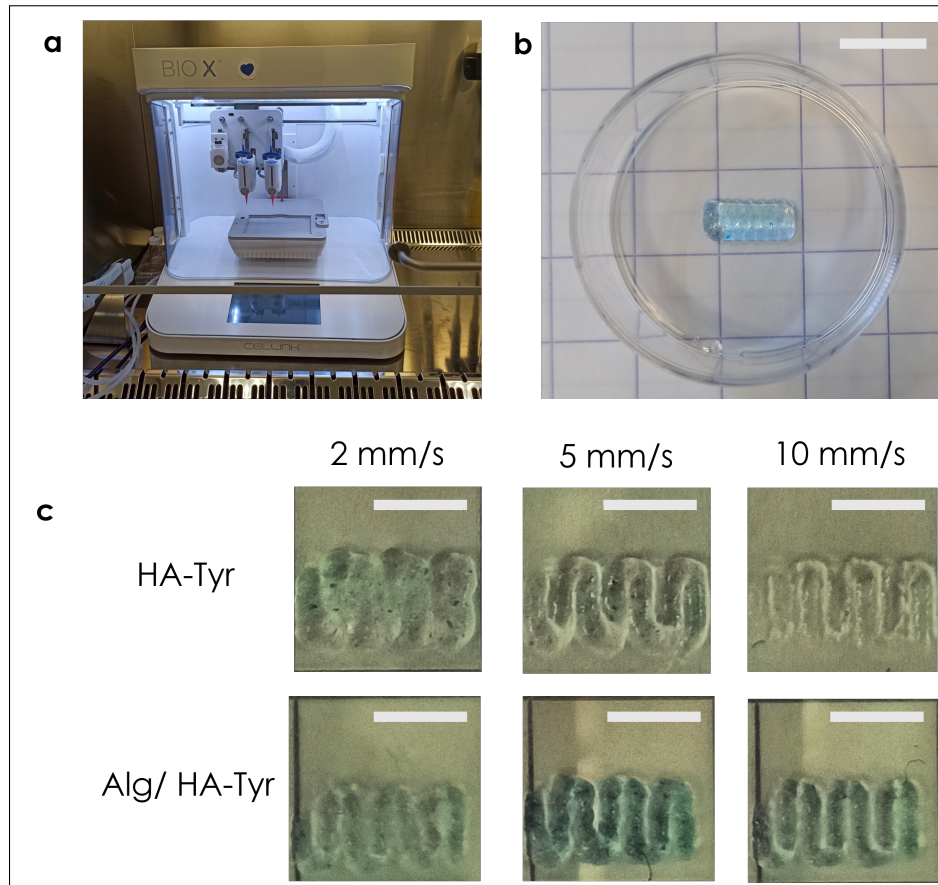


Figure 3: Printing Setup. (a) The bioprinter in the biosafety cabinet with two cartridges equipped with the 25G nozzles. (b) Top view of a bilayered scaffold sample. Scale bar: 10 mm. (c) Printing speed tests with 2 mm/s (left), 5 mm/s (middle) and 10 mm/s (right) for HA-Tyr (top) and Alg/HA-Tyr (bottom). Scale bars 5 mm.

The initial rectangular scaffold design consisted of two HA-Tyr layers followed by two Alg/HA-Tyr layers, three different infill densities, namely 40% (Fig. 4a, d), 50% (Fig. 4b, e) and 60% (Fig. 4c, f), and two printing patterns, namely 0° – 90° (Fig. 4a-c) and 90° – 0° (Fig. 4d-f), were used. Infill density defines the amount of ink used to fabricate a printed structure. In other words, an infill density of 40% means that the extruded material will occupy 40% of the designed construct, while the rest 60% will be void. The printing patterns mentioned above correspond to the main printing direction per layer with 0° representing the transverse ($x = 0$) and 90° the horizontal ($y = 0$) printing directions with respect to the x-y plane. For instance, the 0° – 90° pattern refers to a construct consisting of a bottom layer printed on the transverse direction, followed by a layer printed on the horizontal direction and so on (Fig. 4g). The 90° – 0° pattern uses the opposite printing angles and is illustrated in Fig. 4h.

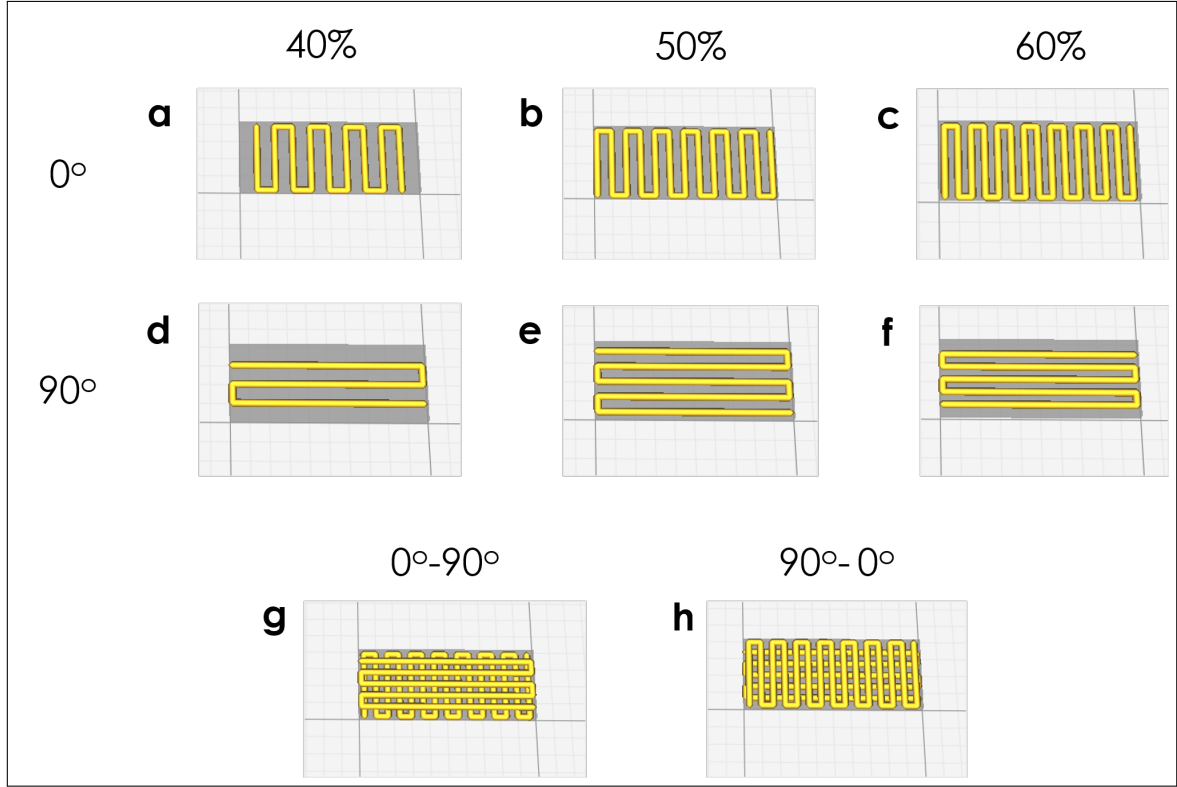


Figure 4: Infill Density and Printing Angle Combinations. (a-c) Illustrations of a single layer printed with a 0° printing angle and (a) 40%, (b) 50%, (c) 60% infill densities. (d-f) Illustrations of a single layer printed with a 90° printing angle and (d) 40%, (e) 50% and (f) 60% infill densities. (g, h) Illustrations of two layers printed with (g) the 0° - 90° combination and (h) the 90° - 0° combination. The infill used for the last two illustrations was 60%.

2.6 Compression Tests

Compression tests of single-material scaffolds were performed at ambient conditions using a motorized compression test stand (ESM303, Mark-10, Copiague, NY, US) equipped with a 2-inch parallel plate geometry at a compression speed of 2 mm/min (Fig. 5a). Test samples with dimensions of 10 mm \times 4 mm \times 1.5 mm were printed for each material. Both HA-Tyr and Alg/HA-Tyr scaffolds were measured after a 10-min immersion in 3 ml of 200 mM CaCl_2 and two subsequent washing steps with 0.9% NaCl, to imitate the post-printing processing of the bilayered scaffolds. Moreover, increased CaCl_2 times of 15, 20 and 25 min were also applied for the Alg/HA-Tyr constructs. After washing, every scaffold was placed on a glass slide and any excess liquid was carefully cleaned using a paper tissue (Fig. 5b, c). The thickness of the structures was measured using a digital caliper at $n \geq 3$ sites. The contact surface of each structure was measured with Fiji [46], using top-view pictures of the scaffolds acquired right before each scaffold was loaded to the compression stand. The stress was calculated as the load output divided by the measured contact surface of each scaffold and the strain was exported from the travelled distance of the moving (top) plate of the instrument. The starting point of compression was defined as the distance between the two plates for which the measured load had the minimum (positive) value. Finally, the compressive modulus, E , was determined by linear fitting ($R^2 > 94\%$) of the stress-strain

curve, in the strain region between 0% and 20%, to avoid the introduction of errors due to bulging of the hydrogels at higher strain values. Samples were prepared in triplicate ($n = 3$) for each condition.

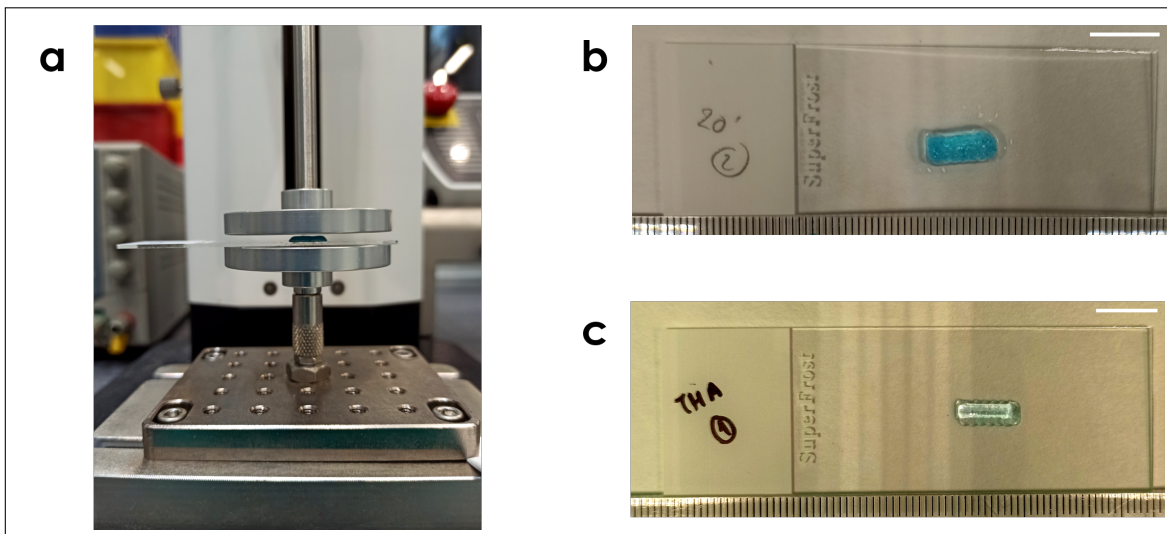


Figure 5: Compression Tests. (a) The compression test setup. A glass slide with a test sample has been placed between the 2-inch parallel plates. (b) Alg/HA-Tyr and (c) HA-Tyr scaffolds for compression tests. Scale bars: 10 mm.

2.7 Swelling Studies of Single Material Scaffolds

For the determination of the mass swelling ratios, SR_m of the inks, single-material test scaffolds with dimensions of $10 \text{ mm} \times 4 \text{ mm} \times 0.5 \text{ mm}$ were prepared. Directly after printing, the scaffolds were weighted using an analytical balance (AA-160, Denver Instrument, Bohemia, NY, US). Subsequently, all scaffolds were immersed in 3 ml of 200 mM CaCl_2 for 10 min, washed twice in 3 ml 0.9% NaCl for 5 min and then left in 3 ml of swelling solvent for up to 24 h to reach a swelling equilibrium. Each sample was weighed 2 h and 24 h after printing and then it was promptly returned to its dish. The mass swelling ratios, SR_m , were determined by the following formula:

$$SR_m = \frac{m_{swollen} - m_{dry}}{m_{dry}} \quad (2)$$

where, $m_{swollen}$ is the mass of the scaffold after 2 or 24 h in solvent and m_{dry} is the mass of the scaffold after printing. Scaffolds were prepared in triplicate ($n = 3$) for each condition.

2.8 Curvature Analysis

For the curvature analysis, side-view photos of the scaffolds in 35 mm petri dishes were acquired after 2 and 24 h in the swelling solvent and the images were processed using the Kappa plugin for Fiji (NIH) [46]. Three different curves were defined for each scaffold which

were traced manually using 10 points per curve and the curvature (κ) was calculated using a B-spline method. The curvature, κ , is defined as:

$$\kappa = \frac{1}{\rho} \quad (3)$$

where ρ is the radius of the circular arc that best approximates the curve of the scaffold. The average κ value of the three curves was selected as the curvature of the scaffold. Three scaffolds were used per condition ($n = 3$).

2.9 Self-bending Model

The design of the scaffold and the sequence of material deposition was based on a qualitative model, which was inspired by the Timoshenko beam theory [47]. This theory considers the deflection of a bi-metal strip under uniform heating and has already been used as a starting point for predicting scaffold deformation in 4D printing studies [48–50]. Briefly, if the two metals possess different expansion coefficients, k , bending of the strip will occur upon heating, described by the following formula:

$$\kappa = \frac{1}{\rho} = \frac{6(k_2 - k_1)(t - t_0)(1 + m^2)^2}{h[3(1 + m)^2 + (1 + mn)(m^2 + \frac{1}{mn})]} \quad (4)$$

where κ the curvature and ρ the radius of curvature of the bi-metal beam, k_1, k_2 the coefficients of thermal expansion of the two materials, t_0 and t the original and final temperatures of the beam, respectively, $m = \frac{a_1}{a_2}$ the ratio of the thickness values of the two layers, $n = \frac{E_1}{E_2}$ the ratio of elasticity moduli of the two layers and h the total thickness of the beam. The numbers 1 and 2 correspond to the cross-section of the beam presented in Fig. 6a. More specifically, if the expansion coefficient of the bottom material is larger than that of the top material, the deflection will be convex down (Fig. 6b). In order to establish an analogy between the swelling-induced bending and the Timoshenko theory, the following key assumptions were made:

1. Instead of a temperature increase, the driving force of bending is the immersion of the scaffold in swelling solvent.
2. The coefficient of thermal expansion is analogous to the linear expansion ratio, λ , defined as the cube root of the volumetric swelling ratio, SR_v , assuming isotropic swelling of the hydrogel inks.
3. Unlike the original Timoshenko theory, the width of the scaffold is significant in comparison to its length (length to width ratio is 2.5:1), however its effect on the shape-shifting is beyond the scope of this thesis and will not be considered.

Additionally, the elastic modulus of a swollen polymer network, E , can be defined by the linear expansion rate of the network, λ , after swelling, and the modulus of the dry network, E_0 , as $E \approx E_0\lambda^{-1}$ [51]. Furthermore, from swollen network thermodynamics, the elastic modulus of the dry network can be determined using the linear expansion rate, λ , as $E_0 \approx \lambda^{-v}$, where v is 5.25 and 8 for highly and less swollen networks, respectively [52]. Therefore, $E \approx \lambda^{-\alpha}$ and n can be defined as:

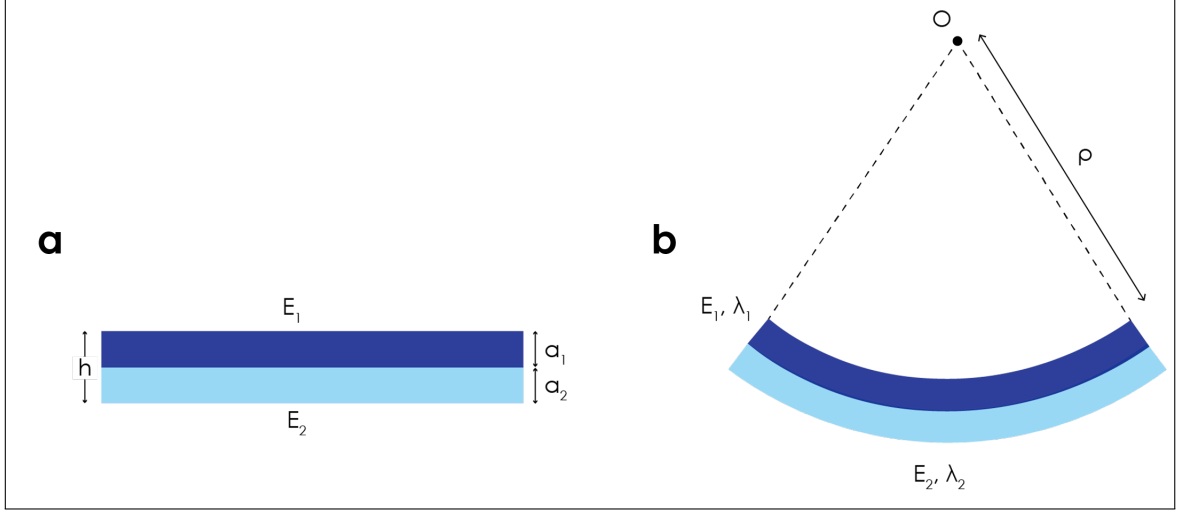


Figure 6: Graphic illustration of the swelling induced bending of bilayered structure (cross-section view). The bilayered beam before, (a), and after bending (b). Figure nomenclature: h : the total thickness, α_1, α_2 : the thickness of the top and bottom layer, respectively, E_1, E_2 : the compressive moduli of the top and bottom layer, respectively, λ_1, λ_2 : the linear expansion rate of the top and bottom layers, respectively, ρ : the radius of curvature.

$$n \approx \left(\frac{\lambda_2}{\lambda_1}\right)^\alpha \quad (5)$$

where $\alpha = v + 1$ is considered a model coefficient and is assumed constant for both the HA-Tyr and Alg/HA-Tyr inks [50].

By eliminating the $(t-t_0)$ term of the original equation which introduces the temperature increase in the model, the following rough estimation can be extracted from Equation 4 for the behavior of the bilayered hydrogel scaffolds:

$$\kappa = \frac{1}{\rho} \sim \frac{6(\lambda_1 - \lambda_2)(1 + m)^2}{h[3(1 + m)^2 + (1 + m)\left(\frac{\lambda_2}{\lambda_1}\right)^\alpha(m^2 + \frac{\lambda_1^\alpha}{m\lambda_2^\alpha})]} \quad (6)$$

2.10 Cell Studies

2.10.1 Cell Thawing And Plating

Frozen hMSCs (Passage 4) were thawed and plated for expansion 14 days before bioprinting. Briefly, frozen 1 ml aliquots containing approx. 10^6 cells were thawed by immersion in a water bath (37°C) for 1.5 min and gently mixed with 10 ml of expansion medium. Subsequently, hMSCs were centrifuged at $200\times g$ for 5 min in order to form a pellet. The supernatant liquid was discarded and the pellet was gently suspended in 1 ml of expansion medium. Next, 20 μl of the suspension were mixed with 20 μl of trypan blue and loaded on a cell-counting cover slip (BioRad) (double-sided, 10 μl per side). An automated cell counter (TC20TM, BioRad) was used to count the number of viable cells per milliliter of

suspension. Upon calculating the total cell number, hMSCs were seeded at ≈ 3000 cells/cm² in 175 cm² flasks (Thermo-Fisher Scientific) containing 20 ml of expansion medium (5×10^5 cells/flask). During the 14 days of culturing, the density of hMSCs was assessed regularly to ensure they did not reach a high confluence rate. The expansion medium consisted of α MEM, fungizone (1.5 μ g/ml), gentamicin (50 μ g/ml), FBS (10% v/v), AA (29 μ g/ml) and FGF2 (1 ng/ml). The medium was refreshed every three days.

2.10.2 Trypsinization

Confluent hMSCs cultured in 175 cm² flasks were trypsinized to be used either for bioprinting or other experiments described below. Briefly, each flask was washed twice using a HEPES buffered saline solution (10 ml per washing step) and then incubated at 37°C (5% CO₂, 90% humidity) for 5 min with 10 ml of trypsin/EDTA solution. After incubation, each flask was gently tapped to aid the detachment of hMSCs which was, then, assessed using a fluorescence microscope (ZOETM Fluorescent Cell Imager, Biorad). Upon confirming cell detachment, the hMSCs-containing trypsin solution was collected in a 50 ml falcon tube. Subsequently, the flask was washed twice with 5 ml of trypsin neutralizing solution (TNS) which was also collected in the same falcon tube. The hMSCs-trypsin-TNS solution was centrifuged at $200 \times g$ for 5 min to induce pellet formation. Pellet suspension, and cell counting were performed as described in the previous section.

2.10.3 Pellet Preparation and Culture

hMSCs were plated as previously described and cultured in expansion medium for three days. On the fourth day, cells were trypsinized and centrifuged at $200 \times g$ for 5 min. The supernatant liquid was discarded and the formed pellet was suspended in 2 ml of culture medium in order to count its cell content. Subsequently, the suspension was divided into sterile 1.5 ml Eppendorf tubes (2×10^5 hMSCs/tube) and the tubes were centrifuged at $200 \times g$ for 5 min. The supernatant medium was discarded and replaced with 0.5 ml of fresh chondrogenic medium and the tubes were transferred to the incubator (37°C, 5% CO₂, 90% humidity). The medium was changed every three days up to day 21. In total, 18 pellets were prepared.

2.10.4 Media Preparation

Two different media were used for the pellet study, in order to assess the optimal chondrogenic induction medium to use with the bioprinted scaffolds. The first medium, hereinafter referred to as CM-L, was purchased from Lonza (Basel, Switzerland) and prepared according to the manufacturer's instructions. Briefly, aliquots (SingleQuotsTM) containing dexamethasone, AA, ITS+, GA-1000, sodium pyruvate, proline and L-glutamine were added to 185 ml of hMSC differentiation basal medium to prepare the incomplete chondrogenic induction medium. Before adding it to the pellets, TGF- β 3 was added to the volume of medium needed for refreshing to reach a concentration of 10 ng/ml, in order to prepare the complete CM-L. The second medium, hereinafter referred to as CM-E, was prepared according to a protocol from Narcisi *et al.* [53]. ITS+ (10 \times), L-Proline (40 μ g/ml), sodium pyruvate (1 mM), fungizone (1.5 μ g/ml) and gentamicin (50 μ g/ml) were

mixed with DMEM-HG, GlutaMAXTM, HEPES to prepare the incomplete CM-E. TGF- β 1 (1 ng/ml), dexamethasone (100 nM) and AA (29 μ g/ml) were added fresh before each use (complete CM-E). Six pellets were used per medium and the remaining six were used as day 2 controls.

2.10.5 CaCl₂ Effect on hMSCs

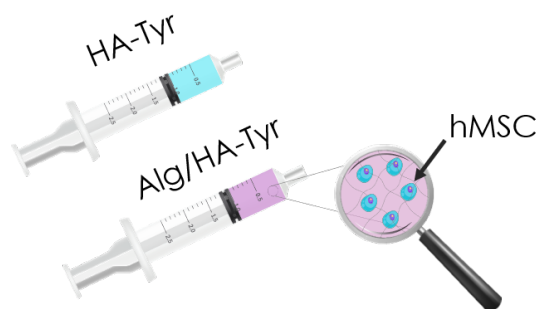
Before the start of the bioprinting experiments, the effect of CaCl₂ on hMSCs was investigated. Solutions of 100 mM, 200 mM and 300 mM of CaCl₂ in 1 \times PBS were prepared and sterilized by filtration (0.2 μ m syringe filters). hMSCs cultured in monolayers in a 48-well plate for 14 days were washed twice using 100 μ l of 1 \times PBS (5 min per wash). Subsequently, hMSCs were incubated at room temperature with 100 μ l of the aforementioned CaCl₂ solutions for 10, 15, 20 and 25 min ($n=3$ per time-point and concentration value). Wells without any CaCl₂ exposure were used as controls ($n=3$).

2.11 4D Bioprinting

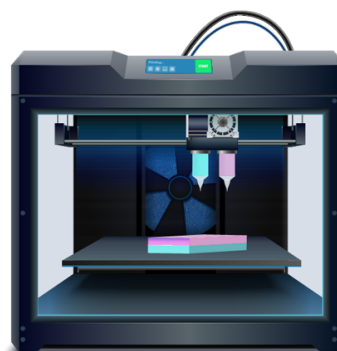
For bioprinting studies, the bioprinter was moved to the biosafety cabinet after being thoroughly sterilized with 70% ethanol. Subsequently, the printer was programmed to run a 5-min UV sterilization cycle in order to sterilize the printing chamber. Moreover, a longer UV sterilization cycle (approx. 20 min) was performed using the UV setting of the biosafety cabinet, to ensure the external part of the printer was completely sterile. For the preparation of 1 ml of HA-Tyr ink, 25 mg of UV-sterilized HA-Tyr powder were mixed with 650 μ l of sterile 0.9% NaCl and 10 μ l of 10 U/ml sterile HRP using the two-syringe mixing method described above. The formulation was left to be further mixed overnight at 4°C in a covered syringe placed on a thermal shaker. The following day 170 μ l of sterile 0.9% NaCl and 170 μ l of 1 mM sterile H₂O₂ were mixed with the ink. Immediately after homogenizing, the ink was centrifuged for 5 min at 200 \times g to remove air bubbles and kept protected from light in the biosafety cabinet at room temperature for at least 30 min before printing. The same preparation procedure was followed for the Alg/HA-Tyr ink, with the only difference being the addition of 10 mg of sterile sodium alginate powder in the initial formulation (first day). Subsequently, hMSCs were trypsinized, counted and suspended in a volume of medium equal to 10% of the total bioink volume. Two cell densities were used, namely 5 \times 10⁶ cells/ml and 6.5 \times 10⁶ cells/ml, each for one of the two bioprinting studies performed. The suspension was added in the Alg/HA-Tyr formulation and gently mixed using two coupled syringes. Upon mixing, the two inks were loaded in printing cartridges equipped with 25G nozzles and scaffolds were printed in 12-well plates. Subsequently, 3 ml of sterile CaCl₂ (200 mM) were added in the wells for 10 min. The solution was then discarded and the scaffolds were washed twice with 0.9% NaCl (3 ml per washing-step, 5 min each). Finally, 3 ml of medium (either expansion or chondrogenic, depending on the study) were added in each well and the plates were stored in the incubator (37°C, 5% CO₂, 90% humidity). The medium was refreshed every 3 days. A step-by-step illustration of the 4D bioprinting process is presented in Fig. 7. All the processes described above were performed under sterile conditions and all the necessary equipment was either already sterile (*e.g.*, syringes, well plates) or sterilized by autoclaving at 120°C for 2 h (*e.g.*, nozzles, cartridges, Luer locks).

Step 1: Bioink Preparation

HA-Tyr and Alg/HA-Tyr inks are precrosslinked with H_2O_2 . The Alg/HA-Tyr ink is then mixed with hMSCs.

**Step 2: 3D Bioprinting**

HA-Tyr ink and Alg/HA-Tyr bioink are loaded to the printer and a rectangular bi-layered scaffold is fabricated.

**Step 3: Secondary crosslinking**

The scaffold is immersed in a $CaCl_2$ solution to induce the secondary crosslinking of Alg/HA-Tyr

**Step 4: Swelling**

The scaffold is immersed in chondrogenic differentiation medium

**Step 5: Self-Bending (4D)**

The different swelling behavior of the two layers causes the scaffold to bend

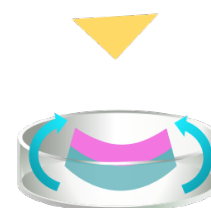


Figure 7: 4D bioprinting of self-bending bilayered scaffolds.

2.12 Cell Assays

2.12.1 Presto Blue™ Assay

Measurements of the PrestoBlue reduction after 1, 7 and 14 days of culture were used as indicators of the cell metabolic activity using fluorescence measurements. PrestoBlue was added to medium at a final concentration of 10% and 1ml of the solution was added to the scaffold-containing wells ($n = 3$). The scaffolds were incubated for 1h at 37°C (5%CO₂, 90% humidity). Subsequently, 100 μ l of medium for each sample were transferred into a 96-well plate in triplicates ($n = 3$). Samples without scaffolds (or pellets) served as blanks. The fluorescence (Relative Fluorescent Unit, RFU) was read at 570 nm using a microplate reader (PerkinElmer, Massachusetts, US). Corrected RFU was calculated by subtracting the average blank well value from the measured value of the scaffold-containing wells and presented as mean \pm 1 standard deviation.

2.12.2 Live/Dead Assay

A Live/Dead™ Viability/ Cytotoxicity kit (Thermo Fisher Scientific, Waltham, Massachusetts, USA) was used to assess the viability of hMSCs on day 1, 7 and 14 and the assay was prepared according to the protocol provided by the supplier. Briefly, stock solutions of calcein-AM and ethidium homodimer-1 (EthD-1) were thawed and a staining solution containing calcein-AM (2 μ M) and EthD-1 (3 μ M) in sterile 0.9% NaCl was prepared.

For bioprinting experiments, scaffolds ($n = 3$) were washed twice with sterile 0.9% NaCl (5 min per wash) and 1 ml of the staining solution was added to each well. Subsequently, the samples were incubated for 30 min protected from light at room temperature (20-25°C).

For 2D monolayers of hMSCs exposed to CaCl₂, each well was washed with 100 μ l of 1×PBS to remove the remaining CaCl₂ before the addition of 100 μ l of the staining solution. An incubation time of 30 min at room temperature was used.

Cell viability was assessed using a fluorescence microscope. Imaging of live cells, stained by calcein-AM, was performed using the green channel while dead cells, stained by EthD-1, were imaged using the red channel. Quantification of live and dead cells was performed using Fiji [46] following the protocol suggested by Allevi (Philadelphia, US) [54]. Briefly, raw images were transformed to 8-bit type and background noise was minimized using the Brightness/Contrast adjustment. Subsequently, image segmentation was performed using the Threshold setting. To separate cells in close proximity appearing as one, the image was subjected to a watershed segmentation process [55] and the result was then visually assessed to ensure optimal division. Finally, live and dead cells were counted automatically, using the “Analyze Particles” option. The size range was set to 100–1000 μ m² for live cells and to 20–400 μ m² for dead cells. The aforementioned ranges were selected based on the smaller and larger average diameters reported for hMSCs (for the live count) cultured in 3D spheroids [56] as well as for nuclei (for the dead count) [57]. Circularity range was set to 0.00–1.00 to include all particle morphologies present in each image. Finally, although the cells were counted by the software, the result was assessed visually to prevent counting errors. Viability was calculated as the ratio of live cells to the number of total cells and presented as mean \pm 1 standard deviation for multiple images ($n = 3$) per scaffold.

Area and circularity were the shape descriptors that were used to characterize the shape of the imaged cells. Both shape descriptors were calculated using Fiji. The area of each detected particle was first calculated and, based on that value, circularity was extracted from the software using the following formula:

$$Circularity = 4\pi \times \frac{Area}{Perimeter^2} \quad (7)$$

with a value of 1 indicating a perfect circle and a value approaching 0 indicating an increasingly elongated shape.

2.13 Histological Analysis

In order to assess the tissue formation and cell distribution as well as the chondrogenic capacity of the hMSCs used, histological analysis of the pellets, which were prepared as described in the *Pellet Preparation and Culture* section, was performed. Moreover, the tissue morphology as well as the presence of GAGs and collagen in the 4D bioprinted scaffolds was investigated after 14, 21 and 28 days post-fabrication.

2.13.1 Fixation

Pellets were fixed after 2 and 21 days of culture. Six pellets were fixed per condition, *i.e.*, 6 pellets on day 2 to serve as controls, 6 CM-E cultured pellets on day 21 and 6 CM-L-cultured pellets on day 21, as well. For the fixation, pellets were washed twice with 1×PBS before being fixed in 0.5 ml of 4% Paraformaldehyde (PFA) fixative. Subsequently, they were incubated overnight at 4°C. The following day, PFA was replaced with 1×PBS and the pellets were kept at 4°C until further use.

Scaffolds were fixed after 2, 3 and 4 weeks of culture. Scaffolds were washed twice with 0.9% NaCl before being fixed in a PFA-Glutaraldehyde-Cetylpyridinium chloride (CPC) solution (2% PFA, 2.5% Glutaraldehyde, 0.9% NaCl, 0.5% CPC, 50 mM CaCl₂). The scaffolds were incubated overnight in the fixative at 4°C and were subsequently washed twice with 0.9% NaCl. Finally, the scaffolds were stored in 50 mM CaCl₂ at 4°C. Three scaffolds were fixed per condition ($n = 3$).

2.13.2 Agarose Embedding

Agarose powder was mixed with deionized water (2% w/v) in a glass beaker and the solution was left to actively mix at 90°C on a magnetic, thermal mixer until the contents were homogenized. Covering the beaker with foil prevented water evaporation during mixing. Pellets were removed from 1×PBS and gently dried on a paper tissue. Subsequently, each pellet was placed on a metal histology tray and the agarose mixture carefully poured on top. The trays were left to cool at room temperature, until the agarose solution turned into a stiff gel. Then, the pellet-containing gels were carefully removed from the metal trays and excess gel was removed using a scalpel, until a small, cubic construct (approx. 5×5×5 mm³) was formed.

2.13.3 Dehydration

Cubic agarose constructs as well as fixed scaffolds were placed in histology cassettes before dehydration. The cassettes were placed in a container and the dehydrating solutions were successively changed according to the protocol. The dehydration steps are presented in [Table 4](#) (see [Appendix F](#)).

2.13.4 Paraffin Embedding

Paraffin beads (Surgipath Paraplast, Leica Biosystems, Wetzlar, Germany) were placed in two wax melting devices and the temperature was set to 60°C. When the dehydration process was complete, the histology cassettes were removed from xylene and placed in one of the melting devices for 60 min. The reason for using two different melting devices was to minimize the presence of xylene residues in the final embedded samples. Xylene melts paraffin and, if not removed from the wax, it could result in unstable samples. Metal moulds were put on a heated surface and the temperature was set to 60°C. After the cassettes had been left in the wax for one h, they were removed and opened. Fresh wax (from the second melting device) was poured in the moulds and the dehydrated agarose structures containing the pellets were carefully placed in the melted wax of the moulds. The plastic lid of the histology cassettes was removed and the bottom part was placed on top of the metal mould where it was secured by the addition of more wax. Subsequently, the samples were removed from the heated surface and left to cool at room temperature. After the paraffin had hardened the trays were kept at 4°C until slicing.

2.13.5 Slicing

Slicing of the wax-embedded samples was performed using a manual rotary microtome (HistoCore, BIO CUT, Leica Biosystems, Wetzlar, Germany). The moulds were placed in the freezer (-20°C) prior to slicing to facilitate the removal of the wax block from the mould as well as the slicing per se. A water bath was prepared and the temperature was set at 45°C. The clearance angle was set to 3° and a 6 µm slicing thickness was selected. Each wax block was removed from the mould and secured in the specimen holder of the microtome. The blade of the instrument was placed as close as possible to the surface of the wax specimen and slicing was performed, using a rotational lever. Ribbons of successive wax slices were collected and placed on the water bath for 2-3 min, until “relaxation” of the slices due to thermal expansion was observed. Subsequently, glass slides were used to collect the wax slices. At least three wax slices from different sample regions were collected per slide and three slides were prepared per sample (one for each stain). After slicing was performed for all the samples, the glass slides were left to dry overnight in an oven at 37°C.

2.13.6 Staining

Three different histochemical stainings were performed for the agarose-embedded pellets, namely Picrosirius Red, Alcian Blue and Hematoxylin-Eosin. Picrosirius red staining

was used to visualize collagen production, Alcian blue was used to stain glycosaminoglycans as well as proteoglycans, while haematoxylin-eosin staining was used to assess the general distribution of tissue and cell morphology and distribution [58]. For each of the aforementioned staining procedures, glass slides were removed from the oven and placed in a slide rack, one per each staining type. Using this rack, multiple slides could be easily immersed in the solutions included in each protocol. All three staining procedures can be divided in three parts: a first de-paraffinization and re-hydration part, a second staining part, and, finally, another dehydration part. The staining steps per type of stain are summarized in [Appendix F](#).

2.13.7 Imaging

Stained slices were imaged using an optical microscope (DM500, Leica Biosystems, Wetzlar, Germany) equipped with a 5-megapixel camera (ICC50W, Leica Biosystems, Wetzlar, Germany). Real-time imaging was performed using the Leica Application Suite (LAS software) for image acquisition. The following microscope settings were used for imaging: brightness: 70%, gamma: 0.8, saturation: 100%, sharpening: medium. Three objectives were used, namely a 4× (N.A.: 0.1), a 10× (N.A.: 0.25) and a 40× (N.A.: 0.65) objective. Microscopy images of the pellets are presented as obtained while images of the self-bent scaffolds were first imported in Adobe Illustrator CC 2019 and arranged in order to reconstruct the whole scaffolds (for the 4× objective) or a particular region of interest (for the 40× objective).

2.14 Statistical Analysis

Samples were assessed in triplicate for each condition and the acquired data are presented as mean value \pm one standard deviation. Two-way ANOVA followed by multiple comparisons test was performed for grouped data, using GraphPad Prism version 9.1.1. for Windows (GraphPad Software, San Diego, California USA). When only two data sets were compared, Welch's t-test was used. A p value < 0.05 was considered significant. * : $p < 0.05$, ** : $p < 0.01$, *** : $p < 0.001$, **** : $p < 0.0001$.

3 Results

3.1 Rheological Characterization of the HA-Tyr and Alg/HA-Tyr inks

In situ enzymatic crosslinking of the two inks, triggered by H_2O_2 addition and followed by immediate loading of the formulation on the rheometer plates, revealed the time progress of the crosslinking process (Fig. 8a). The storage moduli of both materials showed an almost linear, sharp increase before reaching a plateau value, which indicated the end of crosslinking. A similar, though less pronounced, due to magnitude difference, behavior was also measured for the loss moduli of the two inks. Moreover, from the same graph it is observed that G' and G'' for both materials reached their plateau values within approximately 20 min. The prevalence of the elastic over the viscous component was evident in both inks, as their G' plateau values were at least 8 times greater than the corresponding G'' values (Fig. 8b). More specifically, the storage modulus of HA-Tyr plateaued at ≈ 190 Pa while its loss modulus reached a value of ≈ 7.9 Pa. On the other hand, the storage and loss moduli of Alg/HA-Tyr plateaued at ≈ 200 Pa and ≈ 23 Pa, respectively. The higher damping factor calculated for the Alg/HA-Tyr ink revealed the presence of a higher viscous portion in this material ($\tan\delta_{Alg/HA-Tyr} = 0.116$ VS. $\tan\delta_{HA-Tyr} = 0.041$). Nevertheless, the damping factors of both inks were lower than 1, indicating that they are in the gel state (Table 2) [43].

It was observed that the two inks yielded at very similar strain values (approx. $10^5\%$) (Fig. 8c) and their calculated yield points were also found to be almost identical (Fig. 8d). The strain sweep tests further confirmed an elastic, gel-like behavior for both materials, as the elastic modulus, G' , was higher than the corresponding viscous modulus, G'' in the linear viscoelastic region, *i.e.*, the regime of the $G'(\gamma)$ and $G''(\gamma)$ curves, where the values of both the storage and loss moduli are independent of the applied deformation (Fig. 8e).

To investigate the frequency dependence of the inks, their response was measured during frequency sweep tests in the range of angular frequencies between 0.2π and 200π rad/s. The values of the storage modulus, G' , were consistently higher than the values of the loss modulus, G'' , in the frequency range studied, denoting the elastic behavior of the two inks was dominant when a load was applied (Fig. 8e). Thus, the tested inks demonstrated a gel-like behavior [59]. The storage moduli of both inks showed a very low frequency dependence, while, on the contrary, the loss moduli were frequency dependent, meaning that, when the inks are exposed to higher frequency values, the viscous component starts to influence their response.

Steady flow tests revealed that both inks have a shear rate, $\dot{\gamma}$, dependence, showing a shear thinning behavior (Fig. 8f). The material parameters, K and n , for the two inks

Table 2: Overview of the rheological parameters for the characterization of the HA-Tyr and Alg/HA-Tyr inks.

	Storage Modulus, G' (Pa)	Loss Modulus, G'' (Pa)	$\tan\delta$	Yield Stress (Pa)
HA-Tyr	190 ± 37.640	7.883 ± 0.873	0.041	595 ± 7.23
Alg/HA-Tyr	203 ± 13.140	23.570 ± 2.757	0.116	574 ± 21.9

shown in [Table 3](#), were determined by fitting the linear regime of the viscosity-shear rate curve using [Equation 1](#).

Table 3: Power-law fitting for Alg/HA-Tyr and HA-Tyr inks.

	$K (Pa.s^n)$	n	R^2
Alg/HA-Tyr	2467	0.2683	0.9995
HA-Tyr	2351	0.1541	0.9996

Following extrusion, the shear rate drops while the viscosity of the ink increases due to removal of the applied shear stress. As already mentioned, the materials should be capable of quick recovery of their solid-like behavior after extrusion. To determine the strain-dependent behavior of the inks with respect to their viscoelastic moduli, oscillatory thixotropy tests were performed ([Fig. 8g, h](#)). Similarly to the three-state printing process presented in [Fig. 2](#), the thixotropy test consisted of three steps: First, a low oscillatory strain is applied to the material, followed by a step of increasing strain, before returning to the original strain value (third step). During the low strain phase, the storage modulus G' prevails while in high strain phases, the loss modulus, G'' , dominates as the material starts to flow. The response of both inks to the final, low-strain step, is a relevantly fast structural recovery reaching almost 100% in the case of HA-Tyr, within 10 min ([Fig. 8g](#)). For the Alg/HA-Tyr ink, however, the storage modulus reached approx. 65% of its initial value in the 10 min following its exposure to high strain ([Fig. 8h](#)).

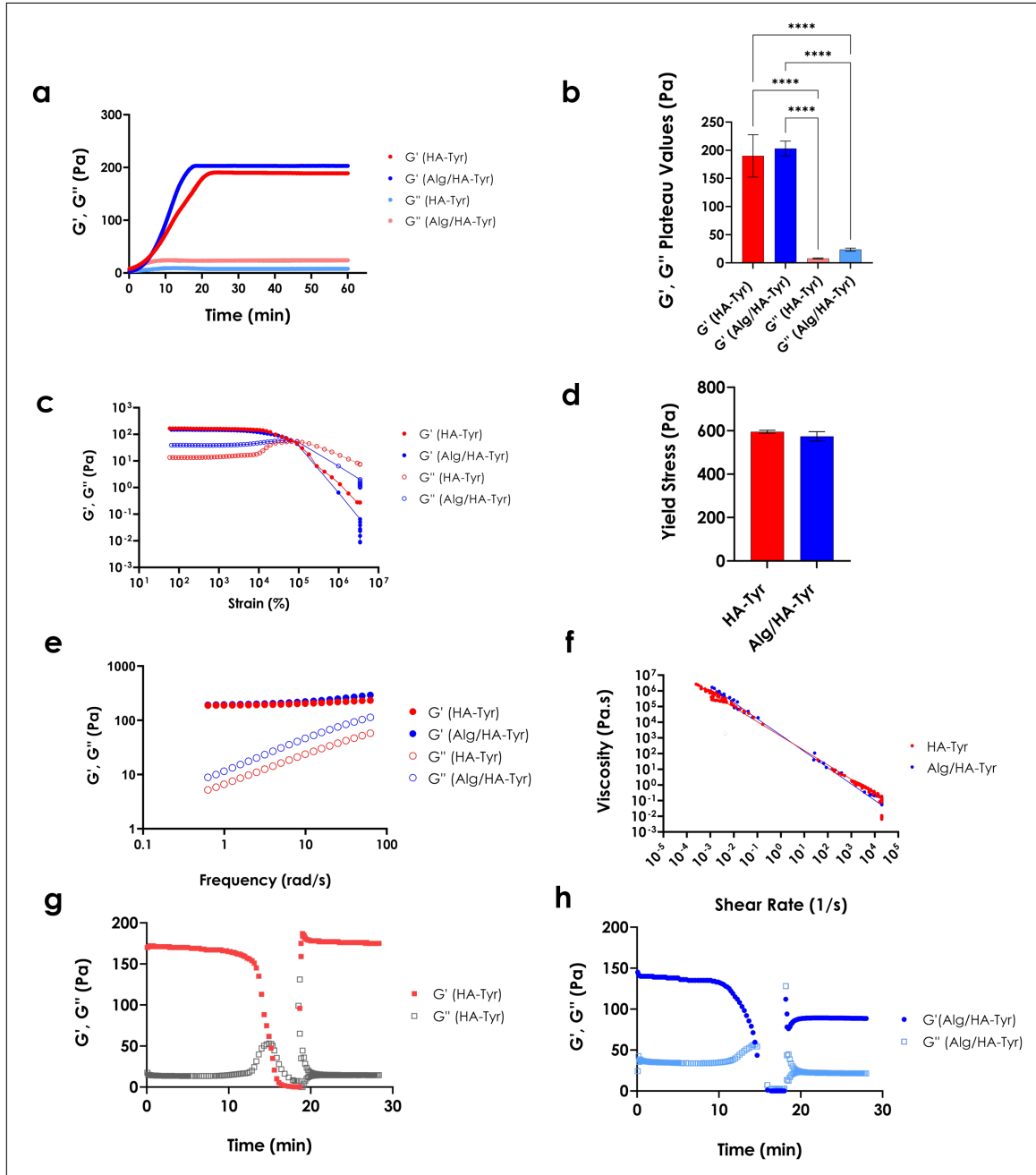


Figure 8: Rheological characterization of HA-Tyr and Alg/HA-Tyr inks. (a) Time dependence of the storage (G') and loss modulus (G'') of HA-Tyr (red) and Alg/HA-Tyr (blue). **(b)** The plateau values of G' and G'' for HA-Tyr (red) and Alg/HA-Tyr (blue). **(c)** Amplitude strain sweep for HA-Tyr (red) and Alg/HA-Tyr (blue) inks. Storage moduli, G' , are plotted as closed squares while loss moduli, G'' , are plotted as open squares. **(d)** Yield stress values of HA-Tyr (red) and Alg/HA-Tyr (blue). **(e)** Frequency dependence of the storage (G') (closed circles) and loss modulus (G'') (open circles) of HA-Tyr (red) and Alg/HA-Tyr (blue). **(f)** Shear rate, $\dot{\gamma}$, dependence of the shear viscosity, η of the HA-Tyr (red) and Alg/HA-Tyr (blue). Oscillatory thixotropy tests for HA-Tyr **(g)** and Alg/HA-Tyr **(h)**.

3.2 Single-Material 3D Printing: Printing Optimization, Scaffold Design and Characterization

Single-material scaffolds from Alg/HA-Tyr and HA-Tyr were printed, in order to measure their individual responses under compressive loading as well as their swelling behaviors. Compression tests revealed that the secondary crosslinking of the Alg/HA-Tyr ink with 200 mM CaCl₂ for 10 min resulted in a compressive modulus of ≈ 6.7 kPa which was more than 3 times larger than the modulus measured for HA-Tyr (≈ 2.1 kPa) (Fig. 9a). Moreover, Alg/HA-Tyr scaffolds showed a negligible change of their swelling ratios after 2 h and 24 h of immersion in 0.9% NaCl with 2 mM CaCl₂ ($SR_{2h} \approx 2.5$ VS. $SR_{24h} \approx 2.6$) (Fig. 9b). On the other hand, HA-Tyr scaffolds exhibited a pronounced increase in swelling after 24 h of immersion in the aforementioned solution. More specifically, a swelling ratio of ≈ 3.2 was measured for HA-Tyr scaffolds after 2 h of immersion, which increased to a value of ≈ 5.7 after 24 h. Therefore, HA-Tyr scaffolds absorbed at least two times more liquid than their Alg/HA-Tyr counterparts after 24 h.

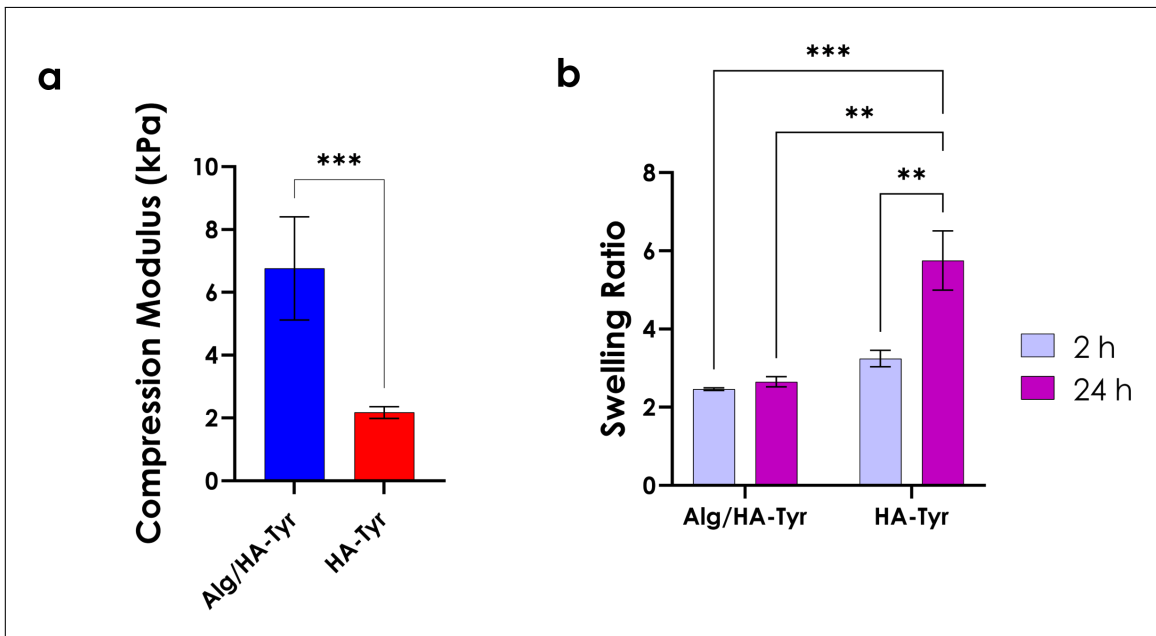


Figure 9: Single-material Scaffold Characterization (a) Compression moduli of Alg/HA-Tyr and HA-Tyr scaffolds. (b) Swelling ratios of Alg/HA-Tyr and HA-Tyr scaffolds after immersion in 0.9% NaCl with 2 mM CaCl₂.

3.3 Multimaterial 3D Printing: From 3D to 4D

If $SR_1 > SR_2$ then $\lambda_1 > \lambda_2$ and the bending of the bilayered hydrogel scaffold is expected to be convex down (see Fig. 6b). Therefore, it was decided to fabricate rectangular scaffolds consisting of a bottom layer of HA-Tyr and a top layer of Alg/HA-Tyr, as $SR_{v,HA-Tyr} > SR_{v,Alg/HA-Tyr}$, in order to observe bending “towards” the side of the top layer, *i.e.*, the Alg/HA-Tyr layer, upon immersion in 0.9% NaCl with 2 mM CaCl₂. The predicted bending direction was experimentally verified as presented in Fig. 10a. To demonstrate the possibilities of this 4D printing approach, more complex geometries, including cross-, star- and flower-shaped scaffolds, were fabricated, yielding sophisticated structures upon swelling

(Fig. 10(b-d)).

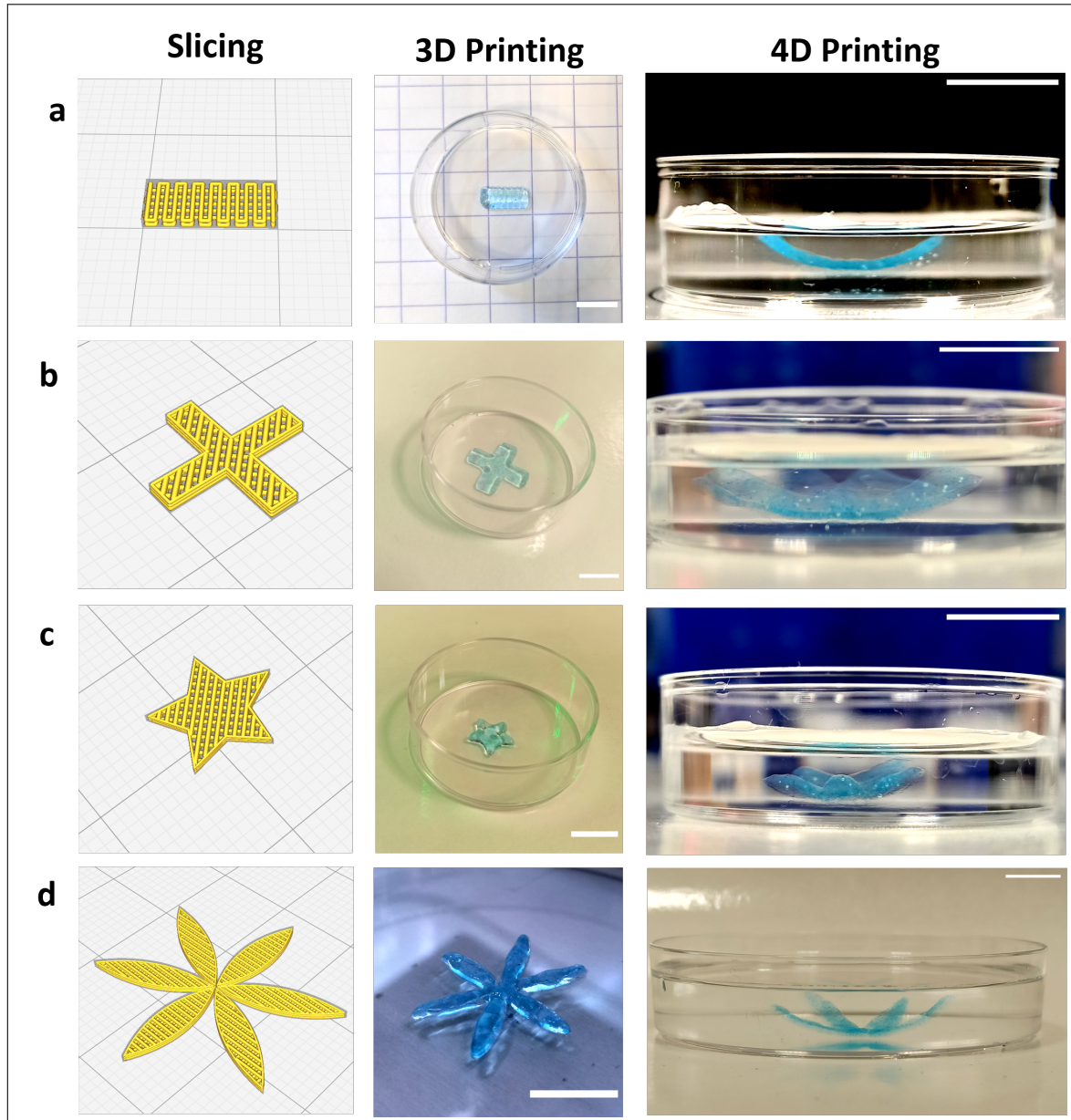


Figure 10: Different scaffold designs during the slicing (left), 3D printing (middle) and 4D printing (right) steps of the fabrication process. (a) Rectangular scaffold with a zig-zag infill pattern of $0^\circ - 90^\circ - 0^\circ$. (b) Cross-shaped, (c) star-shaped and (d) flower-shaped scaffolds with a line infill pattern ($45^\circ - 135^\circ$) and a single-wall shell. All designs (a–d) comprise of two bottom layers made from HA-Tyr and one top layer made of Alg/HA-Tyr. Slicing of scaffolds was performed using Cura. Shape-shifted scaffolds are imaged submerged in 0.9% NaCl with 2 mM CaCl_2 . Scale bars: 10 mm.

3.4 Parameters affecting self-bending

Following the achievement of self-bending of the bilayered scaffolds, the effect of different parameters on the final curvature of the structures was investigated. More precisely, the influence of the infill density values, printing angles combination as well as the thickness ratio of the two printed materials was investigated. Subsequently, the effect of a range of CaCl_2 immersion times and swelling solvent composition on the self-bending was studied. The parameters were divided into two categories: (i) fabrication- and (ii) post-processing related parameters. The first three parameters belong to category (i) while the last two to category (ii).

3.4.1 Effect of Infill Density and Printing Pattern on Curvature

The combinations of the infill densities and printing patterns produced scaffolds which exhibited self-bending upon immersion in 0.9% NaCl with 2 mM CaCl_2 (Fig. 11(a-l)). The curvatures of the bilayered scaffolds made with 2 bottom layers of HA-Tyr and 2 top layers of Alg/HA-Tyr after 2 and 24 h after of immersion in the NaCl solution are presented in the graph of Fig. 11m. The greatest curvature value, 0.125 mm^{-1} for a 24 h immersion, was observed for the scaffolds printed with 40% infill and a $0^\circ - 90^\circ$ printing pattern (Fig. 11a, d). For the same infill value, a change in the printing direction of each layer to $90^\circ - 0^\circ$ resulted in a significantly lower curvature of 0.074 mm^{-1} after 24 h (Fig. 11g, j). The lowest curvature value (0.029 mm^{-1}) was measured for scaffolds with 50% infill and $0^\circ - 90^\circ$ printing pattern (Fig. 11b, e). The $0^\circ - 90^\circ$ pattern led to an increase of the curvature to 0.042 mm^{-1} for the same infill value (Fig. 11h, k). For the 60% infill pattern, the curvatures measured after 24 h of immersion were significantly higher than those measured for the 50%, for both the $0^\circ - 90^\circ$ and $90^\circ - 0^\circ$ printing patterns (Fig. 11f, l). However, using the $0^\circ - 90^\circ$ pattern, the scaffolds exhibited similar curvature values for 2 and 24 h of immersion (0.055 mm^{-1} and 0.06 mm^{-1} , respectively) (Fig. 11c, f). On the contrary, the $90^\circ - 0^\circ$ printing pattern resulted in scaffolds that took a longer time to reach their final curvature (0.025 mm^{-1} for 2 h and 0.05 mm^{-1} for 24 h) (Fig. 11i, l).

Based on these results, three infill-printing pattern combinations prevailed: the 40% infill with a $0^\circ - 90^\circ$ printing pattern, the 40% infill with a $90^\circ - 0^\circ$ printing pattern and the 60% infill with a $0^\circ - 90^\circ$ printing pattern. Although the 40% infill led to a more pronounced self-bending, the scaffolds were less robust in comparison with their 60%-infill counterparts, which was the printing design selected to continue with the rest of the experiments.

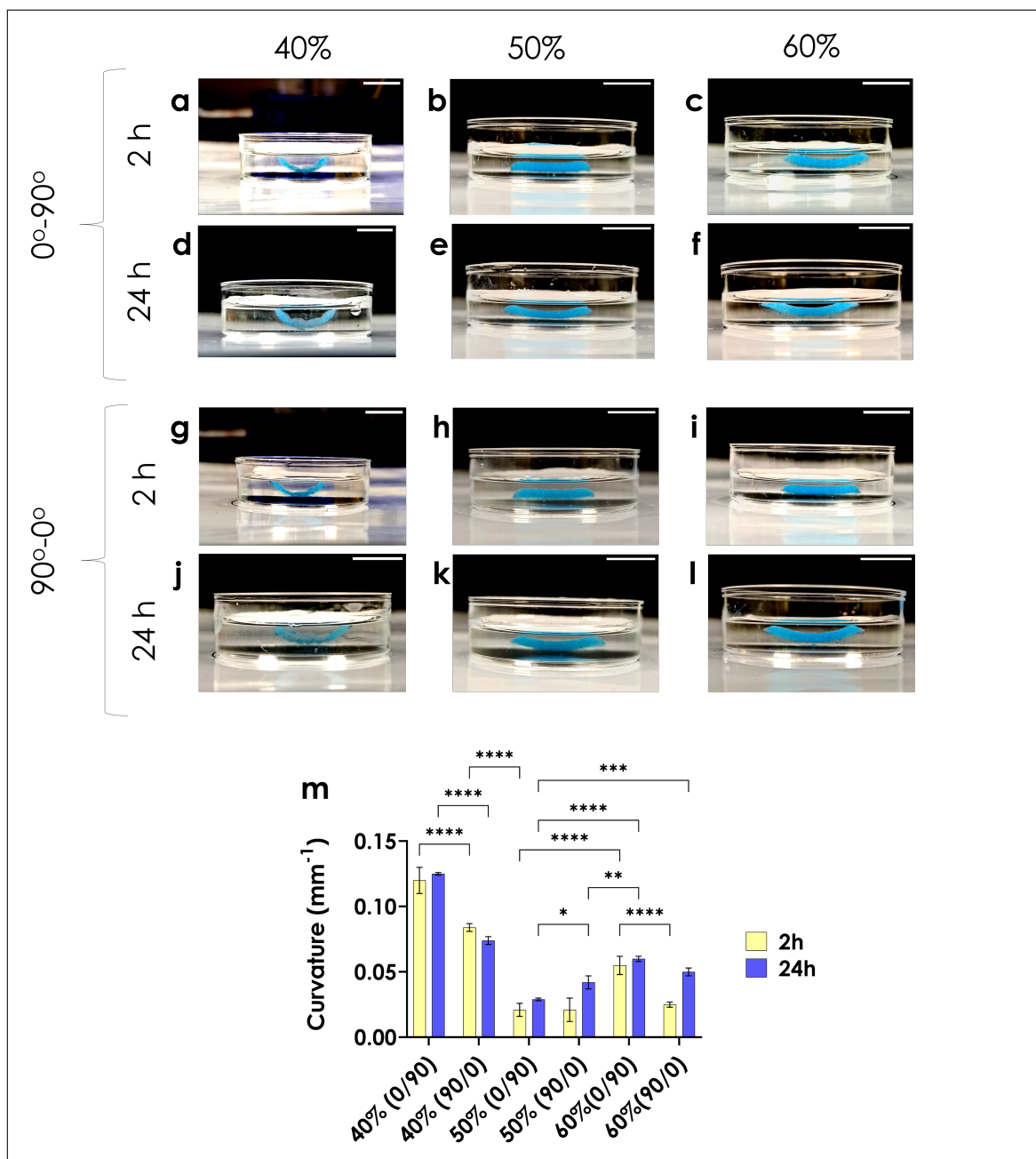


Figure 11: The effect of infill density and printing pattern on self-bending. (a-l) Side-view images of bilayered, self-bent scaffolds from HA-Tyr and Alg/HA-Tyr immersed in 0.9% NaCl with 2 mM CaCl₂. The pictures were obtained 2 h and 24 h after scaffold immersion in the swelling solvent. (m) Quantification of the curvatures measured per infill density and printing pattern combination for 2 h (yellow) and 24 h (cyan) of immersion. Scale bars: 10 mm.

3.4.2 Effect of Thickness Ratio on Curvature

From the results described in the previous section, the 60% infill and $0^\circ - 90^\circ$ printing pattern was the combination offering a satisfactory trade-off between scaffold robustness and self-bending. Nevertheless, the scaffold design was further optimized in an attempt to enhance the shape-shifting effect and obtain higher curvature values.

One of the factors affecting the curvature of the bilayered structure is the thickness ratio, m , and the total thickness of the scaffold, h (see Equation 6). By reducing the thickness of both the Alg/HA-Tyr and HA-Tyr from two to one printed layers, the same m value was obtained, which was equal to 1, however the h value changed to $h_{1:1} = \frac{h_{2:2}}{2}$, where $h_{1:1}$ the thickness of a scaffold with one printed layer of HA-Tyr followed by one printed layer of Alg/HA-Tyr and $h_{2:2}$ the thickness of a scaffold with two printed layers per material. If we assume the linear expansion rates, λ , of both inks remain constant, the new curvature, κ , is given by

$$\kappa_{1:1} \sim 2\kappa_{2:2} \quad (8)$$

where subscripts denote the number of printed Alg/HA-Tyr layers to printed HA-Tyr layers.

Starting from this estimation, the effect of three thickness ratios on the self-bending behavior of the hydrogel constructs was studied. More precisely, scaffolds with m values of 1:1, 1:2 and 1:3 were printed, corresponding to one top layer of Alg/HA-Tyr and one, two and three bottom layers of HA-Tyr, respectively (Fig. 12a-c). Images of the aforementioned scaffolds immersed in 0.9% NaCl with 2 mM CaCl_2 after 2 and 24 h are presented in Fig. 12d-f and Fig. 12g-i, respectively. A more pronounced bending was exhibited by all three conditions in comparison to the bending of the 2:2 scaffolds (Fig. 11d,f). Quantification of the corresponding curvature values confirmed the observed trend (Fig. 12j). The measured curvature of the 1:1 condition, 0.11 mm^{-1} , was almost two times greater than the curvature measured for the 2:2 condition (0.06 mm^{-1}) (see Fig. 11m), providing a good indication for the estimation of Equation 8. Moreover, the measured curvature values after a 2-h immersion in the swelling solvent for the 1:2 (0.068 mm^{-1}) and 1:3 conditions (0.07 mm^{-1}) were significantly lower than the corresponding value of the 1:1 condition (0.012 mm^{-1}). Nevertheless, after 24 h in 0.9% NaCl with 2 mM CaCl_2 , the curvature values measured for the 1:2 and 1:3 conditions showed a notable increase, reaching 0.13 mm^{-1} and 0.11 mm^{-1} , respectively, becoming similar to the 1:1 condition.

Thus, the objective of enhancing the curvature of the scaffold using the highest infill density value considered in the previous section, *i.e.*, 60%, was achieved. As the 24-h curvatures of scaffolds with thickness ratios of 1:1, 1:2 and 1:3 did not differ significantly, the choice of the optimal scaffold design among them depends on application-related factors. Although, the 1:1 scaffolds showed a fast self-bending that was evident from as early as 2 h post-immersion, they were very fragile and prone to tearing when manipulated with a spatula. On the other end of the spectrum, the HA-Tyr part of the 1:3 scaffolds swelled substantially, to the extent that during scaffold handling, it was easily separated from the Alg/HA-Tyr layer as it was “sticking” to the tools. Therefore, the 1:2 thickness ratio was selected as the optimal condition, because it yielded scaffolds capable of withstanding manipulation and retaining their integrity even when removed from the swelling solvent. Therefore, this scaffold design was adopted for the rest of the experiments.

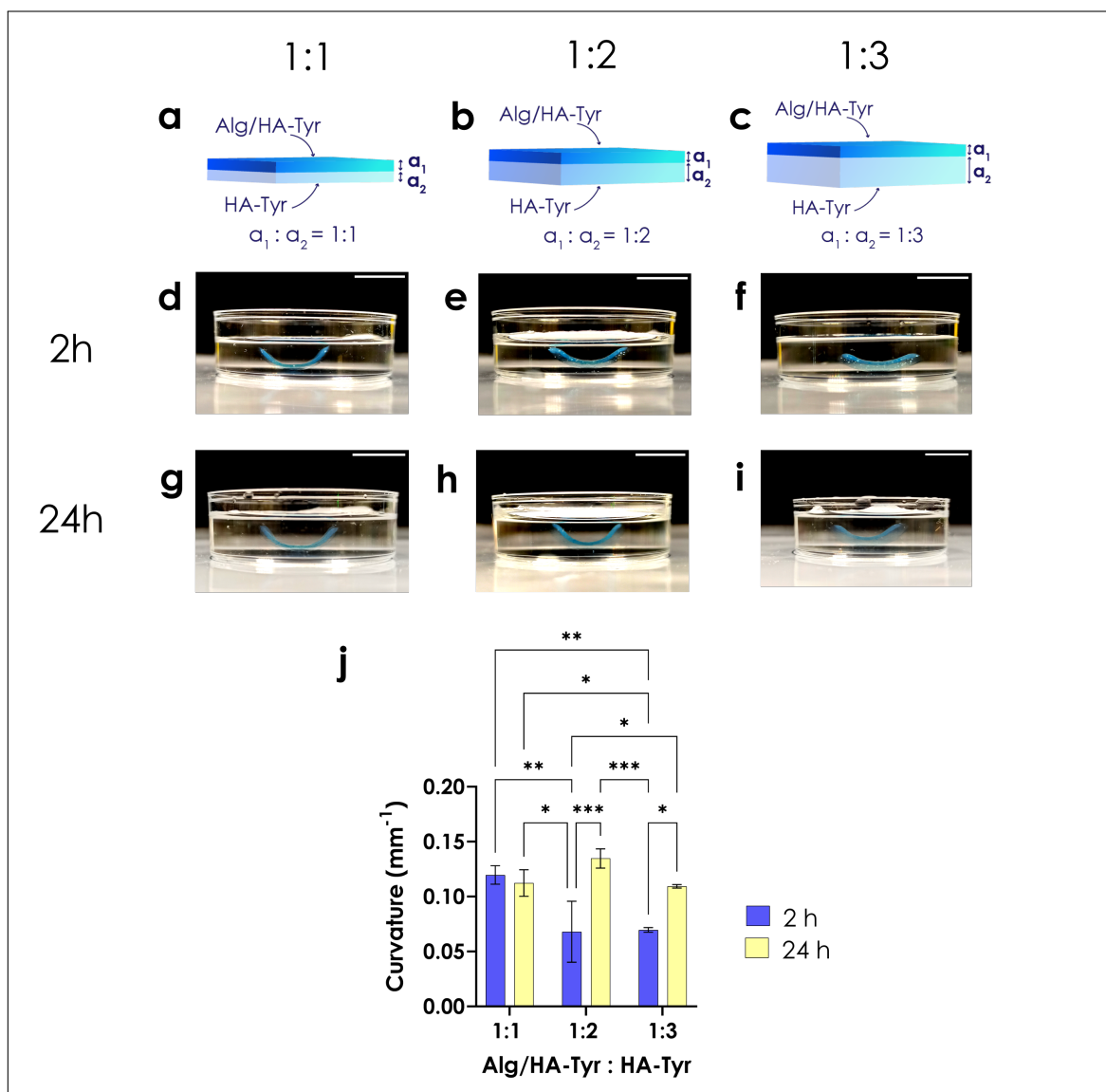


Figure 12: The effect of thickness ratio on self-bending. (a-c) Schematic illustration of the scaffold design for the 1:1 (a), 1:2 (b) and 1:3 (c) conditions. α_1 : the thickness of the Alg/HA-Tyr layer, α_2 : the thickness of the HA-Tyr layer. (d-f) Images of the scaffolds being submerged for 2 h in 0.9% NaCl with 2 mM CaCl_2 . (g-i) Images of the scaffolds being submerged for 24 h in 0.9% NaCl with 2 mM CaCl_2 . (j) Quantification of the curvature values measured for the 1:1, 1:2 and 1:3 conditions after 2 h (blue) and 24 h (yellow) in the aforementioned swelling solvent. Scale bars: 10 mm.

3.4.3 Effect of CaCl₂ Crosslinking Time on Curvature

From Equation 6 it was demonstrated that the swelling-induced bending of a bilayered structure is also affected by the elastic moduli, E , and the swelling ratios of the two materials. Therefore, the effect of varying the time of CaCl₂ immersion was investigated as another potential mechanism of controlling the degree of self-bending. Four different crosslinking times were studied, namely 10, 15, 20 and 25 min. Images of the scaffolds after crosslinking and immersion in swelling solvent (0.9% NaCl with 2 mM CaCl₂) are presented in Fig. 13a-h, for 2 and 24 h of swelling. The measured curvatures of the bilayered scaffolds, presented in Fig. 13i, revealed that the 3D printed structures exhibited a similar bending, regardless of the crosslinking or swelling time (0.13-0.16 mm⁻¹). For all four groups, a significant increase was demonstrated between the curvature after 2 and 24 h of swelling. The lack of a visible change in the obtained curvatures was further investigated by printing single-material scaffolds, and measuring their swelling ratios and compression moduli for different crosslinking times. More precisely, Alg/HA-Tyr scaffolds and HA-Tyr scaffolds were printed and immersed in 200 mM CaCl₂ for 10, 15, 20 and 25 min. Subsequently, their swelling behaviors were measured and the results are presented in Fig. 13j, k. Neither of the two inks showed a significant difference in their swelling ratios for any of the investigated conditions. More precisely, Alg/HA-Tyr scaffolds, showed an almost identical swelling behavior for all the four crosslinking times considered, and their ratios were about 2.5 (Fig. 13j). The HA-Tyr scaffolds demonstrated a swelling ratio of approx. 3.5 for 2 h of immersion after 10, 15 and 20 min of CaCl₂ immersion (Fig. 13k). The scaffolds for the 25 min condition had a higher average swelling rate (approx. 7), however there was no significant difference between the four groups. An increase in the measured swelling was reported after 24 h for the same scaffolds which was statistically similar among the four different conditions. Thus, λ_1 and λ_2 are expected to remain relatively constant, *i.e.*,

$$\left(\frac{\lambda_2}{\lambda_1}\right)_{10min} \approx \left(\frac{\lambda_2}{\lambda_1}\right)_{15min} \approx \left(\frac{\lambda_2}{\lambda_1}\right)_{20min} \approx \left(\frac{\lambda_2}{\lambda_1}\right)_{25min} \quad (9)$$

Moreover, compression tests revealed that the elastic modulus of Alg/HA-Tyr was not affected significantly by the increase of its crosslinking time and was between 7.1 to 9.1 kPa. Nevertheless, all four Alg/HA-Tyr groups maintained a significantly higher value from the HA-Tyr group (approx. 2 kPa) (Fig. 13l). From this result, the relationship between the elastic modulus and the linear expansion ratio, $E \approx \lambda^{-v}$, presented in Section 3.3., was verified, as they both showed a relatively constant behavior. Therefore, the exponent, v , is also constant resulting to a constant value of the coefficient α . Finally, based on the above explanation, from Equation 9 it was estimated that:

$$\kappa_{10min} \approx \kappa_{15min} \approx \kappa_{20min} \approx \kappa_{25min} \quad (10)$$

Hence, the similar self-bending behavior of the scaffolds was also in accordance with Equation 6.

The results presented above indicated that the time of scaffold immersion in 200 mM CaCl₂ solution resulted in similar self-bending when varied between 10 and 25 min. Thus, since the ultimate goal of the present thesis was the fabrication of self-bending cell-laden

scaffolds, the choice of crosslinking time was made based on the effect of CaCl_2 exposure on hMSC viability (see [Appendix A](#)).

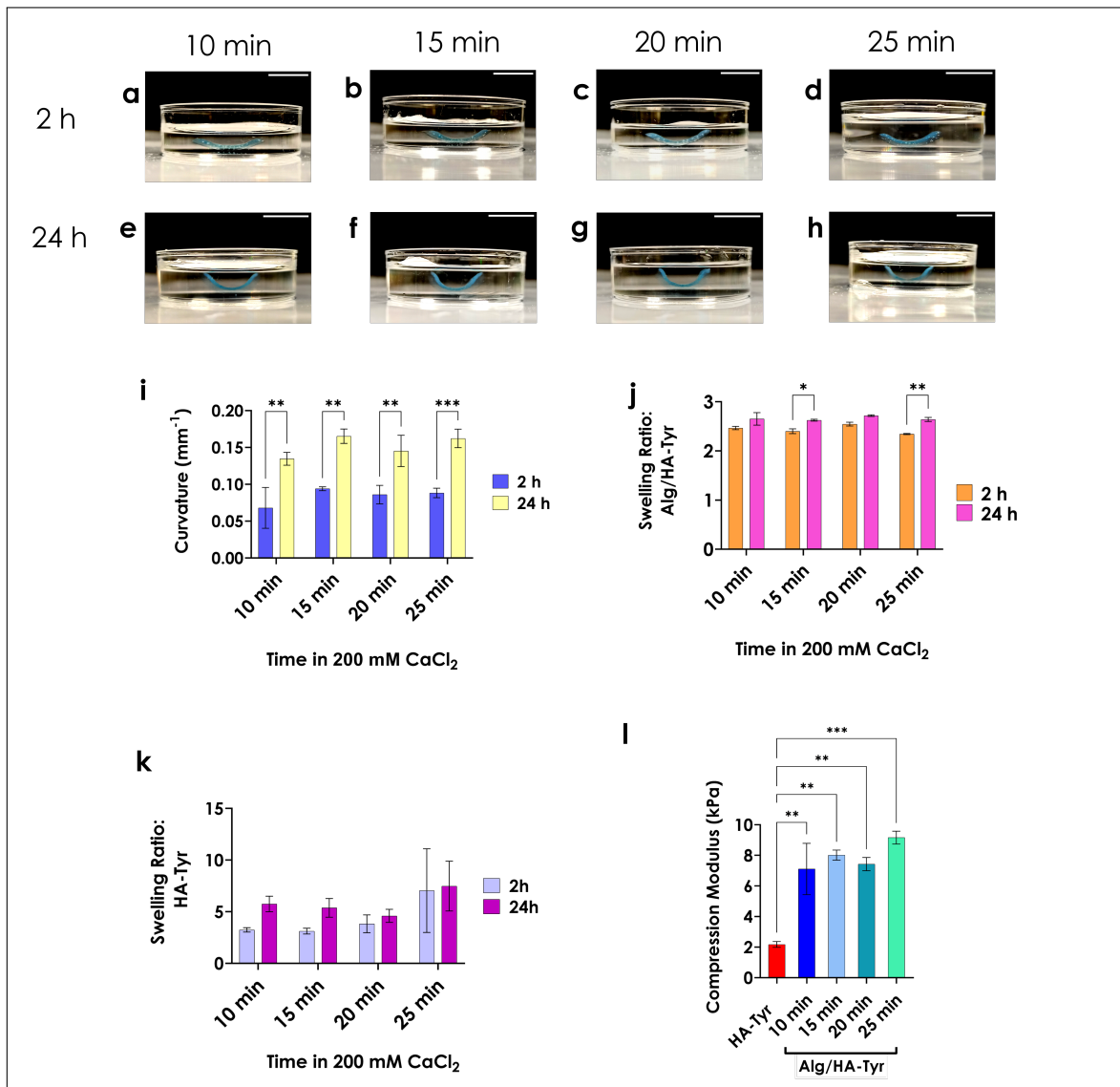


Figure 13: Effect of CaCl_2 immersion time in the curvature. (a-h) Images of bilayered scaffolds from HA-Tyr and Alg/HA-Tyr acquired 2 h (a-d) and 24 h (e-h) after immersion in 0.9% NaCl with 2 mM CaCl_2 . The depicted scaffolds were immersed in 200 mM CaCl_2 for 10 min (a, e), 15 min (b, f), 20 min (c, g) or 25 min (d, h), before being transferred to the swelling solution. (i) Quantification of the curvature values measured for 10, 15, 20 and 25 min of CaCl_2 immersion, after 2 h (blue) and 24 h (yellow) in the swelling solvent. (j, k) Swelling ratios measured for the four conditions described above, using single-material scaffolds printed with Alg/HA-Tyr (j) (orange: 2 h swelling, pink: 24 h swelling) and HA-Tyr (k) (lilac: 2 h swelling, purple: 24 h swelling). (l) Compression moduli of single-material scaffolds made of HA-Tyr (red), and Alg/HA-Tyr crosslinked for 10 min (blue), 15 min (light blue), 20 min (dark green) or 25 min (light green). Scale bars: 10 mm.

3.4.4 Effect of Solution Composition on Curvature

The effect of different swelling solvents on the bending behavior of the hydrogels was also studied, in order to gain a better overview on their response in solutions of various solute amounts and types. More precisely, the bending of bilayered hydrogel scaffolds was studied in 0.9% NaCl (Fig. 14a, d), 5% NaCl (Fig. 14b, e), 10% NaCl (Fig. 14c, f), DMEM (Fig. 14g, j), 0.9% NaCl & 2 mM CaCl₂ (Fig. 14h, k) and deionized (di) H₂O (Fig. 14i, l). The pictures were acquired after 2 h (Fig. 14 a, b, c, g, h, i) and 24 h of immersion in the solutions (Fig. 14 d, e, f, j, k, l). The swelling ratios of the two materials in the different solutions are presented in Fig. 14m, n for 2 and 24 h of swelling, respectively. The quantified curvature values for all the aforementioned conditions are presented in the graph of Fig. 14o. The highest curvature value (0.13 mm⁻¹) was reported for the 0.9% NaCl with 2 mM CaCl₂. Slightly lower values were measured for the DMEM- and di H₂O-immersed scaffolds (0.1 mm⁻¹ and 0.09 mm⁻¹, respectively). However, upon closer examination, it was discovered that in di H₂O the HA-Tyr layer had swelled to the point of dissolving in the water and the observed scaffold was basically only the top Alg/HA-Tyr layer of the construct. For this reason, no swelling ratios are included for this solvent and the bar representing the average curvature obtained from scaffolds immersed in di H₂O is presented with a black-line pattern (Fig. 14o). A significantly lower curvature value was observed for immersion in the 10% NaCl solution (0.065 mm⁻¹). Interestingly, immersion of the bilayered scaffolds in both the 0.9% and 5% NaCl solutions resulted in a concave-down bending, which is here denoted with a negative curvature value. When a 5% NaCl solution was used as a swelling solvent, the scaffolds exhibited an initial concave down self-bending (-0.025 mm⁻¹) which gradually shifted to a slightly concave up after 24 h (0.017 mm⁻¹). However, in the case of the 0.9% NaCl solution, the initial curvature direction which was measured at -0.037 mm⁻¹ at 2 h, was preserved and increased (data not shown), leading to the breaking of the scaffold.

Immersion in 0.9% NaCl resulted in pronounced swelling of both hydrogels with the Alg/HA-Tyr ink reaching the highest value (approx. 5) that was also significantly higher than the measured swelling ratio of HA-Tyr. From Equation 6, if $\lambda_1 < \lambda_2 \Rightarrow \lambda_{HA-Tyr} < \lambda_{Alg/HA-Tyr}$, a convex down bending is expected. This swelling behavior was confirmed for the 2 h immersion, however, it could not be confirmed for the 24 h time-point, as the bilayered scaffolds were ruptured. Similarly, in 5% NaCl, Alg/HA-Tyr exhibited a higher liquid absorption in comparison to the HA-Tyr ink, which resulted in the convex down bending presented in Fig. 14h. After 24 h of immersion, though, the measured swelling ratios did not show a significant difference and the scaffolds appeared slightly bent (Fig. 14k). For the highest NaCl concentration tested, *i.e.*, 10%, the swelling ratios of the two inks did not exhibit a distinct difference for neither the 2 h nor the 24 h time-point. Scaffolds immersed in the aforementioned solution showed an initial slight curvature that was preserved throughout the 24 h course of the experiment. Despite not measuring a significantly different swelling ratio for DMEM-immersed scaffolds after 2 h, a clear dominance of the HA-Tyr swelling occurred after 24 h of immersion. Finally, constructs swelling in the 0.9% NaCl with 2 mM CaCl₂ solution, demonstrated the highest curvature (Fig. 14c, f), as the HA-Tyr part of the bilayers showed an increased swelling, evident from as early as 2 h, which almost doubled after 24 h. On the other hand, the swelling behavior of the Alg/HA-Tyr part remained almost unchanged for the same time-points.

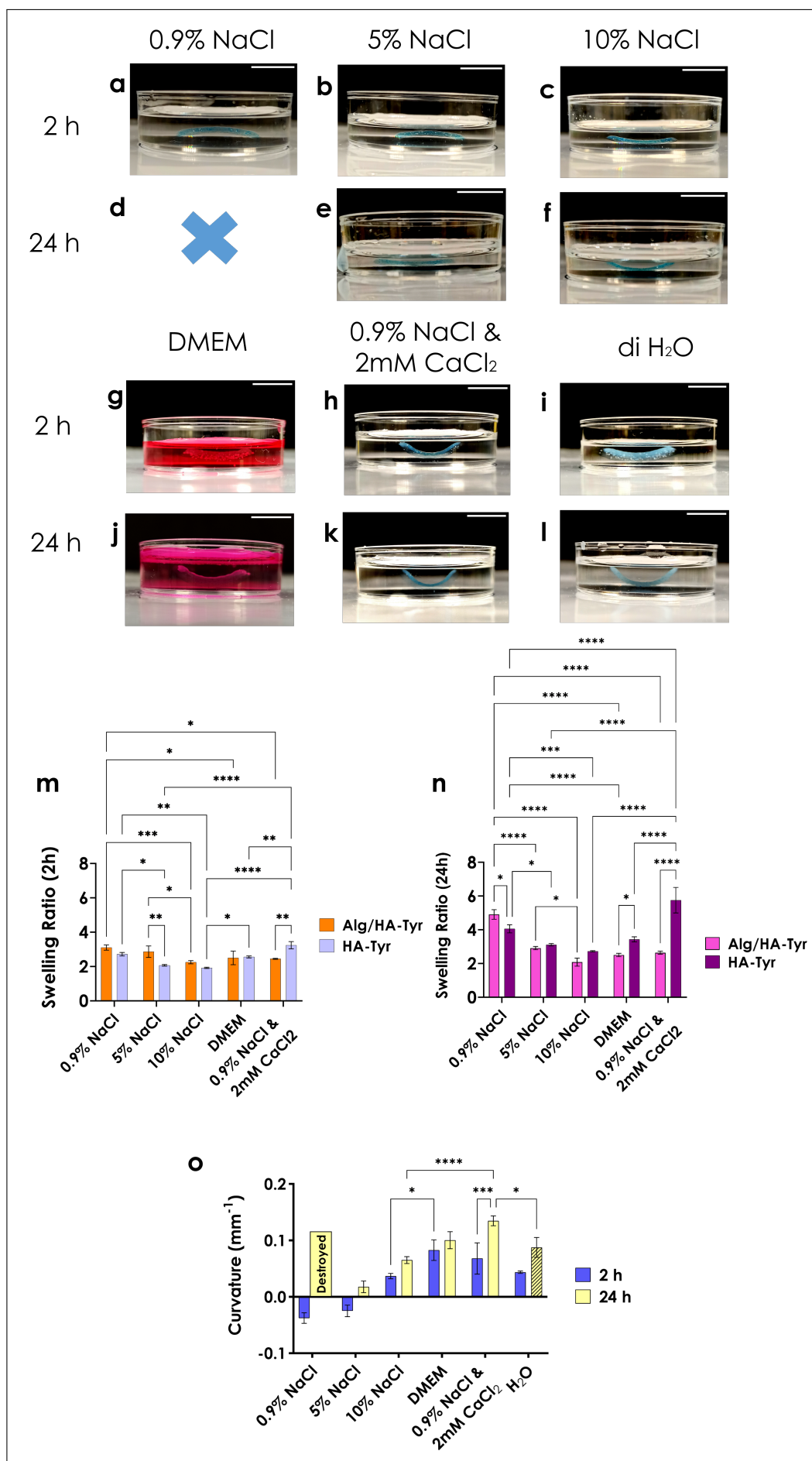


Figure 14: (continued) (a-k) Images of bilayered scaffolds from HA-Tyr and Alg/HA-Tyr acquired 2 h (a-c, g-i) and 24 h (d-f, j, k) after immersion in the following solutions: 0.9% NaCl (a, d) (the blue “x” represents the lack of image due to scaffold break), 5% NaCl (b, e), 10% NaCl (c, f), DMEM (g, j), 0.9% NaCl with 2 mM CaCl₂ (h, k) and deionized (di) H₂O i, l. Swelling ratios measured for single material scaffolds from Alg/HA-Tyr (orange) and HA-Tyr (lilac) after 2 (m) and 24 h (n) of immersion in the aforementioned solvents. (o) Quantification of the curvature values measured for each of the above solutions, after 2h (blue) and 24 h (yellow). Negative values correspond to a concave down bending. The black line pattern of the bar representing the curvature in di H₂O after 24 h corresponds to the absence of the bottom HA-Tyr layer. Scale bars: 10 mm.

3.5 4D Bioprinting

3.5.1 Determination of the Chondrogenic Capacity of hMSCs and Medium Optimization

Before the preparation of the bioinks, the chondrogenic capacity of the hMSCs was determined by performing a pellet study. In the same study, the influence of two different chondrogenic media on cartilage formation was also investigated, in order to determine the optimal medium for bioprinting. The two media used were a commercially available one (Lonza) (CM-L) and a medium based on a protocol suggested recently by Narcisi *et al.* (CM-E) [53]. Representative histological images are presented in Fig. 15a-i.

By comparing microscopy images of the Picrosirius red staining of the three groups it was observed that a significantly higher collagen production occurred in pellets cultured in the CM-E, as almost the whole surface of the pellet slice was stained red (Fig. 15d). On the contrary, pellets cultured in the CM-L for the same period of time had a lower collagen content (Fig. 15g) that was similar to that observed for day 2 (Fig. 15a). Alcian blue staining revealed a higher content of GAGs in the pellets cultured in CM-E (Fig. 15e) compared to those cultured in CM-L (Fig. 15h). Nevertheless, the CM-L-cultured pellets, though less stained, exhibited a distinctly different image from the controls (Fig. 15b), showing a higher GAG content. Finally, images from haematoxylin-eosin stained pellet slices showed a similar cell distribution in all three pellet groups (Fig. 15c, f, i). However, a more light pink hue can be observed for the CM-L-cultured pellets after 21 days (Fig. 15i) in comparison to those cultured in CM-E (Fig. 15f). From the above observations, it became apparent that the pellets cultured in CM-E produced more collagen and GAGs compared to those cultured in CM-L.

Metabolic activity measurements showed a distinct difference between the two media (Fig. 15j). More specifically, the corrected RFU values for pellets cultured in CM-L were approx. 15,000 and 14,000 for day 14 and day 21, respectively. On the other hand, pellets cultured in CM-E showed a notably higher metabolic activity for both culture days concerned ($\approx 59,000$ for day 14 and $\approx 48,000$ for day 21).

Thus, two conclusions were drawn from the study described above: First, the chondrogenic capacity of the hMSCs was confirmed, as both the CM-E and CM-L pellets showed collagen and GAGs production, denoting the formation of cartilage ECM. Second, induction

of chondrogenesis was more pronounced using the CM-E medium, making it the optimal option for the present project.

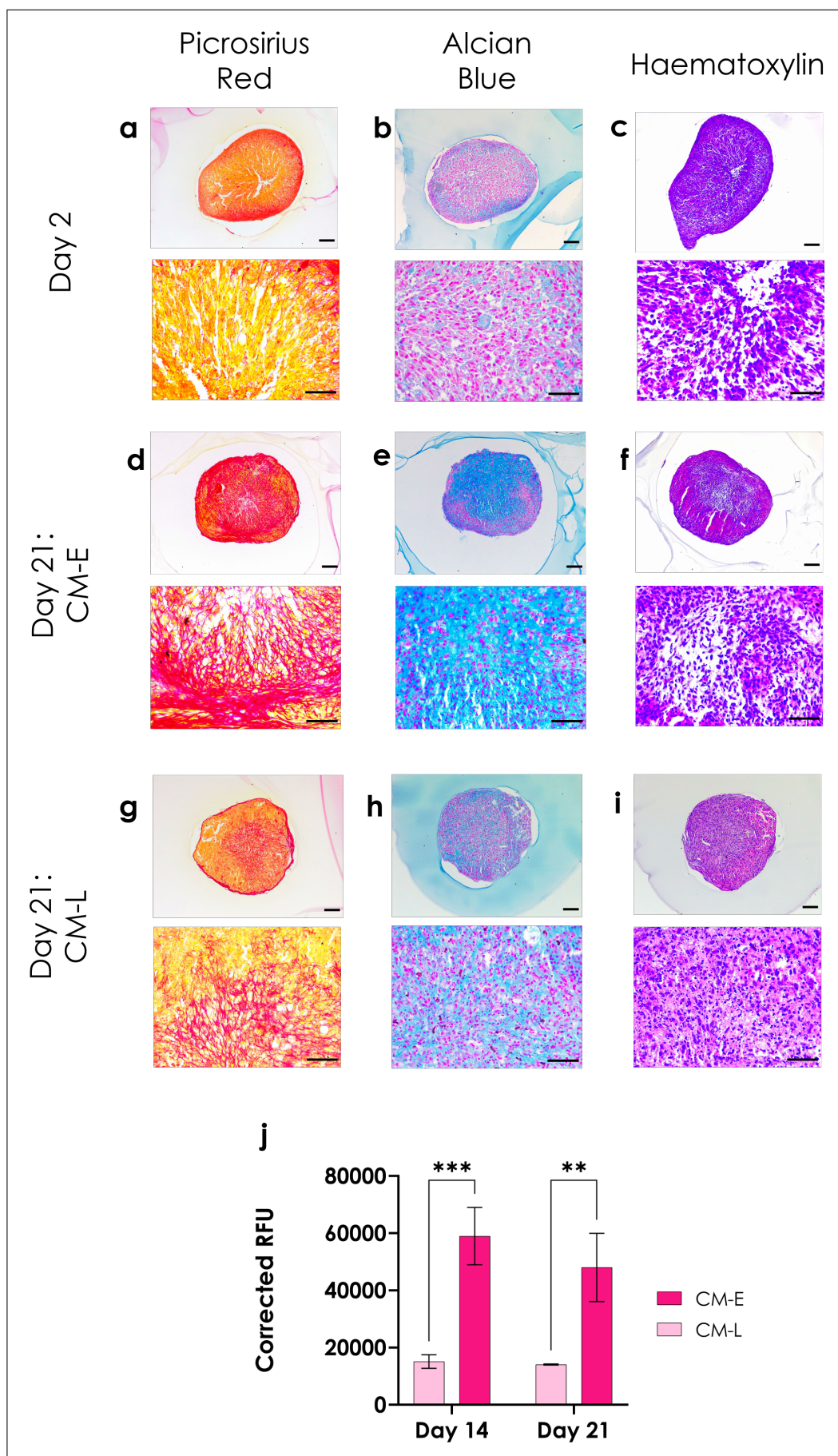


Figure 15: Pellet study for investigating the chondrogenic capacity of hMSCs and determining the optimal medium. (continued on next page)

Figure 15: (continued) **(a-i)** Representative microscopy images of slices from paraffin-embedded hMSC pellets stained with Picrosirius red (**a, d, g**), Alcian blue (**b, e, h**) and haematoxylin-eosin (**c, f, i**). The images show a control pellet (**a-c**), a pellet cultured for 21 days in CM-E (**d-f**) and a pellet cultured for 21 days in CM-L (**g-i**). Images depicting the whole pellet were acquired with a 10× objective (N.A.: 0.25) (**a-i, top**), while close-ups from the same pellets were acquired using a 40× objective (N.A.: 0.65) (**a-i, bottom**). **(j)** Quantification of metabolic activity using fluorescence readings of Presto blue assay for pellets cultured in CM-L (light pink) and CM-E (dark pink) for 14 and 21 days. Scale bars: 100 μm .

3.5.2 4D Bioprinting using Cell Expansion Medium

After confirming the chondrogenic differentiation capacity of the cells, hMSCs were incorporated in the Alg/HA-Tyr ink with a density of 5×10^6 cells/ml, and a first bioprinting study was performed. The aim of this first experiment was to investigate the viability and behavior of the cells in the self-bent scaffolds up to 14 days post-fabrication. For this reason, the bioprinted constructs were cultured in cell-expansion medium instead of chondrogenic differentiation medium. The HA-Tyr ink was not mixed with cells and was used solely for achieving self-bending of the scaffolds.

Fluorescent Live/Dead images of the scaffolds are presented in [Fig. 16a-c](#). Cells remained viable after 14 days of incubation and exhibited an increasing area. Live/Dead quantification revealed that cell viability varied between 69% to 76% for 1, 7 and 14 days of incubation ([Fig. 16d](#)). Furthermore, measurements of cellular shape factors showed a consistent increase in the measured cell area with increasing incubation days (from 397.2 μm^2 for Day 1 to 2931 μm^2 for Day 14) ([Fig. 16e](#)). On the other hand, the circularity of the cells remained almost constant, varying between 0.32 and 0.4, for the same time-points ([Fig. 16f](#)). Presto Blue TM reduction measurements showed a significant increase in fluorescence at day 14 (6320 RFU) compared to the RFU values measured for day 1 (1094 RFU) and day 7 (2467 RFU) (six- and three-fold increase, respectively). However, no significant difference was observed between the RFU values of day 1 and day 7.

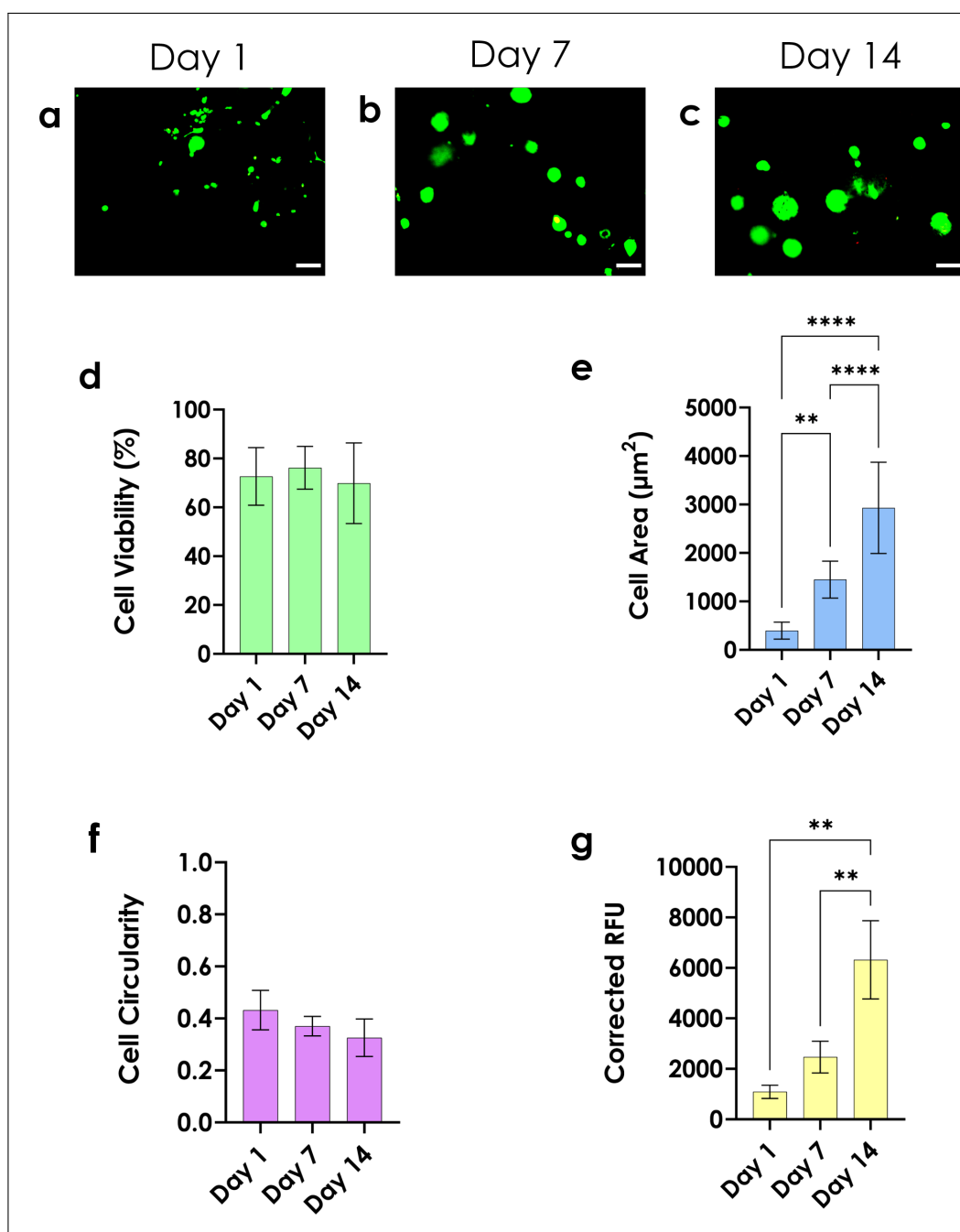


Figure 16: 4D Bioprinting: Viability and proliferation assessment of hMSCs in bilayered scaffolds from Alg/HA-Tyr and HA-Tyr incubated in expansion medium. (a-c) Merged fluorescent images from Live/Dead assay of the Alg/HA-Tyr layer of the bilayered scaffolds. Green color indicates the presence of viable cells stained with calcein while red color indicates the nuclei of dead cells stained with EthD-1. Images were acquired after 1 (a), 7 (b) and 14 (c) days of incubation with cell expansion medium. (d-f) Quantification of cell viability (d), cell area (e) and cell circularity (f) after 1, 7 and 14 days of incubation. (g) Quantification of hMSCs metabolic activity using fluorescent readings of Presto blue for 1, 7 and 14 days of incubation. Scale bars: 100 μm .

3.5.3 4D Bioprinting using Chondrogenic Medium

The response of hMSCs in 4D bioprinted scaffolds incubated in CM-E, was investigated. Two scaffold types were fabricated: bilayered scaffolds similar to the ones used for the previous experiments, made from a cell-free bottom part from HA-Tyr and a cell-laden top part from Alg/HA-Tyr and single-layered scaffolds from cell-laden Alg/HA-Tyr that were used as controls. In addition, the cell density was increased from 5 to 6.5×10^6 cells/ml.

Live/Dead assay images after 1, 7 and 14 days for both scaffold types are presented in Fig. 17 a-f. After 14 days of incubation in CM-E, hMSCs maintained a relatively stable average viability (from 65.1% to 80.2%) in the bilayered scaffolds (Fig. 17g). For the single-layered structures, though, a notably high number of dead cells was observed on day 1 (Fig. 17d). However, the controls' viability showed a significant increase for day 7 (69.6%) and day 14 (57.9%). Cell area measurements revealed that hMSCs in both scaffold types had comparable areas for day 1 ($562.5 \mu\text{m}^2$) and day 7 ($647.1 \mu\text{m}^2$), however, an increase was observed after 14 days ($966 \mu\text{m}^2$) (Fig. 17h). Similar area values were also measured for the controls for each time-point. On the other hand, there was a consistent difference in the circularity values between the two groups for all three time-points, with hMSCs in the single-layered scaffolds exhibiting a more circular morphology while the cells in the bilayered scaffolds showed a significantly decreased circularity value, meaning that they were generally more elongated for all the time-points concerned (Fig. 17i). Furthermore, the circularity values for the bilayered values decreased from 0.43 for day 1 to 0.33 for day 7 and remained almost constant till day 14 (0.35). A similar trend was also observed for the circularity values of the controls. More specifically, starting from 0.74 for day 1, they decreased to 0.51 for day 7 and maintained a similar value (0.52) for day 14.

Presto blueTM readings for the same time-points revealed that both scaffold types showed a similar pattern in their measured RFU values: an increased value for day 7 followed by a significant decrease for day 14 to a value similar to that measured for day 1 (Fig. 17j). The metabolic activity in the bilayered scaffolds increased significantly from 82,611 RFU for day 1 to 103,619 RFU for day 17 and dropped back to 81,994 RFU for day 14. Additionally, the very low viability for the control group measured for day 1 matched the metabolic activity readings, as an equally low value (17,292 RFU). Subsequently, the metabolic activity of the control group showed a pronounced increase of the hMSCs metabolic activity (68,068 RFU) and dropped again to 35,520 RFU on day 14. Overall, hMSCs in the bilayered scaffolds remained consistently more metabolically active than their control counterparts.

Histological staining revealed that there was an increase in GAGs production in the self-bent scaffolds between 14 (Fig. 18b) and 28 days of culture (Fig. 18h). An increase in collagen production was also observed (Fig. 18c, f, i), although it was less pronounced. A higher GAG and collagen production as well as a more intense HE staining (Fig. 18g) was detected at the outer parts of the scaffolds compared to regions located deeper in the structure for day 28 (Fig. 18g-i). Moreover, a higher contraction of the scaffolds was observed for day 28, which is evident by the reduced thickness of the structures (Fig. 18g-i).

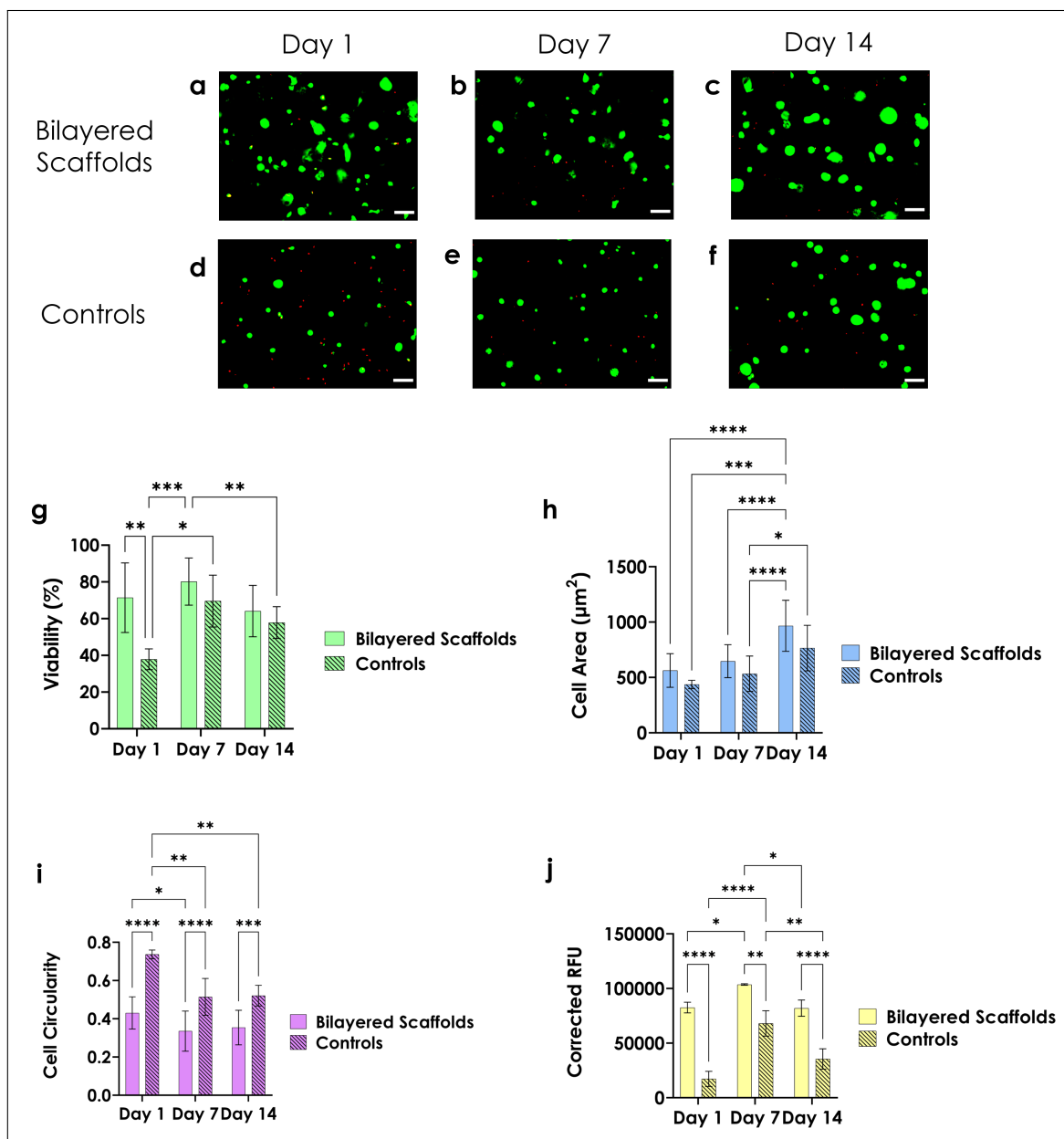


Figure 17: 4D Bioprinting: Viability and proliferation assessment of hMSCs in bilayered scaffolds from Alg/HA-Tyr and HA-Tyr incubated in chondrogenic medium. (a-c) Merged fluorescent images of Live/Dead assay of the hMSCs-laden Alg/HA-Tyr layer part of bilayered scaffolds from HA-Tyr and Alg/HA-Tyr. **(d-f)** Merged fluorescent images of hMSCs-laden Alg/HA-Tyr scaffolds. Live/Dead images were acquired after 1 **(a, d)**, 7 **(b, e)** and 14 days **(c, f)** of incubation in CM-E medium. Quantification of cell viability **(g)**, cell area **(h)** and cell circularity **(i)** for the bilayered (plain-colored bars) and the single-material scaffolds (patterned bars), after 1, 7 and 14 days of incubation. **(j)** Fluorescence readings of the cell-viability Presto blue assay after 1, 7 and 14 days. RFU: relevant fluorescent unit. Scale bars: 100 μm .

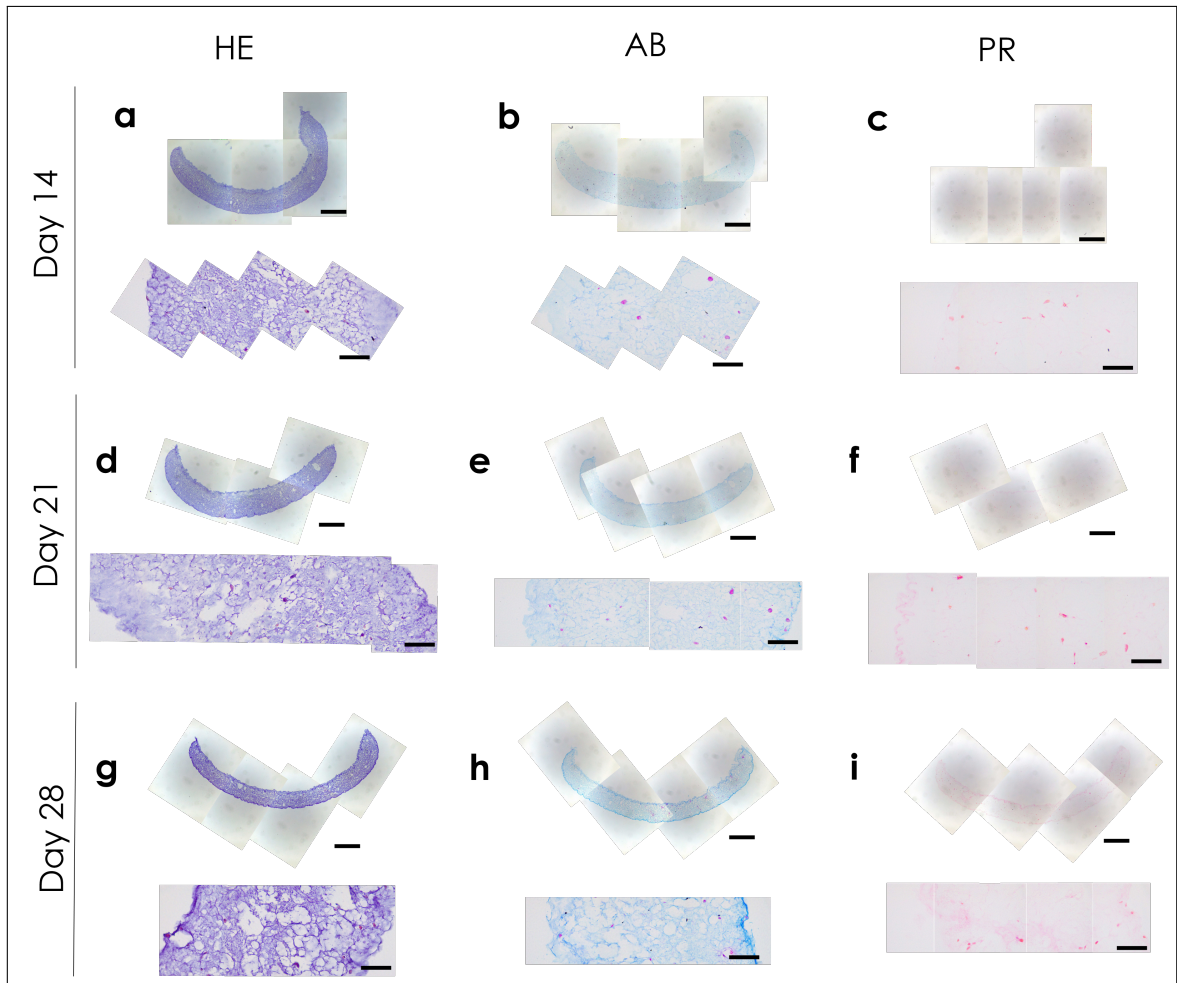


Figure 18: Histology of 4D bioprinted bilayered scaffolds. Representative images after 14 (a-c), 21 (d-f) and 28 days (g-i). The three stains imaged are Heamatoxylin-Eosin (HE) (a, d, g), Alcian Blue (AB) (b, e, h) and Picrosirius Red (PR) (c, f, i). Scale bars: 1 mm (top images), 100 μm (bottom images).

4 Discussion

Rheological measurements of the two inks confirmed their compatibility with extrusion printing. The crosslinking of both inks was complete after approx. 20 min which is in line with the 30-min incubation time after the addition of H_2O_2 suggested by Schwab *et al.* [42]. Addition of alginate in the HA-Tyr ink resulted in a composite hydrogel with a more pronounced viscous component and a decreased ability to recover after exposure to high strain values. Similar observations have been made when alginate was mixed with gelatin [60]. Increasing the alginate component of the composites led to an increase in loss modulus and damping factor. In addition, both inks exhibited a shear thinning behavior, as their viscosity decreased with increased shear rate, verifying their compatibility for extrusion printing. HA-Tyr inks with the same H_2O_2 and HRP concentrations have been reported to show good printability during extrusion [17]. The inks used for these measurements were cell-free and, thus, the influence of cell encapsulation on the viscoelastic properties and the printability of the hydrogels was not considered. However, cell embedding has been reported to affect the rheological properties of hydrogel-based bioinks, for cell densities varying from 2.5×10^6 cells/ml [19] to 500×10^6 cells/ml [61]. Especially for HA-Tyr, a dramatic impact of cell encapsulation on the rheological properties has been reported for a cell density of 5×10^6 hMSCs/ml [20]. For this reason, it was decided to mix the cell suspension with the Alg/HA-Tyr precursor formulation, after the enzymatic crosslinking was complete. Although a slightly increased flow for the same pressure values was observed for the Alg/HA-Tyr bioink, compared to the cell-free Alg/HA-Tyr formulation, the effect of this change did not significantly affect the printing process. Nevertheless, rheological characterization of cell-laden inks could provide valuable information about the bioprinting process and could, thus, be considered for future research. Furthermore, rheological measurements were performed for a constant temperature of 21°C , to imitate the conditions of printing at room temperature. When cell encapsulation is considered, though, the temperature of the bioink is increased and its properties could be potentially altered. In fact, it has been reported that increasing the bioink temperature from room temperature to 37°C results in a decrease of its viscoelastic moduli as well as its viscosity [62, 63]. Therefore, the response of the hydrogels for different temperatures could also be measured using a temperature sweep test.

Swelling measurements of the two inks revealed that HA-Tyr swells at least two times more than the Alg/HA-Tyr composite. The absorption of less liquid by the composite hydrogel was probably due to its higher crosslinking degree, given that both the HA-Tyr and the alginate components were crosslinked. Similar behaviors have been reported in the literature: Shah and Barnett observed a significant increase in the swelling ratios of HA hydrogels for a decreasing concentration of divinyl sulfone (crosslinking agent), [64], while Petta *et al.* reported a liquid absorption rate that was decreasing with increasing photocrosslinking time in HA-Tyr scaffolds [17]. The double crosslinking of the Alg/HA-Tyr composite was also responsible for its higher compression modulus compared to the value measured for the HA-Tyr scaffolds. A decreased crosslinking degree has been associated with a decreased mechanical strength in HA hydrogels [64] as well as alginate [65]. For the preparation of both inks, 0.9% NaCl was used and the swelling ratio and curvature experiments were conducted using 0.9% NaCl with 2 mM CaCl_2 solution. It has, however, been reported that storage of sodium alginate hydrogels in solutions with the same NaCl concentration (0.15 M) and a CaCl_2 concentration of 1.8 mM results in a significant decrease in both its compressive and shear moduli after 15 h [65]. Therefore, the properties of the Alg/HA-Tyr during the swelling experiments as well as during the bioprinting studies might

alter from those measured immediately after CaCl_2 crosslinking.

A starting infill of 40% was selected as lower values were expected to produce fragile scaffolds that would be difficult to manipulate post-printing. On the other hand, the infill was increased up to 60% as for this value adjacent printed filaments were observed to be slightly in contact with each other, without affecting the shape of the scaffold. The influence of the infill density and printing angle revealed that a lower infill density results in a more pronounced bending. The mechanism behind this behavior was not fully deciphered however, a possible explanation could be the increased distance between the filaments of the each printed layer. By increasing the inter-filamentous distance, *i.e.*, decreasing the infill density, the top and bottom surfaces of the scaffold obtain a patterned profile, which could enhance the ability of the structure to bend, acting like a “backbone”. Furthermore, an increased distance between adjacent filaments results also in an increased surface area in direct contact with the swelling solvent, which might explain why scaffolds printed with the 40% infill density showed a higher curvature from as early as 2 h of immersion. In fact, surface patterning has been reported to enhance self-folding of bioprinted scaffolds from silk fibroin [38], suggesting that a similar “striated” pattern could be responsible for the high curvature of the 40% infill group.

The layer ratio of the two hydrogels did not seem to affect significantly the obtained curvature, which is not fully aligned with the behavior that was expected based on the model. This behavior might be explained by the anisotropic swelling of the hydrogels. One of the basic assumptions made when this model was introduced was that both materials exhibited an isotropic swelling. However, given the position of each material in the printed structure, the swelling behavior of different printed layers might not be identical with the behavior of adjacent layers. For instance, the first printed layer, located at the bottom of the structure, has a higher surface area in direct contact with the swelling solvent and, thus, might expand easier towards that direction, whereas a layer located in the middle of the scaffold might exhibit a more pronounced swelling towards its sides. Therefore, since the model presented was a simple, qualitative approach, further investigation is needed to establish computational models capable of predicting the behavior of similar structures.

Increasing the crosslinking time of the Alg/HA-Tyr layer from 10 to 15, 20 and 25 min of immersion in 200 mM CaCl_2 did not influence significantly the observed bending. It has been reported that crosslinking time had an effect on the diameter of self-folding tubes made from methacrylated alginate and HA, which demonstrated a more pronounced folding with increasing CaCl_2 exposure time [41]. Moreover, in another study, the swelling degree of methacrylated HA was observed to be affected by the presence of Ca^{2+} cations [48]. This behavior was not observed, however, for the Alg/HA-Tyr and HA-Tyr bilayers. A possible explanation could be the different crosslinking mechanism, as methacrylated hydrogels were crosslinked using UV light. Furthermore, in both the aforementioned studies, the highest CaCl_2 concentration considered was 100 mM. Thus, it could be possible that both alginate- and HA-based hydrogels demonstrate a shape-shifting dependence on Ca^{2+} cations up to a certain concentration above which, no further change is observed. In fact, Shah and Barnett reported an asymptotic decrease of the swelling ratio of HA hydrogels with increasing CaCl_2 concentration, which, however, became less pronounced for higher concentrations (60 mM to 100 mM) which could explain the behavior of the HA-Tyr scaffolds [64]. In order to test this assumption, more experiments are needed that would investigate the effect of a range of CaCl_2 concentrations as well as crosslinking-times on the two inks.

Different solutions were found to have an effect on the swelling behavior of the two inks and, consequently, on the curvature of the self-bent scaffolds. The decrease of the HA-Tyr swelling ratio with increasing NaCl concentration is a behavior that has been reported in the literature for HA hydrogels [64]. However, the significantly higher swelling of HA-Tyr in 0.9% NaCl with 2 mM CaCl₂ is a behavior that could not be explained and needs further investigation. On the other hand, Ca²⁺-crosslinked alginate has been reported to swell in the presence of Na⁺ ions due to a Na⁺-Ca²⁺ ionic exchange. Briefly, the Ca²⁺ ions undergo an ionic exchange process with the Na⁺ ions, “leaching” out of the hydrogel and, consequently, increasing its swelling capacity [66]. An increased liquid uptake was observed for the Alg/HA-Tyr inks in 0.9% NaCl, which, however, decreased with increased concentration of NaCl. The interplay of the two polymers in the hydrogel needs to be further investigated, however, a first speculation is that at 0.9% NaCl, the alginate swelling seems to define the behavior of the structure. As the NaCl concentration increases, though, a decreased water uptake is observed, and the HA-Tyr component of the structure seems to prevail. The decreased swelling ratio of the Alg/HA-Tyr inks in DMEM and 0.9% NaCl with 2 mM CaCl₂ is relevant with results reported in literature and is possibly associated with the presence of Ca²⁺ ions in the solutions which slightly crosslink the alginate component. More precisely, it has been found that 1% alginate hydrogels contracted when immersed in 3 mM CaCl₂ solutions, and a decreased concentration of Ca²⁺ ions was measured after hydrogel immersion [67].

In both bioprinting studies presented in this thesis, an initial drop in cell viability was observed. More precisely, cell viability measured for day 1 was approximately 75% for both conditions. The source of this initial viability drop could be due to the printing process per se and/or the post-printing processing of the scaffolds. More precisely, extrusion bioprinting has been reported to have a significant effect on the viability of the encapsulated cells which in some cases reached a value as low as 50% [68,69]. However, during printing optimization, the optimal pressure values were determined as the minimum values for which filament extrusion occurred. This is an approach compatible with the concept of the “biofabrication window” which describes the trade-off between bioink printability and cell viability [70,71]. High viability values (90%-100%) have been reported in extrusion bioprinting of cell-laden gelatin, using significantly higher pressures (1-2 bar) as well as for nozzles with smaller inner diameters (200 μ m) [19]. Therefore, the extrusion of the bioink was probably not the main factor responsible for the viability decrease. On the other hand, it was observed that exposure of hMSCs to 200 mM CaCl₂ for 10 min negatively influenced their viability. Hence, it is likely that cell death was caused by the immersion of the scaffolds in 200 mM CaCl₂ during the Alg/HA-Tyr crosslinking step. In order to address this issue, the use of 100 mM CaCl₂ for the Alg/HA-Tyr crosslinking could be considered.

During bioprinting, only the Alg/HA-Tyr ink was mixed with cells, while the HA-Tyr part of the scaffold was cell-free and used for the shape-shifting. This decision was made based on the lack of a secondary crosslinking step for this ink which resulted in a significantly lower compression modulus compared to the modulus measured for the Alg/HA-Tyr. Furthermore, during scaffold manipulation, such as transferring of scaffolds to a different well-plate or refreshing, the softer HA-Tyr part was the one in contact with either the spatulas or bottom of the well, respectively. Therefore, the risk of material and, consequently, cell loss during the culturing period was considered high. Based on these facts, cells were only incorporated on the Alg/HA-Tyr layer.

Culturing bioprinted bilayers, laden with hMSCs, in expansion medium exhibited cer-

tain challenges in terms of cell viability quantification. As already mentioned, the apparent cell area showed a significant increase after 14 days of incubation. Assuming that each of the observed green particles is a cell, the average area values measured for day 14 correspond to a cell diameter of approx. $55 \mu\text{m}$, which is surprisingly large in comparison to hMSCs dimensions reported in the literature [56]. A possible explanation for the large area measurements could be that hMSCs did indeed expand but, being encapsulated in the Alg/HA-Tyr hydrogel, they formed clusters of cells. Therefore, the observed large particles probably contained more than one cells that could not be distinguished using fluorescent microscopy, leading to a possible underestimation of the measured viability. This assumption is also supported by the lack of cell adhesion ligands in alginate [72] and the low cell adhesion reported for HA-Tyr gels [17, 73].

4D bioprinted scaffolds exhibited differences when compared to the 3D bioprinted (single-material) controls, with the most evident difference being in the measured cell circularity for all three time-points. The hMSCs in the self-bent scaffolds exhibited a more elongated shape even after 1 day of incubation. A possible explanation for this observation could be the fact that during imaging the Live/Dead solution was discarded and scaffolds were left resting on the bottom of the well plates. The bent scaffolds, however, could not hold their shape outside the medium and became flat after the solution was removed. Therefore, if the cells had managed to attach to the material within the first 24 h from the bioprinting, their elongation could be due to the scaffold's deformation from a bent to a flat shape. This assumption needs further investigation and could be answered by attempting to image the cells while the scaffolds are immersed in a solution.

Collagen production was low at all three time-points considered, although a slightly more intense staining was observed for day 28. A more evident increase in the production of GAGs was observed between day 14 and day 28. It should be noted, however, that since the scaffold contains HA which is a GAG itself the more pronounced Alcian blue staining could be due to "background noise" from the HA content of the bioink. From HE and Alcian Blue images, it is evident that the cells in the structure are sparse. It could, thus, be assumed that the low ECM deposition was due to the low cell density used for bioprinting (6.5×10^6 hMSCs/ml). In fact, cell density has been reported to be positively correlated with the production of ECM with densities of 4×10^6 and 5×10^6 chondrocytes/ml resulting in low GAGs and collagen production [74, 75]. The concentration of ECM close to the sides of the scaffolds was an interesting result that in combination of the reduced scaffold thickness for day 28, could be an indicator of scaffold degradation. Overall, more histological analyses of the self-bent scaffolds are needed that would study ECM production for a longer period of time. Moreover, real-time quantitative PCR tests on the encapsulated cells could also be performed, in order to investigate whether chondrogenic markers can be detected and from which time-point on.

5 Concluding Remarks and Future Perspectives

In conclusion, a 4D bioprinting approach for the fabrication of bilayered scaffolds capable of self-bending upon immersion in a solution, was presented. Control of the scaffolds' curvature was achieved by tuning the infill density, printing angle and layer thickness of the structure, as well as the crosslinking time of the Alg/HA-Tyr layer. It was found that decreasing the infill density resulted in a pronounced increase in the scaffolds' curvature. Furthermore, the thickness of the HA-Tyr part of the bilayers did not significantly affect the obtained curvature. On the contrary, decreasing the Alg/HA-Tyr thickness to half resulted in a two-fold increase of the measured curvature, regardless of the HA-Tyr thickness value. Interestingly, increasing the time of immersion in 200 mM CaCl_2 did not affect the bending of the scaffolds, as it did not have a significant influence on the swelling behavior of the two hydrogels. Additionally, the composition of the swelling solvent was found to have an effect on the obtained curvature, with 0.9% and 5% NaCl solutions triggering the scaffolds to bend the opposite way. Finally, cell-laden, self-bending scaffolds were fabricated by mixing hMSCs with the Alg/HA-Tyr ink. The bioprinted structures were capable of maintaining a high cell viability for up to 14 days, unlocking new strategies for cartilage tissue engineering.

Although the results reported in the present thesis are promising, the research on 4D bioprinting can be further optimized. A secondary crosslinking step could be considered for the bottom part of the bilayered scaffolds in order to enhance the overall strength of the structure. A suggestion could be the addition of a visible light photoinitiator in the formulation of the HA-Tyr ink, such as EO [20] or Rose Benghal [27], which would allow the secondary crosslinking of this layer post-extrusion. However, the swelling properties of the new materials should be distinctly different, in order to achieve self-bending. Additionally, after the shape-shifting phase of the 4D bioprinting is complete, an additional crosslinking step could be considered for the whole structure, in order to enhance the stiffness of the bent scaffold while preserving its curvature. This could, again, be achieved by incorporating a photoinitiator in both inks. However, since the ultimate goal of the present work is 4D bioprinting, the applied wavelength would have to be cytocompatible and the irradiation would have to be performed with the scaffolds still immersed in cell culture medium. Therefore, light diffraction would have to be taken into account during the selection of the suitable wavelength and intensity. Furthermore, future experiments could consider functionalization of the inks by using materials that increase the adhesion of hMSCs in the hydrogel (*e.g.*, tripeptide arginyl-glycyl-aspartic acid (RGD)), allowing them to move in the scaffolds, thus, facilitating their proliferation and differentiation [72, 76]. In addition, the incorporation of a fibrous material in the ink formulation *e.g.*, collagen, could provide adhesion sites while at the same time affecting the cell alignment in the structure during extrusion [42]. Finally, cell incorporation could be extended to both inks using different cell densities per bioink. That way, self-bending scaffolds with a cell-density gradient could be bioprinted, allowing a better biomimicry of native cartilage.

For optimizing the curvature control of the self-bending scaffolds, the effect of other parameters could also be investigated in future experiments. For instance, the influence of temperature changes in the bending would offer an insight on the behavior of the bilayers under various conditions. Furthermore, it would be interesting to conduct degradation studies on both the HA-Tyr and Alg/HA-Tyr inks and examine the changes of the curvature with time.

Starting with those two inks, a material database could be created from their swelling behavior, rheological characterization and compressive tests which could be used for the development of a computational model. The use of such model would, ideally, allow for the prediction of the obtained shape after self-bending and could be used for the fabrication of scaffolds with specific curvature values.

References

- [1] H. Kwon, W. E. Brown, C. A. Lee, D. Wang, N. Paschos, J. C. Hu, and K. A. Athanasiou, “Surgical and tissue engineering strategies for articular cartilage and meniscus repair,” *Nature Reviews Rheumatology*, vol. 15, no. 9, pp. 550–570, 2019.
- [2] P. Räsänen, P. Paavolainen, H. Sintonen, A. M. Koivisto, M. Blom, O. P. Ryyänen, and R. P. Roine, “Effectiveness of hip or knee replacement surgery in terms of quality-adjusted life years and costs,” *Acta Orthopaedica*, vol. 78, no. 1, pp. 108–115, 2007.
- [3] X. Cui, K. Breitenkamp, M. G. Finn, M. Lotz, and D. D. D’Lima, “Direct human cartilage repair using three-dimensional bioprinting technology,” *Tissue Engineering - Part A*, vol. 18, no. 11-12, pp. 1304–1312, 2012.
- [4] C. Vinatier, C. Bouffi, C. Merceron, J. Gordeladze, J.-M. Brondello, C. Jorgensen, P. Weiss, J. Guicheux, and D. Noël, “Cartilage tissue engineering: towards a biomaterial-assisted mesenchymal stem cell therapy,” *Current stem cell research & therapy*, vol. 4, pp. 318–329, dec 2009.
- [5] K. Markstedt, A. Mantas, I. Tournier, H. Martínez Ávila, D. Hägg, and P. Gatenholm, “3D bioprinting human chondrocytes with nanocellulose-alginate bioink for cartilage tissue engineering applications,” *Biomacromolecules*, vol. 16, no. 5, pp. 1489–1496, 2015.
- [6] D. Nguyen, D. A. Hgg, A. Forsman, J. Ekholm, P. Nimkingratana, C. Brantsing, T. Kalogeropoulos, S. Zaunz, S. Concaro, M. Brittberg, A. Lindahl, P. Gatenholm, A. Enejder, and S. Simonsson, “Cartilage Tissue Engineering by the 3D Bioprinting of iPS Cells in a Nanocellulose/Alginate Bioink,” *Scientific Reports*, vol. 7, no. 1, pp. 1–10, 2017.
- [7] Y. Chen, J. Zhang, X. Liu, S. Wang, J. Tao, Y. Huang, W. Wu, Y. Li, K. Zhou, X. Wei, S. Chen, X. Li, X. Xu, L. Cardon, Z. Qian, and M. Gou, “Noninvasive in vivo 3D bioprinting,” *Science Advances*, vol. 6, jun 2020.
- [8] M. Costantini, S. Testa, P. Mozetic, A. Barbetta, C. Fuoco, E. Fornetti, F. Tamiro, S. Bernardini, J. Jaroszewicz, W. Świąszkowski, M. Trombetta, L. Castagnoli, D. Seliktar, P. Garstecki, G. Cesareni, S. Cannata, A. Rainer, and C. Gargioli, “Microfluidic-enhanced 3D bioprinting of aligned myoblast-laden hydrogels leads to functionally organized myofibers in vitro and in vivo,” *Biomaterials*, vol. 131, pp. 98–110, 2017.
- [9] A. Lee, A. R. Hudson, D. J. Shiwarski, J. W. Tashman, T. J. Hinton, S. Yerneni, J. M. Bliley, P. G. Campbell, and A. W. Feinberg, “3D bioprinting of collagen to rebuild components of the human heart,” *Science*, vol. 365, no. 6452, pp. 482–487, 2019.
- [10] J. Groll, T. Boland, T. Blunk, J. A. Burdick, D. W. Cho, P. D. Dalton, B. Derby, G. Forgacs, Q. Li, V. A. Mironov, L. Moroni, M. Nakamura, W. Shu, S. Takeuchi, G. Vozzi, T. B. Woodfield, T. Xu, J. J. Yoo, and J. Malda, “Biofabrication: Reappraising the definition of an evolving field,” *Biofabrication*, vol. 8, no. 1, 2016.
- [11] W. Sun, B. Starly, A. C. Daly, J. A. Burdick, J. Groll, G. Skeldon, W. Shu, Y. Sakai, M. Shinohara, M. Nishikawa, J. Jang, D. W. Cho, M. Nie, S. Takeuchi, S. Ostrovidov, A. Khademhosseini, R. D. Kamm, V. Mironov, L. Moroni, and I. T. Ozbolat, “The bioprinting roadmap,” *Biofabrication*, vol. 12, no. 2, 2020.

- [12] A. Schwab, R. Levato, M. D’Este, S. Piluso, D. Eglin, and J. Malda, “Printability and Shape Fidelity of Bioinks in 3D Bioprinting,” *Chemical Reviews*, vol. 120, no. 19, pp. 11028–11055, 2020.
- [13] D. Petta, U. D’Amora, L. Ambrosio, D. W. Grijpma, D. Eglin, and M. D’Este, “Hyaluronic acid as a bioink for extrusion-based 3D printing,” *Biofabrication*, vol. 12, no. 3, p. 32001, 2020.
- [14] W. Liu, M. A. Heinrich, Y. Zhou, A. Akpek, N. Hu, X. Liu, X. Guan, Z. Zhong, X. Jin, A. Khademhosseini, and Y. S. Zhang, “Extrusion Bioprinting of Shear-Thinning Gelatin Methacryloyl Bioinks,” *Advanced Healthcare Materials*, vol. 6, no. 12, p. 1601451, 2017.
- [15] A. G. Tabriz, M. A. Hermida, N. R. Leslie, and W. Shu, “Three-dimensional bioprinting of complex cell laden alginate hydrogel structures,” *Biofabrication*, vol. 7, no. 4, p. 45012, 2015.
- [16] K. K. Moncal, V. Ozbolat, P. Datta, D. N. Heo, and I. T. Ozbolat, “Thermally-controlled extrusion-based bioprinting of collagen,” *Journal of Materials Science: Materials in Medicine*, vol. 30, no. 5, p. 55, 2019.
- [17] D. Petta, D. W. Grijpma, M. Alini, D. Eglin, and M. D’Este, “Three-Dimensional Printing of a Tyramine Hyaluronan Derivative with Double Gelation Mechanism for Independent Tuning of Shear Thinning and Postprinting Curing,” *ACS Biomaterials Science and Engineering*, vol. 4, no. 8, pp. 3088–3098, 2018.
- [18] A. G. Tabriz, M. A. Hermida, N. R. Leslie, and W. Shu, “Three-dimensional bioprinting of complex cell laden alginate hydrogel structures,” *Biofabrication*, vol. 7, no. 4, 2015.
- [19] T. Billiet, E. Gevaert, T. De Schryver, M. Cornelissen, and P. Dubruel, “The 3D printing of gelatin methacrylamide cell-laden tissue-engineered constructs with high cell viability,” *Biomaterials*, vol. 35, no. 1, pp. 49–62, 2014.
- [20] D. Petta, A. R. Armiento, D. Grijpma, M. Alini, D. Eglin, and M. D’Este, “3D bioprinting of a hyaluronan bioink through enzymatic-and visible light-crosslinking,” *Biofabrication*, vol. 10, no. 4, 2018.
- [21] M. N. Collins and C. Birkinshaw, “Hyaluronic acid based scaffolds for tissue engineering - A review,” *Carbohydrate Polymers*, vol. 92, no. 2, pp. 1262–1279, 2013.
- [22] C. B. Knudson, “Hyaluronan and CD44: Strategic players for cell-matrix interactions during chondrogenesis and matrix assembly,” *Birth Defects Research Part C - Embryo Today: Reviews*, vol. 69, no. 2, pp. 174–196, 2003.
- [23] C. W. Archer and P. Francis-West, “The chondrocyte,” *International Journal of Biochemistry and Cell Biology*, vol. 35, no. 4, pp. 401–404, 2003.
- [24] S. Stichler, T. Böck, N. Paxton, S. Bertlein, R. Levato, V. Schill, W. Smolan, J. Malda, J. Teßmar, T. Blunk, and J. Groll, “Double printing of hyaluronic acid/poly(glycidol) hybrid hydrogels with poly(ϵ -caprolactone) for MSC chondrogenesis,” *Biofabrication*, vol. 9, no. 4, p. 44108, 2017.
- [25] K.-C. Hung, C.-S. Tseng, L.-G. Dai, and S.-h. Hsu, “Water-based polyurethane 3D printed scaffolds with controlled release function for customized cartilage tissue engineering,” *Biomaterials*, vol. 83, pp. 156–168, 2016.

- [26] A. Abbadessa, V. H. M. Mouser, M. M. Blokzijl, D. Gawlitta, W. J. A. Dhert, W. E. Hennink, J. Malda, and T. Vermonden, “A Synthetic Thermosensitive Hydrogel for Cartilage Bioprinting and Its Biofunctionalization with Polysaccharides,” *Biomacromolecules*, vol. 17, pp. 2137–2147, jun 2016.
- [27] C. Loebel, N. Broguiere, M. Alini, M. Zenobi-Wong, and D. Eglin, “Microfabrication of photo-cross-linked hyaluronan hydrogels by single- and two-photon tyramine oxidation,” *Biomacromolecules*, vol. 16, no. 9, pp. 2624–2630, 2015.
- [28] S. N. Pawar and K. J. Edgar, “Alginate derivatization: A review of chemistry, properties and applications,” *Biomaterials*, vol. 33, no. 11, pp. 3279–3305, 2012.
- [29] N. E. Simpson, C. L. Stabler, C. P. Simpson, A. Sambanis, and I. Constantinidis, “The role of the CaCl₂-guluronic acid interaction on alginate encapsulated β TC3 cells,” *Biomaterials*, vol. 25, no. 13, pp. 2603–2610, 2004.
- [30] E. Axpe and M. L. Oyen, “Applications of alginate-based bioinks in 3D bioprinting,” *International Journal of Molecular Sciences*, vol. 17, no. 12, 2016.
- [31] J. Kundu, J.-H. Shim, J. Jang, S.-W. Kim, and D.-W. Cho, “An additive manufacturing-based PCL–alginate–chondrocyte bioprinted scaffold for cartilage tissue engineering,” *Journal of Tissue Engineering and Regenerative Medicine*, vol. 9, pp. 1286–1297, nov 2015.
- [32] K. Markstedt, A. Mantas, I. Tournier, H. Martínez Ávila, D. Hägg, and P. Gatenholm, “3D Bioprinting Human Chondrocytes with Nanocellulose–Alginate Bioink for Cartilage Tissue Engineering Applications,” *Biomacromolecules*, vol. 16, pp. 1489–1496, may 2015.
- [33] M. Müller, E. Öztürk, Ø. Arlov, P. Gatenholm, and M. Zenobi-Wong, “Alginate Sulfate–Nanocellulose Bioinks for Cartilage Bioprinting Applications,” *Annals of Biomedical Engineering*, vol. 45, no. 1, pp. 210–223, 2017.
- [34] A. A. Giannopoulos, D. Mitsouras, S.-J. Yoo, P. P. Liu, Y. S. Chatzizisis, and F. J. Rybicki, “Applications of 3D printing in cardiovascular diseases,” *Nature reviews. Cardiology*, vol. 13, no. 12, pp. 701–718, 2016.
- [35] D. Richards, J. Jia, M. Yost, R. Markwald, and Y. Mei, “3D Bioprinting for Vascularized Tissue Fabrication,” *Annals of Biomedical Engineering*, vol. 45, no. 1, pp. 132–147, 2017.
- [36] C. Frantz, K. M. Stewart, and V. M. Weaver, “The extracellular matrix at a glance,” *Journal of Cell Science*, vol. 123, no. 24, pp. 4195–4200, 2010.
- [37] W. J. Hendrikson, J. Rouwkema, F. Clementi, C. A. Van Blitterswijk, S. Farè, and L. Moroni, “Towards 4D printed scaffolds for tissue engineering: Exploiting 3D shape memory polymers to deliver time-controlled stimulus on cultured cells,” *Biofabrication*, vol. 9, no. 3, 2017.
- [38] S. H. Kim, Y. B. Seo, Y. K. Yeon, Y. J. Lee, H. S. Park, M. T. Sultan, J. M. Lee, J. S. Lee, O. J. Lee, H. Hong, H. Lee, O. Ajiteru, Y. J. Suh, S. H. Song, K. H. Lee, and C. H. Park, “4D-bioprinted silk hydrogels for tissue engineering,” *Biomaterials*, vol. 260, no. July, p. 120281, 2020.

- [39] G. H. Yang, W. Kim, J. Kim, and G. H. Kim, “A skeleton muscle model using GelMA-based cell-aligned bioink processed with an electric-field assisted 3D/4D bioprinting,” *Theranostics*, vol. 11, no. 1, pp. 48–63, 2020.
- [40] Y. Luo, “Cell-laden four-dimensional bioprinting using near-infrared-triggered shape-morphing alginate / polydopamine bioinks,” *Biofabrication*, no. 11, 2019.
- [41] A. Kirillova, R. Maxson, G. Stoychev, C. T. Gomillion, and L. Ionov, “4D Biofabrication Using Shape-Morphing Hydrogels,” *Advanced Materials*, vol. 29, no. 46, 2017.
- [42] A. Schwab, C. H elary, R. G. Richards, M. Alini, D. Eglin, and M. D’Este, “Tissue mimetic hyaluronan bioink containing collagen fibers with controlled orientation modulating cell migration and alignment,” *Materials Today Bio*, vol. 7, no. June, pp. 1–13, 2020.
- [43] T. G. Mezger, *The Rheology Handbook*. Vincentz Network, dec 2019.
- [44] A. Ribeiro, M. M. Blokzijl, R. Levato, C. W. Visser, M. Castilho, W. E. Hennink, T. Vermonden, and J. Malda, “Assessing bioink shape fidelity to aid material development in 3D bioprinting,” *Biofabrication*, vol. 10, no. 1, 2018.
- [45] R. P. Chhabra, “Non-Newtonian fluids: An introduction,” *Rheology of Complex Fluids*, pp. 3–34, 2010.
- [46] J. Schindelin, I. Arganda-Carreras, E. Frise, V. Kaynig, M. Longair, T. Pietzsch, S. Preibisch, C. Rueden, S. Saalfeld, B. Schmid, J.-Y. Tinevez, D. J. White, V. Hartenstein, K. Eliceiri, P. Tomancak, and A. Cardona, “Fiji: an open-source platform for biological-image analysis,” *Nature Methods*, vol. 9, no. 7, pp. 676–682, 2012.
- [47] S. Timoshenko, “Analysis of Bi-Metal Thermostats,” *Journal of the Optical Society of America*, vol. 11, no. 3, p. 233, 1925.
- [48] I. Apsite, G. Constante, M. Dulle, L. Vogt, A. Caspari, A. R. Boccaccini, A. Synytska, S. Salehi, and L. Ionov, “4D Biofabrication of fibrous artificial nerve graft for neuron regeneration,” *Biofabrication*, vol. 12, no. 3, 2020.
- [49] C. Cui, D. O. Kim, M. Y. Pack, B. Han, L. Han, Y. Sun, and L. H. Han, “4D printing of self-folding and cell-encapsulating 3D microstructures as scaffolds for tissue-engineering applications,” *Biofabrication*, vol. 12, no. 4, 2020.
- [50] S. Naficy, R. Gately, R. Gorkin, H. Xin, and G. M. Spinks, “4D Printing of Reversible Shape Morphing Hydrogel Structures,” *Macromolecular Materials and Engineering*, vol. 302, no. 1, pp. 1–9, 2017.
- [51] L. R. G. Treloar, “The Physics of Rubber Elasticity,” p. 322, 1975.
- [52] M. Rubinstein and R. H. Colby, *Polymer Physics*. Oxford University Press, 6th ed., 2003.
- [53] R. Narcisi, W. J. L. M. Koevoet, and G. J. V. M. van Osch, “Expansion and Chondrogenic Differentiation of Human Bone Marrow-Derived Mesenchymal Stromal Cells BT - Osteoporosis and Osteoarthritis,” pp. 15–28, New York, NY: Springer US, 2021.
- [54] “Live/Dead Quantification Using Fiji – Step-by-Step Guide,” 2020.

- [55] P. Soille and L. M. Vincent, “Determining watersheds in digital pictures via flooding simulations,” in *Proc.SPIE*, vol. 1360, 1990.
- [56] J. Ge, L. Guo, S. Wang, Y. Zhang, T. Cai, R. C. H. Zhao, and Y. Wu, “The size of mesenchymal stem cells is a significant cause of vascular obstructions and stroke,” *Stem cell reviews and reports*, vol. 10, no. 2, pp. 295–303, 2014.
- [57] A. McColloch, M. Rabiei, P. Rabbani, A. Bowling, and M. Cho, “Correlation between Nuclear Morphology and Adipogenic Differentiation: Application of a Combined Experimental and Computational Modeling Approach,” *Scientific Reports*, vol. 9, no. 1, p. 16381, 2019.
- [58] N. Schmitz, S. Laverty, V. B. Kraus, and T. Aigner, “Basic methods in histopathology of joint tissues.,” *Osteoarthritis and cartilage*, vol. 18 Suppl 3, pp. S113–6, oct 2010.
- [59] M. E. Cooke and D. H. Rosenzweig, “The rheology of direct and suspended extrusion bioprinting,” *APL Bioengineering*, vol. 5, no. 1, pp. 1–20, 2021.
- [60] T. Gao, G. J. Gillispie, J. S. Copus, A. P. Kumar, Y. J. Seol, A. Atala, J. J. Yoo, and S. J. Lee, “Optimization of gelatin-alginate composite bioink printability using rheological parameters: A systematic approach,” *Biofabrication*, vol. 10, no. 3, 2018.
- [61] A. Skardal, J. Zhang, and G. D. Prestwich, “Bioprinting vessel-like constructs using hyaluronan hydrogels crosslinked with tetrahedral polyethylene glycol tetracrylates,” *Biomaterials*, vol. 31, no. 24, pp. 6173–81, 2010.
- [62] Y. Gu, L. Zhang, X. Du, Z. Fan, L. Wang, W. Sun, Y. Cheng, Y. Zhu, and C. Chen, “Reversible physical crosslinking strategy with optimal temperature for 3D bioprinting of human chondrocyte-laden gelatin methacryloyl bioink,” *Journal of Biomaterials Applications*, vol. 33, no. 5, pp. 609–618, 2018.
- [63] L. Ouyang, R. Yao, Y. Zhao, and W. Sun, “Effect of bioink properties on printability and cell viability for 3D bioplotting of embryonic stem cells,” *Biofabrication*, vol. 8, no. 3, 2016.
- [64] C. B. Shah and S. M. Barnett, “Swelling behavior of hyaluronic acid gels,” *Journal of Applied Polymer Science*, vol. 45, no. 2, pp. 293–298, 1992.
- [65] M. A. LeRoux, F. Guilak, and L. A. Setton, “Compressive and shear properties of alginate gel: Effects of sodium ions and alginate concentration,” *Journal of Biomedical Materials Research*, vol. 47, no. 1, pp. 46–53, 1999.
- [66] S. K. Bajpai and S. Sharma, “Investigation of swelling/degradation behaviour of alginate beads crosslinked with Ca²⁺ and Ba²⁺ ions,” *Reactive and Functional Polymers*, vol. 59, no. 2, pp. 129–140, 2004.
- [67] S. Saitoh, Y. Araki, R. Kon, H. Katsura, and M. Taira, “Swelling/deswelling Mechanism of Calcium Alginate Gel in Aqueous Solutions,” *Dental Materials Journal*, vol. 19, no. 4, pp. 396–404, 2000.
- [68] J. Emmermacher, D. Spura, J. Cziommer, D. Kilian, T. Wollborn, U. Fritsching, J. Steingroewer, T. Walther, M. Gelinsky, and A. Lode, “Engineering considerations on extrusion-based bioprinting: interactions of material behavior, mechanical forces and cells in the printing needle,” *Biofabrication*, vol. 12, no. 2, 2020.

- [69] L. Ning, A. Guillemot, J. Zhao, G. Kipouros, and X. Chen, “Influence of Flow Behavior of Alginate–Cell Suspensions on Cell Viability and Proliferation,” *Tissue Engineering Part C: Methods*, vol. 22, pp. 652–662, may 2016.
- [70] N. Paxton, W. Smolan, T. Böck, F. Melchels, J. Groll, and T. Jungst, “Proposal to assess printability of bioinks for extrusion-based bioprinting and evaluation of rheological properties governing bioprintability,” *Biofabrication*, vol. 9, no. 4, 2017.
- [71] K. A. Deo, K. A. Singh, C. W. Peak, D. L. Alge, and A. K. Gaharwar, “Bioprinting 101: Design, Fabrication, and Evaluation of Cell-Laden 3D Bioprinted Scaffolds,” *Tissue Engineering - Part A*, vol. 26, no. 5-6, pp. 318–338, 2020.
- [72] J. A. Rowley, G. Madlambayan, and D. J. Mooney, “Alginate hydrogels as synthetic extracellular matrix materials,” *Biomaterials*, vol. 20, no. 1, pp. 45–53, 1999.
- [73] A. Frayssinet, D. Petta, C. Illoul, B. Haye, A. Markitantova, D. Eglin, G. Mosser, M. D’Este, and C. Hélyary, “Extracellular matrix-mimetic composite hydrogels of cross-linked hyaluronan and fibrillar collagen with tunable properties and ultrastructure,” *Carbohydrate Polymers*, vol. 236, no. January, p. 116042, 2020.
- [74] G. M. Williams, T. J. Klein, and R. L. Sah, “Cell density alters matrix accumulation in two distinct fractions and the mechanical integrity of alginate-chondrocyte constructs,” *Acta Biomaterialia*, vol. 1, no. 6, pp. 625–633, 2005.
- [75] A. Troken, N. Marion, S. Hollister, and J. Mao, “Tissue engineering of the synovial joint: the role of cell density.,” *Proceedings of the Institution of Mechanical Engineers. Part H, Journal of engineering in medicine*, vol. 221, pp. 429–40, jul 2007.
- [76] J. Jia, D. J. Richards, S. Pollard, Y. Tan, J. Rodriguez, R. P. Visconti, T. C. Trusk, M. J. Yost, H. Yao, R. R. Markwald, and Y. Mei, “Engineering alginate as bioink for bioprinting,” *Acta Biomaterialia*, vol. 10, no. 10, pp. 4323–4331, 2014.
- [77] Molecular Probes and I. D. Technologies, “LIVE/DEAD Viability/Cytotoxicity Kit for mammalian cells Protocol,” pp. 1–7, 2005.
- [78] Invitrogen, “PrestoBlue [®] Cell Viability Reagent Product Information Sheet,” pp. 0–1, 2019.

Appendices

APPENDIX A: Effect of CaCl₂ concentration and exposure time on hMSCs

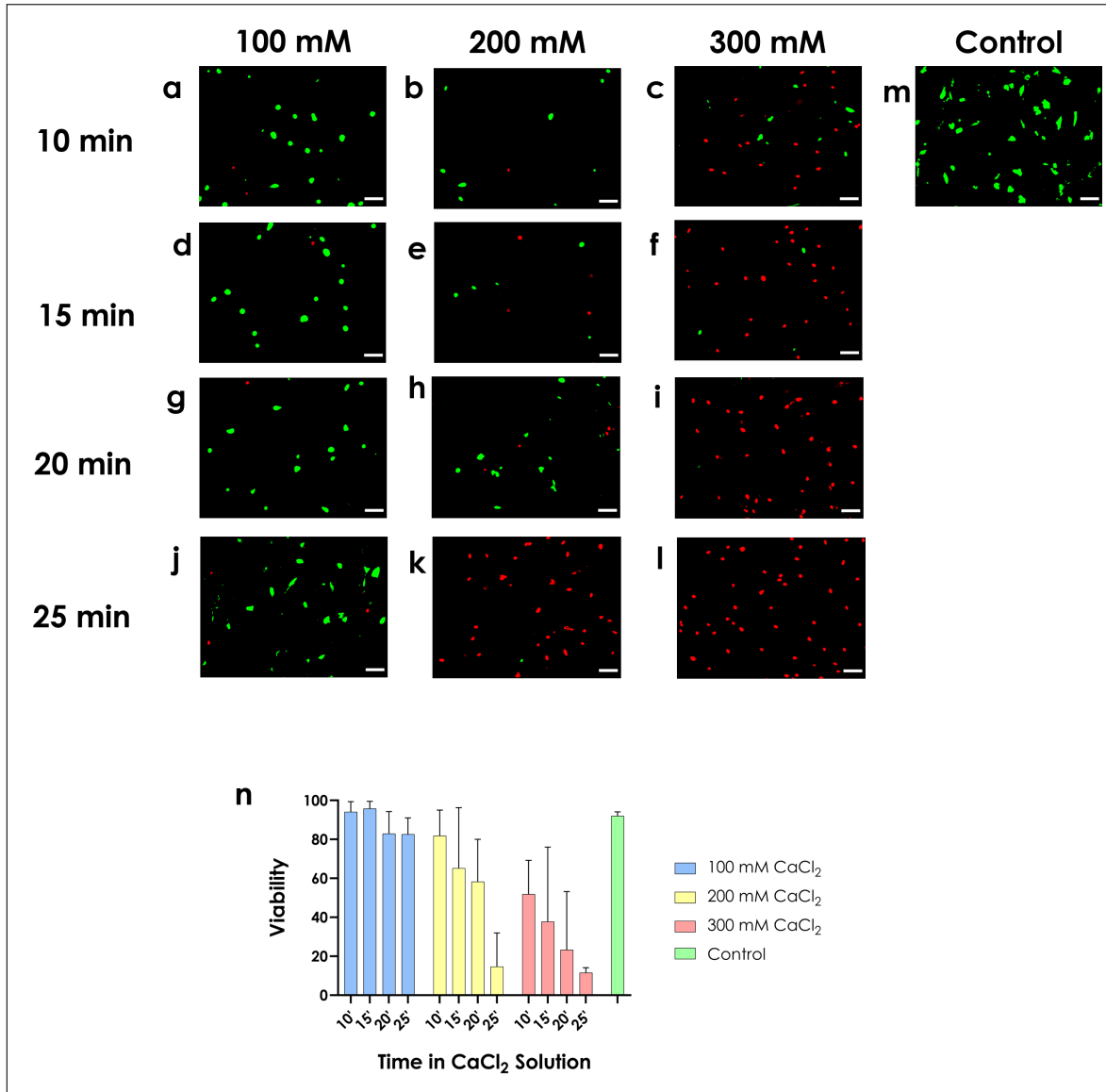


Figure 19: Effect of CaCl₂ concentration and exposure time on hMSCs viability. (a-l) Representative merged, fluorescent Live/Dead images of hMSCs incubated for (10 min, 15 min, 20 min, 25 min) with 100 mM (a, d, g, j), 200 mM (b, e, h, k) and 300 mM CaCl₂ (c, f, i, l). (m) Live/Dead image of hMSCs without any exposure to CaCl₂ (control). (n) Quantification of the viability measured from Live/Dead assay. Scale bars: 100 μ m.

APPENDIX B: Cell Viability Assays: Protocol Optimization

When considering a three-dimensional structure laden with cells, the commonly used protocols for cells cultured in well plates might have to be altered by taking into account that staining substances might need more time to reach sites located deeper in the structure. Moreover, while performing the Live/Dead assessment, red particles, indicating dead cells, were observed to coincide with green particles. Based on the supplier's recommendations [77], the calcein concentration as well as incubation time were increased and cell viability and morphology were measured for each case (Fig. 21). Although differences in the measured viability and cell area when using an increased concentration of calcein (10 μM instead of 2 μM) were indeed observed, some red particles continued to be present at the same sites as green particles (indicated with orange arrows in Fig. 21a-d). In addition, the effect of incubation time of the scaffolds with the Presto blue solution on the obtained fluorescent readings was investigated (Fig. 20). According to the supplier's recommendation, an incubation time of up to 3 h can be used to increase the sensitivity of detection [78]. Thus, scaffolds were incubated for 1, 2 and 3 h and the corresponding RFU were measured. As the 3 h incubation gave a significantly higher reading, this incubation time was selected for conducting the analyses described in the following section.

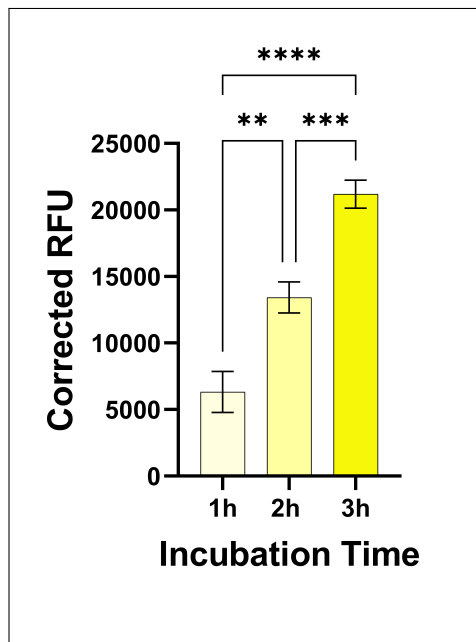


Figure 20: Optimization of Presto Blue protocol using increased incubation times Corrected RFU's are presented for bioprinted bilayered scaffolds laden with hMSCs after 14 days of incubation in cell expansion medium.

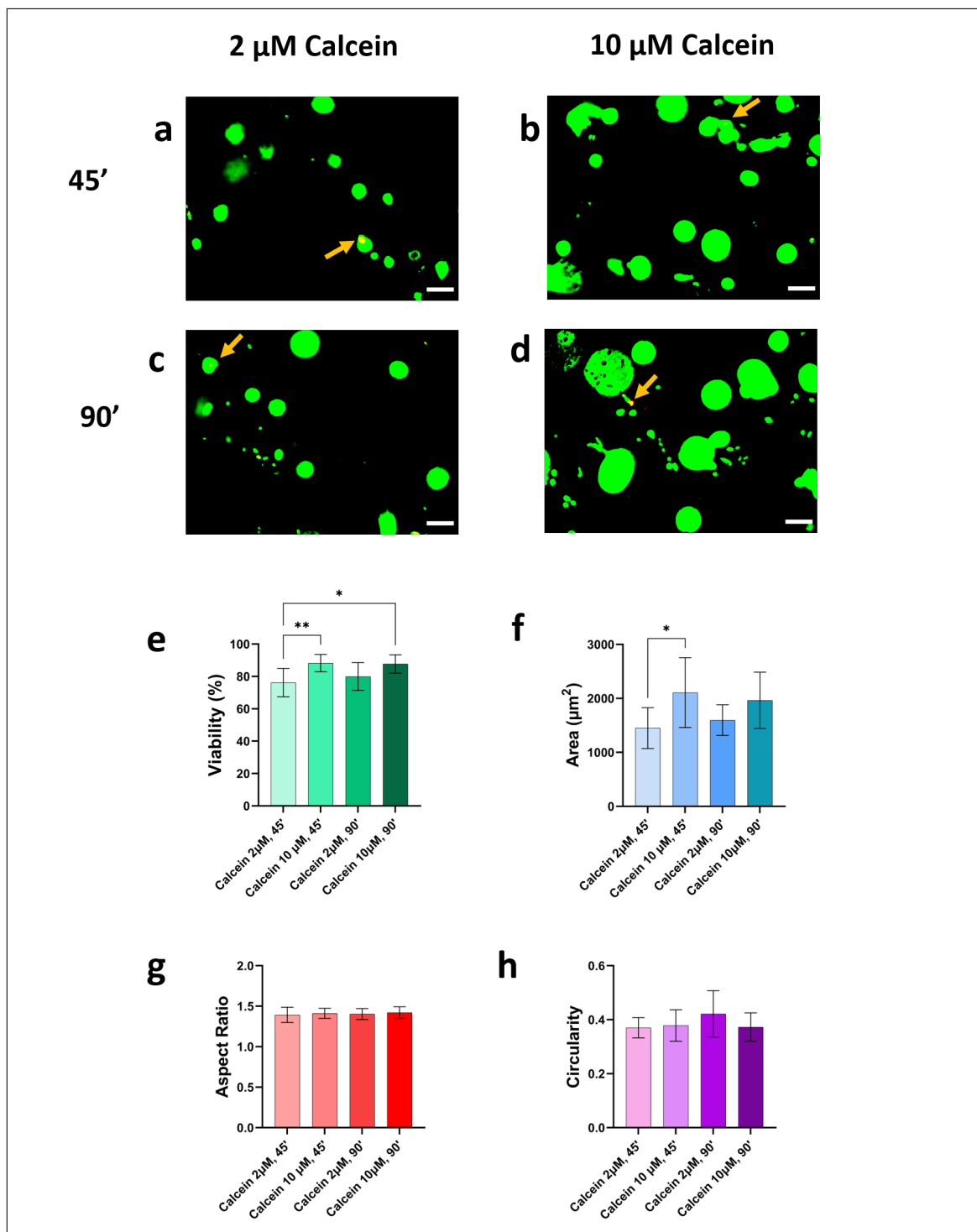


Figure 21: Effect of calcein AM concentration and incubation time on measured viability. (a, b) Live/Dead fluorescent microscopy images for a 45 min incubation using 2 μM and 10 μM calcein AM, respectively. (c, d) Live/Dead fluorescent microscopy images for a 90 min incubation using 2 μM and 10 μM calcein AM, respectively. EthD-1 concentration was kept constant at 3 μM for all the experiments. (e-h) Quantification of cell viability (e) and shape factors including cell area (f), cell aspect ratio (g) and cell circularity (h). Orange arrows illustrate apoptotic cells where the summation of the red and green fluorescence from different planes resulted in an apparent yellow fluorescence. Scale bars: 100 μm .

APPENDIX C: Images of 4D Bioprinted Scaffolds.

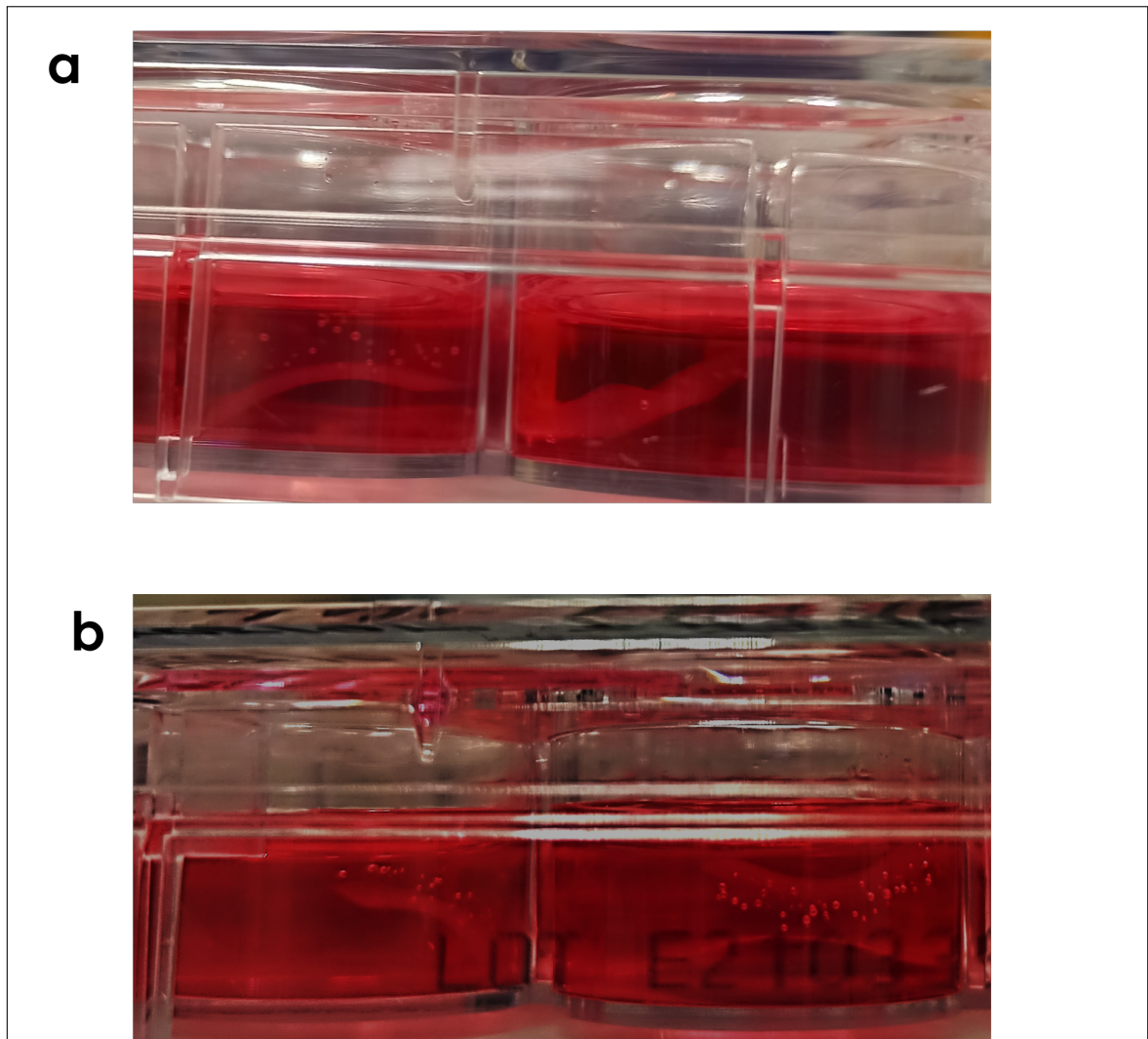


Figure 22: Images of the bioprinted scaffolds immersed in chondrogenic medium 24 h after fabrication.

APPENDIX D: Scaffold Stability

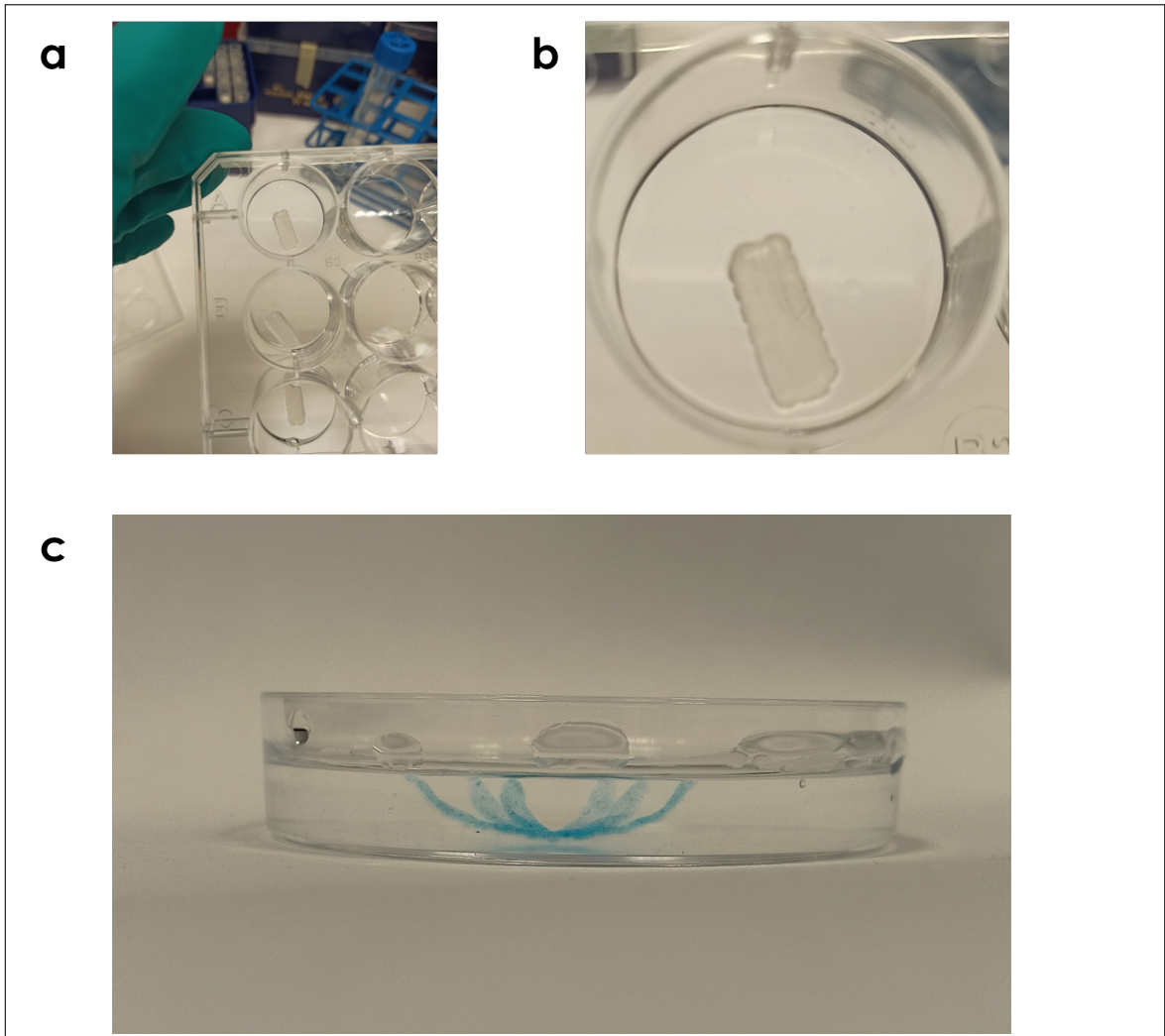


Figure 23: Examples of the stability of bilayered (bio)printed structures. Images of bioprinted, bilayered scaffolds from a cell-free bottom part of HA-Tyr and a hMSCs-laden top part of Alg/HA-Tyr after 14 days of incubation in chondrogenic medium and overnight fixation in 4% PFA. Printing paths are still visible. (c) Image of a cell-free bilayered flower-shaped scaffold, 35 days after fabrication at room temperature. The flower is imaged immersed in 0.9% NaCl with 2 mM CaCl_2 .

APPENDIX E: Use of DMEM in ink preparation

Preliminary experiments were conducted using using medium instead of 0.9% NaCl for the preparation of the inks. During printing, though, it was observed that the two inks were very fluid and could not form continuous filaments with reliable shape retention. Therefore, more H₂O₂ was added to the formulations, reaching a final concentration of 0.2 mM (instead of 0.17 mM that was previously used). After this addition, the two inks exhibited a better printability and the fabrication of bilayered scaffolds was achieved. Subsequently, scaffolds were crosslinked with 200 mM CaCl₂ and washed twice, as previously described. The self-bending capacity of the structures was studied in both media types, namely expansion and chondrogenic media. This experiment was only carried out once and, thus, the preliminary results presented here should be verified by repetitions.

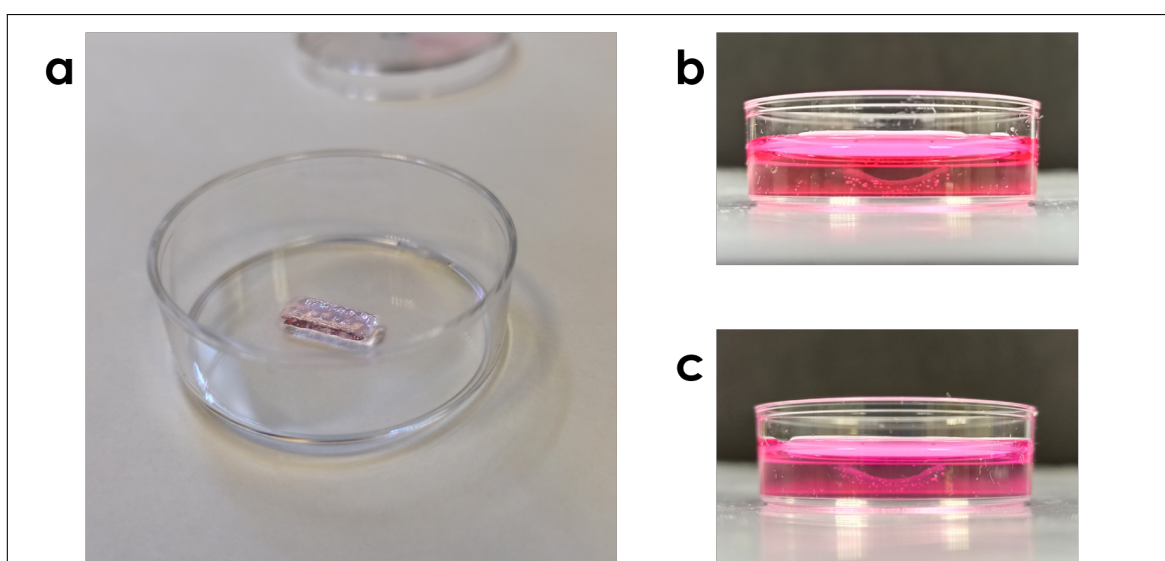


Figure 24: bilayered scaffolds from HA-Tyr and Alg/HA-Tyr prepared with DMEM. (a) The scaffolds after printing. Scaffolds after 2 h immersion in (b) DMEM and (c) α MEM.

Appendix F: Molding and Staining Protocols

Table 4: Dehydration of Hydrogels and Agarose-Embedded Pellets. Table abbreviations: EtOH: ethanol, RT: Room Temperature.

Step	Solution	Time (min)	Temperature
1	70% EtOH	30	RT
2	80% EtOH	60	RT
3	90% EtOH	60	RT
4	100% EtOH	60	RT
5	100% EtOH	30	RT
6	100% EtOH	30	RT
7	100% Xylene	30	RT
8	100% Xylene	30	RT

Table 5: Histochemical Staining of Collagen Fibers: Picrosirius Red Staining Protocol Table abbreviations: EtOH: ethanol, RT: Room Temperature.

Step	Solution	Time (min)	Temperature
1	Xylene	5 min	RT
2	Xylene	5 min	RT
3	100% EtOH	5 min	RT
4	100% EtOH	5 min	RT
5	95% EtOH	3 min	RT
6	95% EtOH	3 min	RT
7	70% EtOH	3 min	RT
8	Deionized H ₂ O	5 min	RT
9	Picrosirius Red	60 min	RT
10	0.5% Acetic Acid	30 sec	RT
11	0.5% Acetic Acid	30 sec	RT
12	Deionized H ₂ O	30 sec	RT
13	Deionized H ₂ O	30 sec	RT
14	95% EtOH	20 sec	RT
15	95% EtOH	20 sec	RT
16	100% EtOH	20 sec	RT
17	100% EtOH	20 sec	RT
18	Xylene	3 min	RT
19	Xylene	3 min	RT
20	Mount with DPX and coverslip		RT

Table 6: Histochemical Staining of Glycosaminoglycan Content: Alcian Blue Staining Protocol. Table abbreviations: EtOH: Ethanol, RT: Room Temperature.

Step	Solution	Time (min)	Temperature
1	Xylene	5 min	RT
2	Xylene	5 min	RT
3	100% EtOH	5 min	RT
4	100% EtOH	5 min	RT
5	95% EtOH	3 min	RT
6	95% EtOH	3 min	RT
7	70% EtOH	3 min	RT
8	Deionized H ₂ O	5 min	RT
9	Alcian Blue	5 min	RT
10	Deionized H ₂ O	1 min	RT
11	Deionized H ₂ O	1 min	RT
12	Deionized H ₂ O	1 min	RT
13	95% EtOH	20 sec	RT
14	95% EtOH	20 sec	RT
15	100% EtOH	20 sec	RT
16	100% EtOH	20 sec	RT
17	Xylene	3 min	RT
18	Xylene	3 min	RT
19	Mount with DPX and coverslip		RT

Table 7: Histochemical Staining For General Assessment of Cell and Tissue Morphology: Hematoxylin-Eosin Staining Protocol. Table abbreviations: EtOH: Ethanol, RT: Room Temperature.

Step	Solution	Time (min)	Temperature
1	Xylene	5 min	RT
2	Xylene	5 min	RT
3	100% EtOH	5 min	RT
4	100% EtOH	5 min	RT
5	95% EtOH	3 min	RT
6	95% EtOH	3 min	RT
7	70% EtOH	3 min	RT
8	Deionized H ₂ O	3 min	RT
9	Hematoxylin	4 min	RT
10	Running tap H ₂ O	10 min	RT
11	Acid Alcohol	5 dips	RT
12	Tap H ₂ O	5 min	RT
13	Eosin Y	2 min	RT
14	95% EtOH	3 min	RT
15	95% EtOH	3 min	RT
16	100% EtOH	3 min	RT
17	100% EtOH	3 min	RT
18	Xylene	3 min	RT
19	Xylene	3 min	RT
20	Mount with DPX and coverslip		RT

List of Figures

1	Schematic illustration of shape-shifting 4D bioprinting.	8
2	Schematic illustration of the three-state transition of an ink during extrusion. Figure abbreviations: G' : storage modulus, G'' : loss modulus, $\tan\delta$: damping factor, η : viscosity, $\dot{\gamma}$: shear rate.	10
3	Printing Setup. (a) The bioprinter in the biosafety cabinet with two cartridges equipped with the 25G nozzles. (b) Top view of a bilayered scaffold sample. Scale bar: 10 mm. (c) Printing speed tests with 2 mm/s (left), 5 mm/s (middle) and 10 mm/s (right) for HA-Tyr (top) and Alg/HA-Tyr (bottom). Scale bars 5 mm.	13
4	Infill Density and Printing Angle Combinations. (a-c) Illustrations of a single layer printed with a 0° printing angle and (a) 40%, (b) 50%, (c) 60% infill densities. (d-f) Illustrations of a single layer printed with a 90° printing angle and (d) 40%, (e) 50% and (f) 60% infill densities. (g, h) Illustrations of two layers printed with (g) the 0° - 90° combination and (h) the 90° - 0° combination. The infill used for the last two illustrations was 60%.	14
5	Compression Tests. (a) The compression test setup. A glass slide with a test sample has been placed between the 2-inch parallel plates. (b) Alg/HA-Tyr and (c) HA-Tyr scaffolds for compression tests. Scale bars: 10 mm.	15
6	Graphic illustration of the swelling induced bending of bilayered structure (cross-section view). The bilayered beam before, (a), and after bending (b). Figure nomenclature: h : the total thickness, α_1, α_2 : the thickness of the top and bottom layer, respectively, E_1, E_2 : the compressive moduli of the top and bottom layer, respectively, λ_1, λ_2 : the linear expansion rate of the top and bottom layers, respectively, ρ : the radius of curvature.	17
7	4D bioprinting of self-bending bilayered scaffolds.	20
8	Rheological characterization of HA-Tyr and Alg/HA-Tyr inks. (a) Time dependence of the storage (G') and loss modulus (G'') of HA-Tyr (red) and Alg/HA-Tyr (blue). (b) The plateau values of G' and G'' for HA-Tyr (red) and Alg/HA-Tyr (blue). (c) Amplitude strain sweep for HA-Tyr (red) and Alg/HA-Tyr (blue) inks. Storage moduli, G' , are plotted as closed squares while loss moduli, G'' , are plotted as open squares. (d) Yield stress values of HA-Tyr (red) and Alg/HA-Tyr (blue). (e) Frequency dependence of the storage (G') (closed circles) and loss modulus (G'') (open circles) of HA-Tyr (red) and Alg/HA-Tyr (blue). (f) Shear rate, $\dot{\gamma}$, dependence of the shear viscosity, η of the HA-Tyr (red) and Alg/HA-Tyr (blue). Oscillatory thixotropy tests for HA-Tyr (g) and Alg/HA-Tyr (h).	27
9	Single-material Scaffold Characterization (a) Compression moduli of Alg/HA-Tyr and HA-Tyr scaffolds. (b) Swelling ratios of Alg/HA-Tyr and HA-Tyr scaffolds after immersion in 0.9% NaCl with 2 mM CaCl ₂	28

10	Different scaffold designs during the slicing (left), 3D printing (middle) and 4D printing (right) steps of the fabrication process. (a) Rectangular scaffold with a zig-zag infill pattern of $0^\circ - 90^\circ - 0^\circ$. (b) Cross-shaped, (c) star-shaped and (d) flower-shaped scaffolds with a line infill pattern ($45^\circ - 135^\circ$) and a single-wall shell. All designs (a–d) comprise of two bottom layers made from HA-Tyr and one top layer made of Alg/HA-Tyr. Slicing of scaffolds was performed using Cura. Shape-shifted scaffolds are imaged submerged in 0.9% NaCl with 2 mM CaCl ₂ . Scale bars: 10 mm.	29
11	The effect of infill density and printing pattern on self-bending. (a-l) Side-view images of bilayered, self-bent scaffolds from HA-Tyr and Alg/HA-Tyr immersed in 0.9% NaCl with 2 mM CaCl ₂ . The pictures were obtained 2 h and 24 h after scaffold immersion in the swelling solvent. (m) Quantification of the curvatures measured per infill density and printing pattern combination for 2 h (yellow) and 24 h (cyan) of immersion. Scale bars: 10 mm.	31
12	The effect of thickness ratio on self-bending. (a-c) Schematic illustration of the scaffold design for the 1:1 (a), 1:2 (b) and 1:3 (c) conditions. α_1 : the thickness of the Alg/HA-Tyr layer, α_2 : the thickness of the HA-Tyr layer. (d-f) Images of the scaffolds being submerged for 2 h in 0.9% NaCl with 2 mM CaCl ₂ . (g-i) Images of the scaffolds being submerged for 24 h in 0.9% NaCl with 2 mM CaCl ₂ . (j) Quantification of the curvature values measured for the 1:1, 1:2 and 1:3 conditions after 2 h (blue) and 24 h (yellow) in the aforementioned swelling solvent. Scale bars: 10 mm.	33
13	Effect of CaCl₂ immersion time in the curvature. (a-h) Images of bilayered scaffolds from HA-Tyr and Alg/HA-Tyr acquired 2 h (a-d) and 24 h (e-h) after immersion in 0.9% NaCl with 2 mM CaCl ₂ . The depicted scaffolds were immersed in 200 mM CaCl ₂ for 10 min (a, e), 15 min (b, f), 20 min (c, g) or 25 min (d, h), before being transferred to the swelling solution. (i) Quantification of the curvature values measured for 10, 15, 20 and 25 min of CaCl ₂ immersion, after 2 h (blue) and 24 h (yellow) in the swelling solvent. (j, k) Swelling ratios measured for the four conditions described above, using single-material scaffolds printed with Alg/HA-Tyr (j) (orange: 2 h swelling, pink: 24 h swelling) and HA-Tyr (k) (lilac: 2 h swelling, purple: 24 h swelling). (l) Compression moduli of single-material scaffolds made of HA-Tyr (red), and Alg/HA-Tyr crosslinked for 10 min (blue), 15 min (light blue), 20 min (dark green) or 25 min (light green). Scale bars: 10 mm.	35
14	Effect of swelling solvent composition on curvature. (continued on next page)	37

14	(continued) (a-k) Images of bilayered scaffolds from HA-Tyr and Alg/HA-Tyr acquired 2 h (a-c, g-i) and 24 h (d-f, j, k) after immersion in the following solutions: 0.9% NaCl (a, d) (the blue “x” represents the lack of image due to scaffold break), 5% NaCl (b, e) , 10% NaCl (c, f) , DMEM (g, j) , 0.9% NaCl with 2 mM CaCl ₂ (h, k) and deionized (di) H ₂ O i, l . Swelling ratios measured for single material scaffolds from Alg/HA-Tyr (orange) and HA-Tyr (lilac) after 2 (m) and 24 h (n) of immersion in the aforementioned solvents. (o) Quantification of the curvature values measured for each of the above solutions, after 2h (blue) and 24 h (yellow). Negative values correspond to a concave down bending. The black line pattern of the bar representing the curvature in di H ₂ O after 24 h corresponds to the absence of the bottom HA-Tyr layer. Scale bars: 10 mm.	38
15	Pellet study for investigating the chondrogenic capacity of hMSCs and determining the optimal medium. (continued on next page) . . .	40
15	(continued) (a-i) Representative microscopy images of slices from paraffin-embedded hMSC pellets stained with Picrosirius red (a, d, g) , Alcian blue (b, e, h) and haematoxylin-eosin (c, f, i) . The images show a control pellet (a-c) , a pellet cultured for 21 days in CM-E (d-f) and a pellet cultured for 21 days in CM-L (g-i) . Images depicting the whole pellet were acquired with a 10× objective (N.A.: 0.25) (a-i, top) , while close-ups from the same pellets were acquired using a 40× objective (N.A.: 0.65) (a-i, bottom) . (j) Quantification of metabolic activity using fluorescence readings of Presto blue assay for pellets cultured in CM-L (light pink) and CM-E (dark pink) for 14 and 21 days. Scale bars: 100 μm.	41
16	4D Bioprinting: Viability and proliferation assessment of hMSCs in bilayered scaffolds from Alg/HA-Tyr and HA-Tyr incubated in expansion medium. (a-c) Merged fluorescent images from Live/Dead assay of the Alg/HA-Tyr layer of the bilayered scaffolds. Green color indicates the presence of viable cells stained with calcein while red color indicates the nuclei of dead cells stained with EthD-1. Images were acquired after 1 (a) , 7 (b) and 14 (c) days of incubation with cell expansion medium. (d-f) Quantification of cell viability (d) , cell area (e) and cell circularity (f) after 1, 7 and 14 days of incubation. (g) Quantification of hMSCs metabolic activity using fluorescent readings of Presto blue for 1, 7 and 14 days of incubation. Scale bars: 100 μm.	42

17	4D Bioprinting: Viability and proliferation assessment of hMSCs in bilayered scaffolds from Alg/HA-Tyr and HA-Tyr incubated in chondrogenic medium.	(a-c) Merged fluorescent images of Live/Dead assay of the hMSCs-laden Alg/HA-Tyr layer part of bilayered scaffolds from HA-Tyr and Alg/HA-Tyr. (d-f) Merged fluorescent images of hMSCs-laden Alg/HA-Tyr scaffolds. Live/Dead images were acquired after 1 (a, d), 7 (b, e) and 14 days (c, f) of incubation in CM-E medium. Quantification of cell viability (g), cell area (h) and cell circularity (i) for the bilayered (plain-colored bars) and the single-material scaffolds (patterned bars), after 1, 7 and 14 days of incubation. (j) Fluorescence readings of the cell-viability Presto blue assay after 1, 7 and 14 days. RFU: relevant fluorescent unit. Scale bars: 100 μm	44
18	Histology of 4D bioprinted bilayered scaffolds.	Representative images after 14 (a-c), 21 (d-f) and 28 days (g-i). The three stains imaged are Heamatoxylin-Eosin (HE) (a, d, g), Alcian Blue (AB) (b, e, h) and Picrosirius Red (PR) (c, f, i). Scale bars: 1 mm (top images), 100 μm (bottom images).	45
19	Effect of CaCl₂ concentration and exposure time on hMSCs viability.	(a-l) Representative merged, fluorescent Live/Dead images of hMSCs incubated for (10 min, 15 min, 20 min, 25 min) with 100 mM (a, d, g, j), 200 mM (b, e, h, k) and 300 mM CaCl ₂ (c, f, i, l). (m) Live/Dead image of hMSCs without any exposure to CaCl ₂ (control). (n) Quantification of the viability measured from Live/Dead assay. Scale bars: 100 μm	58
20	Optimization of Presto Blue protocol using increased incubation times	Corrected RFU's are presented for bioprinted bilayered scaffolds laden with hMSCs after 14 days of incubation in cell expansion medium.	59
21	Effect of calcein AM concentration and incubation time on measured viability.	(a, b) Live/Dead fluorescent microscopy images for a 45 min incubation using 2 μM and 10 μM calcein AM, respectively. (c, d) Live/Dead fluorescent microscopy images for a 90 min incubation using 2 μM and 10 μM calcein AM, respectively. EthD-1 concentration was kept constant at 3 μM for all the experiments. (e-h) Quantification of cell viability (e) and shape factors including cell area (f), cell aspect ratio (g) and cell circularity (h). Orange arrows illustrate apoptotic cells where the summation of the red and green fluorescence from different planes resulted in an apparent yellow fluorescence. Scale bars: 100 μm	60
22	Images of the bioprinted scaffolds immersed in chondrogenic medium 24 h after fabrication.	61

23	Examples of the stability of bilayered (bio)printed structures. Images of bioprinted, bilayered scaffolds from a cell-free bottom part of HA-Tyr and a hMSCs-laden top part of Alg/HA-Tyr after 14 days of incubation in chondrogenic medium and overnight fixation in 4% PFA. Printing paths are still visible. (c) Image of a cell-free bilayered flower-shaped scaffold, 35 days after fabrication at room temperature. The flower is imaged immersed in 0.9% NaCl with 2 mM CaCl ₂	62
24	bilayered scaffolds from HA-Tyr and Alg/HA-Tyr prepared with DMEM. (a) The scaffolds after printing. Scaffolds after 2 h immersion in (b) DMEM and (c) α MEM.	63

List of Tables

1	Composition of HA-Tyr and Alg/HA-Tyr inks. (+) and (-) symbols indicate the presence or absence of the material, respectively.	10
2	Overview of the rheological parameters for the characterization of the HA-Tyr and Alg/HA-Tyr inks.	25
3	Power-law fitting for Alg/HA-Tyr and HA-Tyr inks.	26
4	Dehydration of Hydrogels and Agarose-Embedded Pellets. Table abbreviations: EtOH: ethanol, RT: Room Temperature.	64
5	Histochemical Staining of Collagen Fibers: Picrosirius Red Staining Protocol Table abbreviations: EtOH: ethanol, RT: Room Temperature.	64
6	Histochemical Staining of Glycosaminoglycan Content: Alcian Blue Staining Protocol. Table abbreviations: EtOH: Ethanol, RT: Room Temperature.	65
7	Histochemical Staining For General Assessment of Cell and Tissue Morphology: Hematoxylin-Eosin Staining Protocol. Table abbreviations: EtOH: Ethanol, RT: Room Temperature.	66